High Performance Microbial Fuel Cells and Supercapacitors Using Micro-Electro-Mechanical System (MEMS) Technology

by

Hao Ren

A Dissertation Presented in Partial Fulfillment
of the Requirements for the Degree
Doctor of Philosophy

Approved June 2016 by the
Graduate Supervisory Committee:

Junseok Chae, Chair
Bertan Bakkaloglu
Michael Goryll
Stephen Phillips

ARIZONA STATE UNIVERSITY

December 2016

ABSTRACT

A Microbial fuel cell (MFC) is a bio-inspired carbon-neutral, renewable electrochemical converter to extract electricity from catabolic reaction of micro-organisms. It is a promising technology capable of directly converting the abundant biomass on the planet into electricity and potentially alleviate the emerging global warming and energy crisis. The current and power density of MFCs are low compared with conventional energy conversion techniques. Since its debut in 2002, many studies have been performed by adopting a variety of new configurations and structures to improve the power density. The reported maximum areal and volumetric power densities range from 19 mW/m^2 to 1.57 W/m^2 and from 6.3 W/m^3 to 392 W/m^3, respectively, which are still low compared with conventional energy conversion techniques. In this dissertation, the impact of scaling effect on the performance of MFCs are investigated, and it is found that by scaling down the characteristic length of MFCs, the surface area to volume ratio increases and the current and power density improves. As a result, a miniaturized MFC fabricated by Micro-Electro-Mechanical System(MEMS) technology with gold anode is presented in this dissertation, which demonstrate a high power density of 3300 W/m^3. The performance of the MEMS MFC is further improved by adopting anodes with higher surface area to volume ratio, such as carbon nanotube (CNT) and graphene based anodes, and the maximum power density is further improved to a record high power density of 11220 W/m^3. A novel supercapacitor by regulating the respiration of the bacteria is also presented, and a high power density of 531.2 A/m^2 (1,060,000 A/m^3) and 197.5 W/m^2 (395,000 W/m^3), respectively, are marked, which are one to two orders of magnitude higher than any previously reported microbial electrochemical techniques.

Dedicated to my family whose love and support made all of this possible in my life.

My wife, Danping Yang; my daughter, Caroline Yumeng Ren.

ACKNOWLEDGMENTS

I would like to express my deepest gratitude to my supervisor, Prof. Junseok Chae, for his mentorship, guidance and support. His contagious enthusiasm and perseverance for research have been the constant driving force for my progress. He also gave me plenty of freedom for me to explore the research and whenever I turn to him for help, he is always very helpful. I feel very fortunate to have been his student, and therefore to have had such an enjoyable and fulfilling graduate school experience.

I would like to thank Prof. Bertan Bakkaloglu, Prof. Michael Goryll, Prof. Stephen Phillips and Prof. Cesar Torres for making time to serve on my committee and for enhancing my knowledge by his questions and comments.

I would also like to thank my colleagues in Prof. Chae's group: Dr. Wencheng Xu, Dr. Xu Zhang, Dr. Helen Schwerdt, Dr. Ran Wang, Sangpyeong Kim, Jennie Appel, Shiyi Liu, Ang Chen and Zhaofeng Zhang.

TABLE OF CONTENTS

CHAPTER Page

APPENDIX

LIST OF FIGURES

Figure Page

Figure Page

PREFACE

Energy crisis and global warming have become two popular topics all over the world, and we are gradually marching towards a severe energy crisis and global warming. The fossil fuels, including the oil, gas and coal contribute 80% of the total energy consumption in the world. Yet it is reported that oil, gas, and coal are all estimated to deplete or become economically unfavorable in the next 100-200 years. An increase in global temperature by 1.2 °F is also observed in the past 120 years, correlating the increase in CO_2 concentration in the atmosphere. Thus, it is essential to develop carbon-neutral, renewable energy sources. Renewable energy, such as solar energy, wind energy, hydropower energy, and bioenergy, has now been adopted as effective substitutes of fossil fuel. Of them, bioenergy is abundant, readily available and carbon-neutral, and microbial fuel cell (MFC) is a bio-inspired electrochemical converter to directly convert biomass into electricity with high efficiency. Thus in this dissertation the research on MFC is focused. A critical drawback for MFC is its low current and power density low compared with conventional energy conversion techniques and this drawback is successfully addressed in this dissertation.

CHAPTER 1

INTRODUCTION

1.1. Microbial fuel cell background

Energy crisis has been a popular topic all over the world, and we are gradually marching towards a severe energy crisis, with an ever-increasing demand of energy overstepping the current supply. According to United Kingdom Energy Research Center, the crude oil production is projected to peak in 2030, and after that it suffers from rapid post-peak decline [1]. Similar predictions are shown for natural gas, which peaks in 2020 [2]. The depletion of coal is not as urgent as crude oil, and according to U.S. National Mining Association, the United States has enough recoverable coal to power the country for the next four century; however, according to a Nature commentary, affordable coal depletes very soon and the expense of coal likely increases. Furthermore, the global mean temperature has risen above pre-historical levels due to the excessive emission of greenhouse gas, resulting in the melt of glaciers and rise of sea levels [2]. The depletion of fossil fuels and the threat of global warming facilitate the sought for carbon-neutral renewable energy sources [3, 4]. Renewable energy, such as solar energy, wind energy, hydropower energy, geothermal energy and bioenergy, has now been adopted as effective substitutes of fossil fuel. However, the contribution from renewable energy sources is still minimal: according to Renewables Global Status Report 2011, renewable energy supplied only 16% of global final energy consumption in 2009 and close to 20% of global electricity supply in 2010. In contrast, fossil fuel energy contributes a dominating portion of 81% on overall global energy consumption and 67.6% of global electricity supply [5].

Unlike other renewable energy sources, bioenergy, which utilize biomass to produce energy, is carbon-neutral and has now been actively researched all over the world. Microbial fuel cell (MFC) is one approach to utilize biomass and directly generates electricity from biomass with high efficiency. Many other bioenergy conversions exist, including incineration, gasification, fermentation, methanogenic anaerobic digestion, *etc.*, yet MFC has a number of attractive advantages such as direct electricity generation, high conversion efficiency, capability of operating at low organic concentration, and a reduced amount of sludge production. As a result, MFCs find potential applications such as scaled-up wastewater treatment and renewable energy production [6, 7, 8, 9, 10], bioremediation of recalcitrant components [11, 12] and power supply for remote sensors in hazardous or environmentally unfriendly conditions [13, 14, 15]. In addition to these applications, MFC also has potential to be a miniaturized power source.

Miniaturized power sources are used to power electronic devices, such as cell phones, remote sensor, and radio-frequency identification (RFID) devices, etc. The gold standard of miniaturized power sources is a lithium-ion battery. However, the lithium-ion battery is not renewable, and often bears safety issues. Other miniaturized power sources also possess challenging limitations. For instance, hydrogen fuel cells [16] and nuclear batteries [17] possess potential safety issues and Ni-Cd batteries and lead-acid batteries are not environmentally friendly. Besides, a power gap exists as the progress of lithium-ion batteries has not kept pace with portable technologies [18]. Consequently, it is urgent to find an alternative to replace lithium-ion batteries. Miniaturized MFCs have potential to be one of attractive alternative. Though the volumetric power density of MFCs in the year of 2011, 2333 W/m^3, is still more than 10^4 folds smaller than that of lithium-ion batteries, 60-180 Wh/kg (7.2×10^7 - 2.16×10^8 W/m^3, assuming the density of Lithium-ion battery to be 3000 kg/m^3), from the fact that during the last few years the power density of MFCs has increased by 10^4 folds [19], we foresee that miniaturized MFCs can be practical miniaturized power sources through painstaking research in the future.

1.2. MFC operation principle

An MFC is a device that directly converts chemical energy of organic compounds to electrical energy with the aid of catalytic reactions of microbes. The operating principle of a typical two-chamber MFC is illustrated in Figure 1.1. It is composed of two chambers; anode and cathode chambers which are separated by a proton exchange membrane (PEM). Both chambers are equipped with electrodes; the anode and the cathode. The PEM separates the electrolyte in the anode and the cathode chambers.

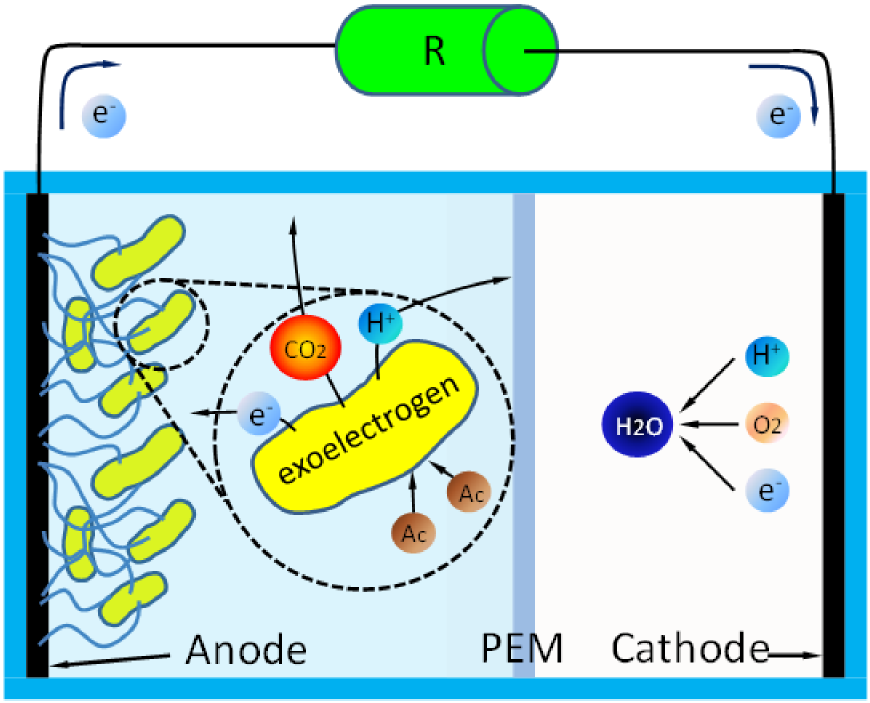

Figure 1.1. A Schematic of a conventional two-chamber microbial fuel cell. Exoelectrogen in the anode chamber break down an organic chemical, acetate, to produce electrons, protons, and CO_2. The electrons pass through an external resistor to be reduced at the cathode.

In operation, specific types of bacteria in the anode chamber breathe by breaking down organic substrates to produce carbon dioxide, protons, and electrons, and the electrons are transfered to the anode via extracellular electron transfer (EET). Then the electrons flow across the external circuit to the cathode due to the potential difference between the two electrodes, which reduce the electron acceptors such as oxygen or ferricyanide *etc.* at the cathode. As a result, an unbalanced charge distribution results in an electrical field gradient between the anode and cathode. This electrical field gradient drives cations to flow from anode to cathode chambers, and drives anions to flow from cathode to anode chambers respectively. This process results in direct conversion of biomass into electricity. Assuming oxygen is used in the cathode chamber, the half reactions in the anode and cathode can be written as

$$\text{Anode:} \quad CH_3COO^- + 2H_2O \rightarrow 2CO_2 + 8e^- + 7H^+$$

$$\text{Cathode:} \quad O_2 + 4H^+ + 4e^- \rightarrow 2H_2O \tag{1.1}$$

For a typical electrochemical system (a fuel cell with an external load connected), energy is produced as electrochemical reactions occur. The total energy of this electrochemical system can be divided into two parts, the energy change in the electrochemical system (fuel cell) which is dissipated as heat and the energy change in the external load which is obtained as electrical energy, which can either be converted to be heat, light or mechanical work. The energy dissipated as heat is the entropy change which cannot be harvested, and the total energy that can be harvested is the free energy. When the external load approaches to infinite, the largest free energy can be obtained, which is relevant to the standard cell electromotive force by:

$$\Delta G=-n\times F\times E^0 \tag{1.2}$$

Here ΔG is the maximum free energy - the Gibbs free energy [J], n is the number of electrons exchanged, F is the Faraday's constant [9.65×10^4 Cmol^{-1}] and E^0 is the standard cell electromotive force of the electrochemical system [V]. The maximum electromotive force in a typical electrochemical system is calculated by the Nernst equation:

$$E_0^{'} = E_0 - \frac{RT}{nF} ln \frac{[products]^p}{[reactants]^r}$$

Here E_0' is the electromotive force for a specific constitute concentration at a given temperature (V), E^0 is the standard cell electromotive force [V], R is the universal gas constant: $R = 8.31\ \mathrm{JK^{-1}mol^{-1}}$, T is the absolute temperature [K], F is the Faraday's constant, the number of coulombs per mole of electrons: $F = 9.65\times10^4\ \mathrm{Cmol^{-1}}$, n is the number of moles of electrons transferred in the cell reaction, Π is the reaction quotient which is the ratio of the activities of the products divided by the reactants raised to their respective stoichiometric coefficient.

Considering an example of a MFC in which exoelectrogen such as *Geobacter sulfurreducens* respire and at the same time produce energy by transferring electrons from breaking down organic substrates such as acetate to an electron acceptor such as oxygen. Applying the two half reactions in equation (1) into the Nernst equation, the total cell potential, which is the potential difference between the maximum electromotive forces of anode and cathode at pH=7, can be derived to be: $E^{o'}$=1.089 V. Note that this is the theoretical cell potential limit which often cannot be achieved in practice due to various potential loss, and we will discuss this in detail in the following sections.

1.3. Exoelectrogen and extracellular electron transfer (EET)

Exoelectrogen is not limited to *Geobacter* species (such as *Geobacter sulfurreducens, Geobacter metallireducens*) and *Shewanella* species (such as *Shewanella oneidensis* MR-1, *Shewanella putrefacians* IR-1, *Shewanella oneidensis* DSP10). *Pseudomonas* species (*Pseudomonas aeruginosa* KRP1), *Rhodopseudomonas palustris* DX-1, *Saccharomyces cerevisiae*, *Escherichia coli*, *etc*., have been also studied as exoelectrogen which have the capability of EET.

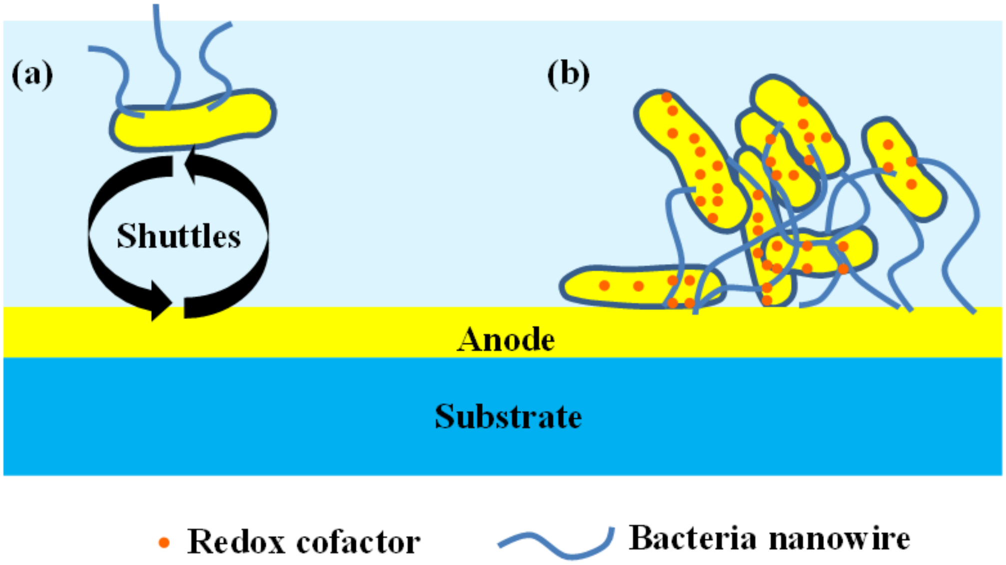

Figure 1.2. A schematic of three extracellular electron transfer (EET) mechanisms. (a) Indirect electron transfer by redox shuttles, (b) Electron transfer by conductive nanowire matrix, or electron transfer by electron superexchange through redox cofactors, such as cytochrome c.

To date, two major EET mechanisms have been reported. One is indirect EET, which rely on electron shuttles that transfer electrons from inside to outside exoelectrogen. Electron shuttles can be either self-secreted or externally added. Electron shuttles are redox driven and generally have two states: oxidized and reduced states. Electrons in Nicotinamide adenine dinucleotide (NADH, reduced form), which is a co-enzyme in all living cells, can be transferred to the oxidized states that are located outside exoelectrogen through a series of membrane-bound and periplasmic cofactors, which reduces the oxidized states. The reduced states are then driven to the anode by redox and release electrons to anode and become oxidized state. Afterwards, the oxidized states again are driven back to exoelectrogen to repeat the process, as illustrated in Figure 1.2 (a).

The other mechanism is the direct EET, which is still on debate. Years ago, it was generally believed that the direct EET mechanism is due to the nano-meter scale *pili* secreted by exoelectrogen, and *in-situ* measurements indicate the *pili* are metallic like, although the conductivity is low compared with metal. According to this mechanism, electrons produced by exoelectrogen can be transferred to the anode directly through the conductive nano *pili*. Recently some researchers claimed that EET relies on the electron super-exchange (electron hopping) between adjacent redox cofactor (such as cytochrome c), and the process is driven by redox. The redox cofactor is immobilized in exoelectrogen, and the reduced redox cofactor caused by the respiration of exoelectrogen can exchange electrons with adjacent oxidized redox cofactor. After multiple electron exchange processes, electrons are transferred to the anode from exoelectrogen. With regards to how electrons are transferred from inside the exoelectrogen to the redox cofactor still remains to be unveiled.

1.4. MFC applications

According to dimensions, MFCs may be divided into three categories, the macroscale, mesoscale and microscale MFCs. The macroscale MFCs have a total volume, including anode and cathode chambers, larger than 500 mL. The mesoscale MFCs have a total volume between 0.2 to 500 mL and the microscale MFCs have a total volume less than 200 μL. During the past century, MFCs have found numerous new applications. In this section, we will briefly review the application of conventional MFCs and then discuss the potential applications of microscale MFCs.

The main role of an MFC is a power source to generate electricity from organic substance, and during the past century a variety of substrates which contains organic substance have been utilized, ranging from wastewater (municipal, industrial, and food wastewater, carbohydrate, proteins, organic acid and alcohol, living plants, inorganic substrate to even radiation waste.

Most reported MFCs are merely at lab-scale, yet some have reached beyond the lab-scale to be field-scale, such as power supplies for sensors and monitoring systems for remote, rural, dangerous and environmentally unfriendly applications where batteries and on-site solar energy harvest systems use are limited. The first application of an MFC as a practical power source was to power a meteorological buoy (Figure 1.3(a)) [20]. Pilot-scale environmental sensor networks were built by Trophos Energy Inc. in 2010 [14, 15]. MFCs have been demonstrated to power a hydrophone, a wireless temperature sensor and a photodiodes. In these systems, DC-DC converters and low power management systems were implemented to boost the output voltage to be at a usable voltage range. To avoid energy loss, capacitor arrays were adopted to allow capture and store energy from arrays of MFCs. MFCs have also applications in powering robots [21, 22, 23].

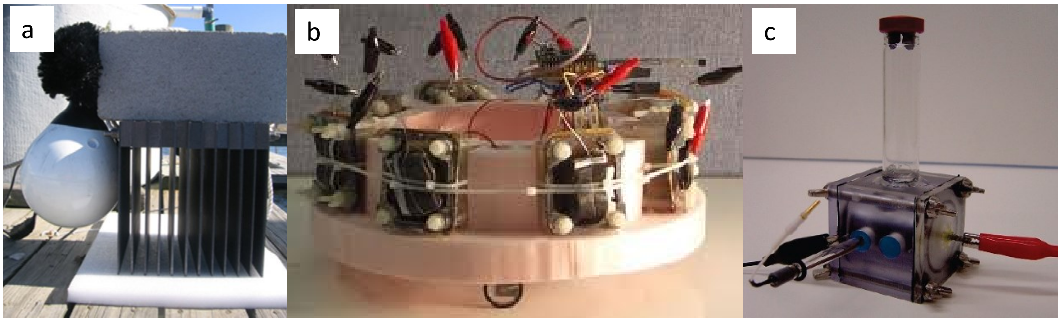

Figure 1.3. Photographs of MFCs for a variety of applications. (a) photograph of the first application of MFC as a viable power source to power a meteorological buoy, (b) robot with air-cathode MFCs on board, to perform sensing, information processing, communication and actuation when fed (amongst other substrates) with flies. This is the first robot in the world, to utilize unrefined substrate, oxygen from free air and exhibit four different types of behavior, (c) Single chamber MEC shown with gas collection tube (top), Ag/AgCl reference electrode (extending from the front), cathode connection (left clip) and brush anode connection (right clip).

Beyond generating electricity, MFCs have also been used for producing hydrogen or other chemicals (e.g., methanol or acetate) when no electron reducers are present at cathodes, or used for environmental sensors for sensing organic concentration or chemical oxygen demand (COD), dissolved oxygen, toxicity, pH and temperature.

The applications of macroscale MFCs suggest possible applications of microscale MFCs. Microscale MFCs may perform better in some applications, including power sources for implantable medical devices, low-power integrated circuit, and portable power sources in rural and environmental unfriendly setups, and developing electronics and sensors, *etc*. partially because microscale MFCs possess unique advantages such as small size, short start-up time, compatibility with microfabrication.

Traditional implantable medical devices (IMDs) should be replaced when battery runs out. For example, the battery of pacemakers, spinal cord stimulators and retinal stimulators needs to be replaced every few years, causing pains and financial burdens for patients. The power needed for IMDs falls in the level of μW to mW, which is in accordance with the power output of MFCs. MFCs as power sources in IMDs have been proposed to be placed in human large intestine and could utilize intestinal contents and microorganisms to generate electricity[24]. However, the size of the reported MFC is rather large (10 cm × 1.0 cm × 2.5 cm), which may cause potential issues including the clogging of large intestine, bringing pain to patients and the biocompatibility of the implantable MFC also needs to be further studied. A microfabricated MFC for IMD application has also been proposed to use glucose in human plasma[25]. The microfabricated MFC is made of a biocompatible material (PDMS) and has small dimensions (1.7 cm × 1.7 cm × 0.2 cm) and net weight of less than 0.5 g, yet the maximum output power is very low (about 2.3 nW). Another microscale MFC for IMD applications has been proposed to use white blood cells to produce electrons; yet this research is only in its preliminary stage [26]. Currently there are many challenges to be addressed for the application of microscale MFCs to IMDs, yet considering the fact that the power density of microscale MFCs has been improved by several orders of magnitude within the last decade, microscale MFCs may become an attractive alternative to currently available power sources such as Lithium-ion batteries, nuclear batteries, hydrogen batteries and rechargeable batteries.

Microscale MFCs can be used as power sources for low-power electronics. As microscale MFCs are small in size, they can be integrated with DC-DC converters. They can be power sources for RFID applications; for instance, battery assisted passive RFID devices as their power consumption is extremely low. One advantage of MFCs is that they do not need to be charged when the output power becomes low; one can add substrate to the anode chamber. Furthermore, microscale MFCs can be built by flexible materials, such as PDMS, parylene and polymide *etc.*, which make them useful in flexible electronics. Microscale MFCs as power sources for low-power electronics can be rather close-to-market: it is unlikely that the technical development of batteries keeps in pace with the accelerating power demands; small, microscale fuel cells enable higher overall energy density than batteries; and the market for low-power electronics has an inherently high cost tolerance[16]. In order to be used in low-power electronics, the negative effect of using fuel cell with live electrogen should be addressed. One possible way is to use hermetic packaging to make sure electrogen and electrolyte not exposed to human beings in everyday use.

Microscale MFCs are attractive in remote locations as power sources where externally-supplied electricity is not readily available. MFCs may operate in harsh environments, such as low temperature (4 °C) and environmental unfriendly conditions. Consequently renewable and self-sustainable power sources including MFCs may be an alternative to where Lithium-ion batteries are not the best option.

Microscale MFCs have the potential to be electronic devices. A bacteria-based and logic gate has been developed using a *Pseudomonas aeruginosa lasI/rhlI* double mutant with two quorum-sensing signaling molecules as the input signals[27]. By using microscale MFCs, these devices could be minimized, allowing potential integration.

Finally, microscale MFCs can be used for miniaturized biosensors as exoelectrogen are sensitive to specific chemicals. A silicon-based microscale MFC toxicity sensor has been reported and preliminary result of its fast response at the exposure of formaldehyde has been validated[28]. This microscale MFC-based toxicity sensor is the first attempt to use exoelectrogen as a toxicity sensor using microfabrication technology. Despite of preliminary success there are several challenges to be addressed, including capability to obtain quantitative sensitivity to toxin, selectivity to different toxins, and others. It is possible to form an array of such sensors to identify different toxic substrates.

1.5. Prior art of MFCs

Most macroscale MFCs are proposed to process large amounts of organic substance, such as marine sediment or wastewater and transform them to generate electricity. One of the most well-known macroscale MFCs, as developed by Tender et al. [20], is composed of two benthic MFCs (BMFCs, one type of MFC driven by the naturally generated potential difference between anoxic sediment and oxic seawater) and is used to power an autonomous meteorological buoy. Their first BMFC has a volume of 1.3 m^3 and produces 24 mW (Figure 1.4(a)).

The same group reported the second version which have a smaller volume of 0.03 m^3 yet producing an increased power of 36 mW (Figure 1.4(b)). More traditional MFCs involve wastewater treatment can be exemplified by the pilot scale MFC constructed by the Advanced Water Management Center in University of Queensland. This reactor has a volume of approximately 1 m^3 and consists of 12 modules. Carbon fiber anodes and cathodes are used, based on a brush design (Figure 1.4(c)). In the second phase, 12 additional modules was planned to be constructed. The performance of their MFC is not reported yet[29]. Another example MFC utilized in wastewater treatment contains 12 anodes/cathodes, a volume of 20 L, and a resulting power density of 380 mW/m^2. Despite of these successful prior art, most macroscale MFCs suffer from low substrate concentration, low conductivity, low buffer capacity, high toxicity, high dissolved oxygen level, and large temperature variance in wastewater, which result in high energy loss to achieve power density in the range of 0.17-1.44 W/m^2 (5-144 W/m^3).

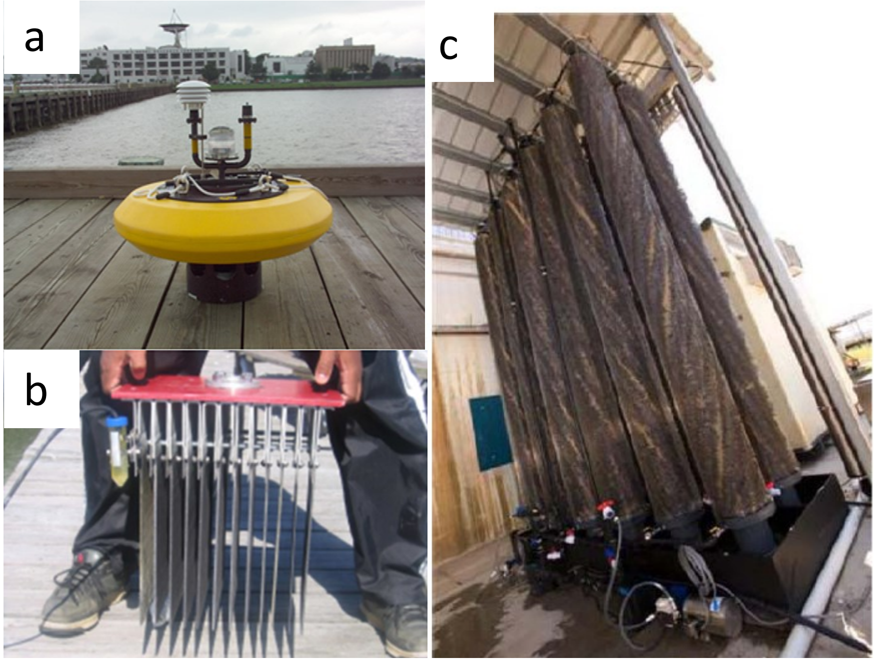

Figure 1.4. Photographs of various macroscale MFCs. (a) the first BMFC constructed by Tender et al. 2007, which has a mass of 230 kg, a volume of 1.3 m^3 and sustains 24 mW, (b) The second version of BMFC constructed by Tenders et al, . 2007, which has a mass of 16 kg, a volume of 0.03 m^3 and sustains 36 mW, (c) macroscale MFC set up by the Advanced Water Management Center in University of Queensland, which has a volume of 1 m^3 with 12 modules.

The majority of previously reported MFCs are mesoscale MFCs. Due to the short distance between electrodes, large surface area to volume ratio, and fast mass transfer and reaction kinetics, the mesoscale MFCs present significantly higher power densities than those of macroscale MFCs. The highest areal power density reported in 2011, 6.86 W/m^2, was achieved by a mesoscale MFC using a single chamber air-cathode MFC[30]. This elevated power density is mainly due to the large cathode area to anode area ratio and elimination of the proton exchange membrane. The same group also achieved an areal power density of 1.8 W/m^2 and a volumetric power density of 1010 W/m^3 by applying a new MFC configuration-cloth electrode assembly (CEA) in a single chamber MFC. By eliminating the

PEM and reducing oxygen diffusion by J-cloth, a low internal resistance of 92 Ω and a high CE of 71 % were achieved[31]. Ringeisen et al. constructed a mesoscale MFC having a smaller volume of 1.2 mL, a high anode specific area of 611 cm^2, and a high flow rate of 1.2 mL/minute, to produce a high areal power density of 2 W/m^2 and a volumetric power density of 330 W/m^3, respectively[32]. Other researchers have reported power densities in the range of 1.5-4.31 W/m^2. Figure 1.5 illustrates two exemplar mesoscale MFCs reported by Fan et al. 2008 and Reigeisen et al. 2006.

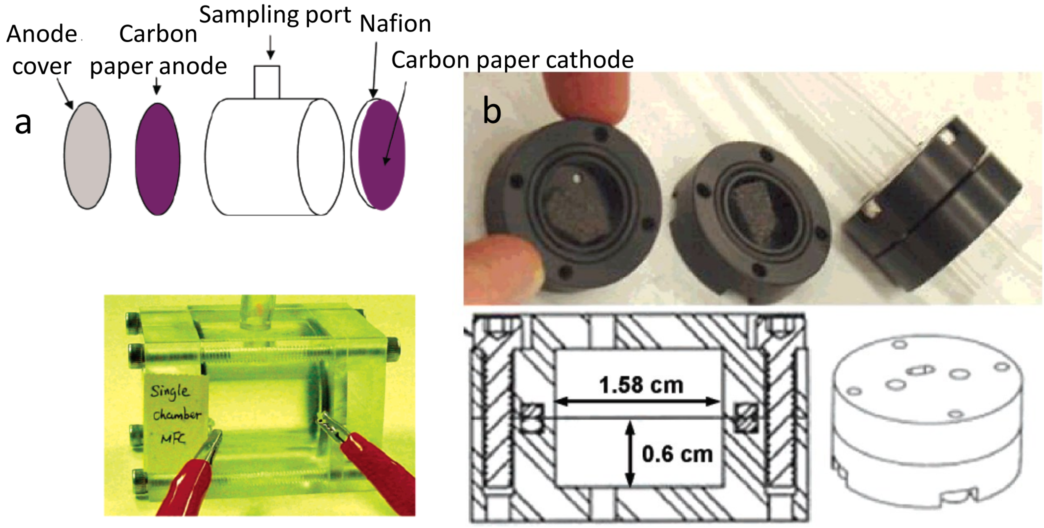

Figure 1.5. Two mesoscale MFCs. (a) a single chamber air-cathode MFC; because of the large cathode area to anode area ratio, the highest reported areal power density (6.8 W/m^2) was achieved (Fan et al. 2008) and (b) a miniaturized MFC with a volume of 1.2 mL; due to the high flow rate 1.2 mL/min, it produced high areal/volumetric power densities of 2 W/m^2 and 330 W/m^3, respectively (Ringeisen et al. 2006).

Microscale MFCs have emerged with the surge of technological innovations and increased commercial success of microfabricated systems[33, 34, 35]. Due to the advantages of microfabrication technology, including small size, light weight, batch fabrication capabilities for potentially low production cost, low power, microscale MFCs may introduce promising applications in portable power sources and “Lab-on-a-chip” systems as has been demonstrated by its increased recognition in prior literature. Such promise is supported by further impacts from short electrode distance, large area to volume ratio, fast mass transfer and reaction kinetics, and short start-up time, the similar parameters to improve power density when scaling down from macroscale to mesoscale MFCs.

The first microscale MFC was conceived by Chiao et al. in 2002 utilizing *Saccharomyces cerevisiae* to break down glucose for generation of electricity[36]. The MFC featured an electrode area of as small as 0.07 cm^2, and generated very low power, 5.72 nW/m^2, which is far less than that of typical mesoscale MFCs, 0.01 W/m^2 [37]. In the following years, the same research group optimized the microscale MFC by introducing microfluidic channels in the anode and cathode chambers to increase the surface area to volume ratio, and were able to obtain an areal power density of 23 $\mu W/m^2$ and a volumetric power density of 0.276 W/m^3, more than three orders of magnitudes higher than their first version[38]. Their power density was further enhanced by fabricating micropillars on the PDMS substrate by soft lithography, which effectively increase surface area to volume ratio, resulting in an areal power density of 4 mW/m^2 and a volumetric power density of 40 W/m^3 [25]. A microscale MFC has been proposed to provide on chip power supply by Qian et al., and the 1.5 μL MFC produced an areal power density of 1.5 mW/m^2 and a volumetric power density of 15 W/m^3 [39]. They also implemented microfluidic channels and soft lithography to create a MFC with a volume of 4 μL, producing an areal power density of 6.25 mW/m^2 and 62.5 W/m^3 [40].

Geobacter species, which generally produce higher power density, were first introduced for utilization in microscale MFCs by Parra and Lin, reporting an areal power density of 0.12 W/m^2 and a volumetric power density of 0.34 W/m^3 [41]. Carbon nanotubes (CNT) were introduced as electrode material as they allow a large surface area to volume ratio and are shown to be biocompatible with microbes. With CNTs as electrodes, an areal power density of 73.8 mW/m^2, and a volumetric power density of 16.4 W/m^3 were achieved[42]. Choi et al. designed a microscale MFC producing an areal power density of 47 mW/m^2 and volumetric power density of 2333 W/m^3, the highest volumetric power density recorded in 2011 for all MFCs regardless of their sizes. The improved power density was accomplished by reducing the distance between the anode and cathode and adding *L-cysteine* into the anode chamber to mitigate oxygen leakage[43]. The first successful microscale MFC array in a series stack configuration was also presented by the same group and produced a power output of 100 μW and an areal power density of 0.33 W/m^2, both of which are the highest in all microscale MFCs. The volumetric power density was reported as 667 W/m^3 [44].

Microscale MFCs may also be employed for various exoelectrogen identification, characterization and toxicity sensing applications. Microscale MFCs have been utilized for identifying and characterizing exoelectrogen due to their compact size and simplicity in assembly into an array configuration of MFCs[45]. A novel microscale MFC toxicity sensor has also been constructed and its proof of concept has been used for the detection of formaldehyde[28]. Figure 1.6 illustrates the various types of microscale MFCs.

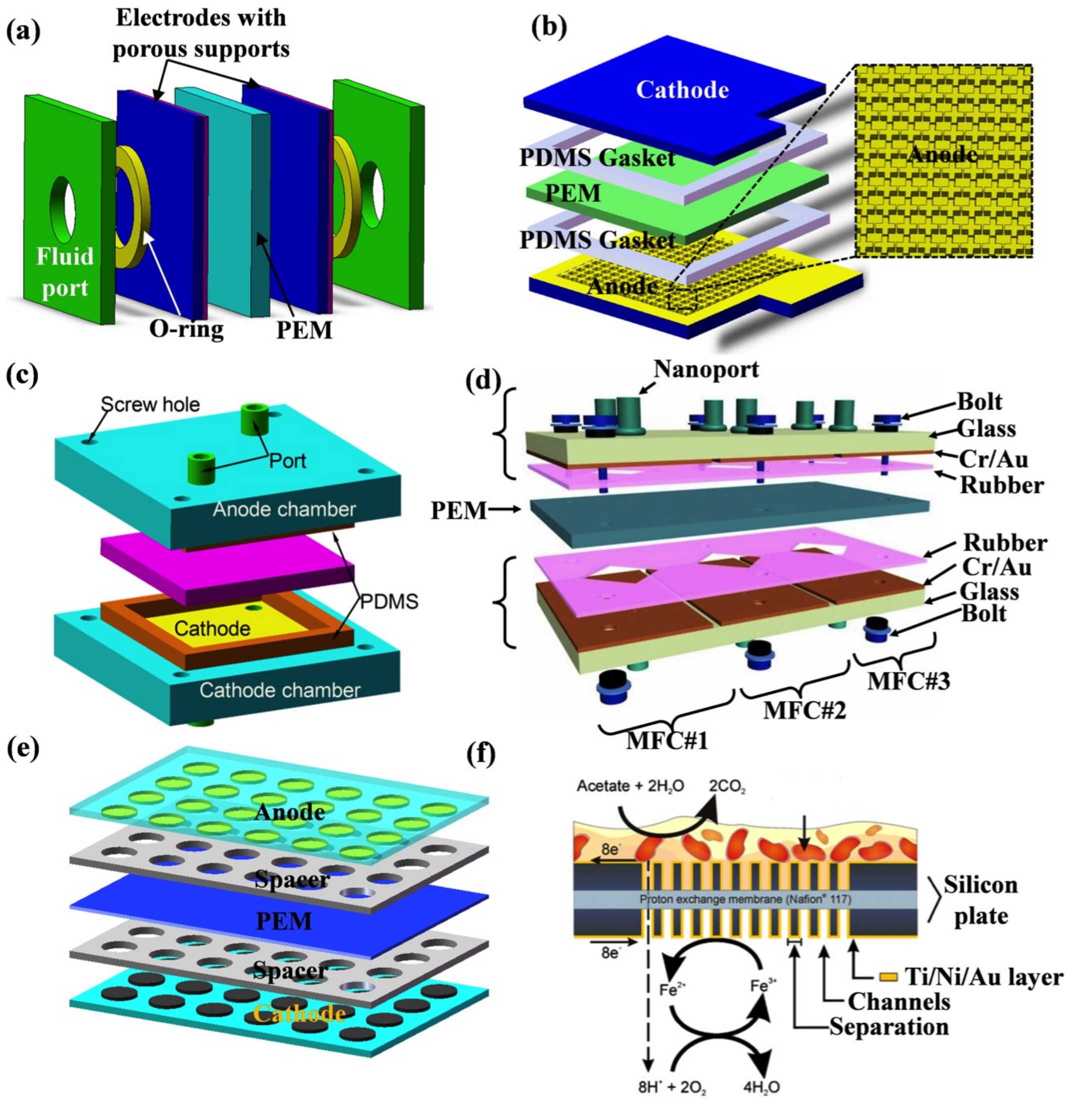

Figure 1.6. Schematic of various microscale MFCs. (a) the first microscale MFC by Chiao et al. 2002, which produced a areal power density of 5.72 nW/m^2 (b) microscale MFC presented by Siu and Chiao 2008, by applying micropillars to increase surface area to volume ratio, an elevated areal/volumetric power density of 4 mW/m^2 and 40 W/m^3 were achieved (c) microscale MFC presented by Choi et al. 2010, by reducing the distance between anode and cathode and mitigating oxygen leakage by adding L-cysteine, areal and volumetric power densities of 47 mW/m^2 and 2333 W/m^3 were obtained (d) Three microscale MFCs in series presented by Choi and Chae 2011, Choi and Chae 2012, which achieved an OCV of 2.47 V and a maximum power output of 100 μW, (e) microscale MFC array presented by Hu et al. 2009, which aims for identify and characterize exoelectrogen (f) microscale MFC as a toxicity sensor presented by Dávila et al. 2011.

From examples of MFCs described above, one may clearly observe that mesoscale MFCs present higher power density than macroscale counterparts thanks to generous effects from scaling effects including shorter distance between electrodes, high surface area to volume ratio, fast mass transfer and reaction kinetics; yet microscale MFCs do not seem to benefit from them. The following chapter discusses theoretical analysis of the scaling effects to understand and predict how significantly the scaling effects impact the areal and volumetric power density of MFCs.

CHAPTER 2

SCALING EFFECT ON MINIATURIZED MFCS

2.1. Mass transfer and reaction kinetics

The Monod equation well describes substrate oxidation rates of bacteria in biofilms including air-breathing bacteria in biofilms[46]. The oxidation rates in biofilms reach at steady state where substrate flux equal to the oxidation rates. Then, bacterial kinetics can be expressed by substrate flux at steady state. In order to simplify the calculation, we assume that the reaction rate is significantly fast compared with diffusion and use the first order reaction kinetics model to describe reaction kinetics of air-breathing bacteria. The maximum flux of the substrate, J, that can be consumed by air-breathing bacteria is

$$J = \sqrt{k_1 D}c \tag{2.1}$$

where k_1 is the rate constant, D is the diffusivity of fluid, and c is the concentration of the substrate. The maximum flux of the substrate can also be written as

$$J = k_c c \tag{2.2}$$

where k_c is mass transfer coefficient. It is common to use the stagnant film model, then, the mass transfer coefficient in a stagnant film can be written as:

$$k_c = Sh(\frac{D}{L_s}) \tag{2.3}$$

where Sh and L_s are the Sherwood number and the characteristic length [m], respectively. Sh can be deduced as:

$$Sh = 0.664\,\mathrm{Re}^{1/2}\,Sc^{1/3} \tag{2.4}$$

where Re is the Reynolds number which can be written as

$$\mathrm{Re} = {\rho v L}/{\mu} \tag{2.5}$$

where ρ is the specific density of the fluid, v is the linear velocity of the fluid, μ is the viscosity of the fluid. L is the characteristic length of the chamber of microscale MFC is written as

$$L = \frac{4A}{p} \tag{2.6}$$

where A and p are the cross section area and the wetted perimeter of the anode chamber, respectively. From equation (2.4) the Schmidt number, S_c, can be written as

$$Sc = {\mu}/{\rho D} \tag{2.7}$$

Therefore, the maximum current and power can be written as

$$I_{\max} = k_c \cdot b \cdot A \cdot e \cdot CE \cdot c \tag{2.8}$$

$$P_{\max} = k_c \cdot b \cdot A \cdot e \cdot CE \cdot c \cdot E \tag{2.9}$$

where b is the number of moles of electrons produced by oxidation of acetate (b = 8 mole e^- /mol), A is Avogadro's number (6.023×10^{23} molecules/mole), e is electron charge (1.6×10^{-19} C/electrons), CE is the columbic efficiency and E is the output voltage of MFC.

Equation 2.5 shows *Re* decreases as the characteristic length decreases assuming all other parameters remain unchanged, and equation 2.3 demonstrates the mass transfer coefficient increases as scaling down MFC. This leads that scaling down MFC delivers a higher mass transfer coefficient assuming other parameters remain unchanged. Consequently, the maximum current and power are expected to improve as scaling down a dimension of MFC.

For example, assume an anode chamber of 20 m × 20 m × 25 cm, linear fluid velocity of 1×10^{-3} m/minute, an anolyte concentration of 25 mole acetate/m^3, a specific density of fluid of 997 kg/m^3, a viscosity of fluid of 0.89×10^{-3} N·s/m^2 and a diffusivity of fluid of 0.88×10^{-9} m^2/s then $Re = 45.74$, $Sc = 103.5$, and $k_c = 1.0497\times10^{-7}$ m/s, respectively. Assuming *CE* of 50 %, *E* of 0.4 V, the maximum areal/volumetric current densities of a macroscale MFC are 1.01 A/m^2 and 4.05 A/m^3, respectively. Likewise, the maximum areal/volumetric power densities of a macroscale MFC are 0.405 W/m^2 and 1.62 W/m^3, respectively.

For a microscale MFC with the same linear fluid velocity of 1×10^{-3} m/min, yet scaling an anode chamber by a factor of 1000, (20 mm × 20 mm × 250 µm), we can calculate that $Re = 0.04574$, $Sc = 103.5$ and $k_c=3.3193\times10^{-6}$ m/s, respectively. Again assuming *CE* of 50 %, *E* of 0.4 V, the maximum areal/volumetric current densities of a microscale MFC are 31.99 A/m^2 and 1.28×10^{5} A/m^3, respectively. Likewise, the maximum areal/volumetric power densities of a microscale MFC are 12.8 W/m^2 and 5.12×10^{4} W/m^3, respectively. This estimation sounds very attractive; however, one additional parameter, internal resistance, must be taken into account to verify the scaling effect more appropriately.

The maximum current of the microscale MFC can be calculated as 31.99 $A/m^2 \times 0.0004\ m^2 = 0.0128$ A. To be able to reach such high current, the internal resistance of the microscale MFC must be very low; $R_{int} = V / I = 31.25\ \Omega$. This is a rather low internal resistance which few microscale MFCs can reach to date. Yet it should be noted the highest current density reported so far is approximately 66 A/m^2 [47]. By limiting the maximum current density of a microscale MFC to be 66 A/m^2, the maximum areal/volumetric current and power densities can be estimated as 66 A/m^2 / 2.64×10^5 A/m^3 and 26.4 W/m^2 / 1.16×10^5 W/m^3, respectively.

Reynolds number, R_e, and mass transfer coefficient, k_c, at different characteristic lengths, from macroscale to nanoscale, are plotted in Figure 2.1. When the characteristic length decreases, R_e decreases and k_c substantially improves.

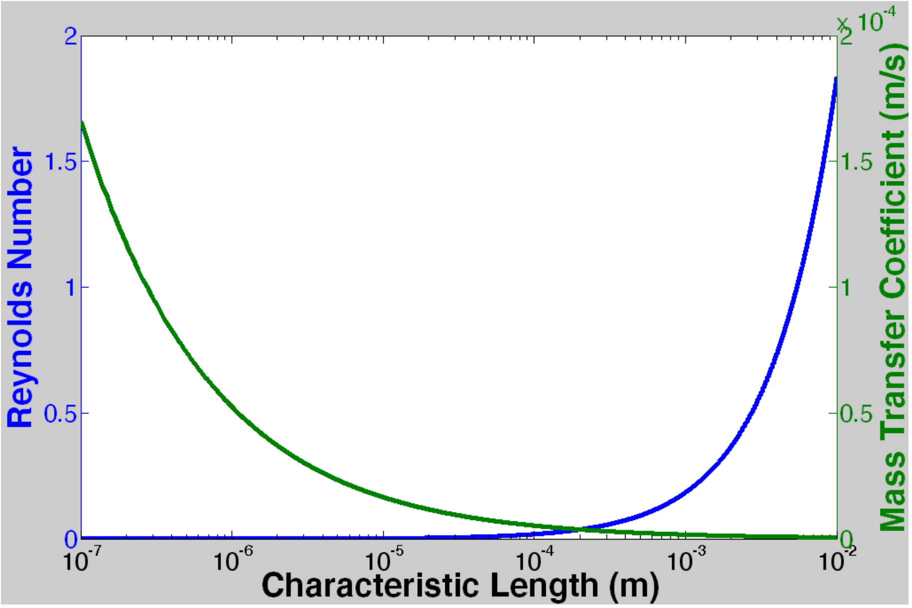

Figure 2.1. Reynolds number and mass transfer coefficient versus the dimension of MFCs. Moving from 1 cm to 100 nm in characteristic length lowers Reynolds number from 0.18 to 1.8×10^{-5} and enhances mass transfer coefficient from 1.7×10^{-6} to 1.66×10^{-4} m/s.

2.2. Internal resistance

Internal resistance often limits the performance of an MFC as discussed in the previous chapter. Suppose the mass transfer, biological kinetics of exoelectrogen, and electron transport from electron donor to the anode all remain unchanged, electrical resistance of a cell is written as:

$$R = \frac{\rho l}{A} \tag{2.10}$$

Here R is the electrical resistance, ρ is the resistivity, l is the length and A is the effective area of reaction occurs. R is directly proportional to $1/A$. The internal resistance of a traditional two-chamber MFC is summation of the resistance of anode R_a, cathode R_c, electrolyte R_e and ion exchange membrane R_m,

$$R_i = R_a + R_c + R_e + R_m \tag{2.11}$$

Note that the ohmic resistance of membrane refers to the resistance of ions movement, not electrons, different from the electrical resistance of membrane. All these resistance components in equation 2.11 are directly proportional to *1/A*, $R_i \infty \frac{1}{A}$.

OCV (E_{ocv}) is independent of the scaling effect in an MFC, the highest power, P_{max}, of an MFC is written as:

$$P_{\max} = \frac{E_{OCV}{}^2}{4R_i} \tag{2.12}$$

Then, the maximum area and volume power density is expressed as

$$p_{\max,areal} = \frac{P_{\max}}{A} = \frac{E_{OCV}{}^2}{4R_i \cdot A}, \quad p_{\max,volumetric} = \frac{P_{\max}}{V} = \frac{E_{OCV}{}^2}{4R_i \cdot V} = \frac{E_{OCV}{}^2}{4R_i \cdot A} \cdot SAV$$

(2.13)

where SAV is the surface area to volume ratio. The maximum areal power density remains constant as A changes since R_i is proportional to *1/A*. This means the areal power density is rather independent of scaling effect assuming all other parameters, *i.e.* the mass transfer, reaction kinetics, thickness of biofilm and resistivity, *etc.,* remain unchanged. In fact, some of these parameters improve as scaling down the dimension; thus in theory the areal power density is expected to improve as scaling down the dimension of an MFC.

Similarly, the volumetric power density is directly proportional to *SAV*. Therefore, as we scale down the chamber, the *SAV* increases, resulting in the enhancement of the volumetric power density. Detailed comparison between areal and volumetric power densities are presented in section above.

According to equation 2.10, R_i is directly proportional to $1/A$. In other words, $R_i \cdot A$ is constant for a specific MFC no matter how the surface area changes. Thus, it is useful to define a parameter, $R_i \cdot A$, areal resistivity (r_i). The larger the areal resistivity is, the smaller the areal power density becomes. Some researchers have extensively studied individual resistance components of an MFC. These analysis also suggest that when analyzing the overall performance, the areal resistivity is a more significant parameter than the individual resistances components. To reduce the areal resistivity, the electrode conductivity, electrolyte conductivity, mass transportation, electrode surface area to volume ratio should be increased, and electrode size, electrode distance, electrode overpotential, and electrolyte acidification should be reduced, and electrode biocompatibility should be improved.

2.3. Promises

Scaling effect. As discussed above, by scaling down, the micro-scale MFC have advantage both in mass transfer and surface area to volume ratio. Due to the detailed description above, here the scaling effect is not discussed in detail.

Recent performance enhancement in micro-scale MFC. The discussion in previous section projects the power/current density of MFCs improves as scaling down their dimensions. In this section, we list prior art of macroscale, mesoscale, and microscale MFCs to compare their performance. When scaling down from macroscale to mesoscale, prior studies demonstrate enhancement of both areal and volumetric power densities. The highest areal and volumetric power densities in mesoscale MFCs are higher than those of macroscale MFCs by a factor of 4.8 and 7.

On the other hand the performance of microscale MFCs in literature does not support the scaling effect. In fact, the performance of microscale MFCs is even lower than that of macroscale counterparts. The first microscale MFC was reported in 2002. The areal and volumetric power densities of microscale MFCs have been improved by a factor of 5.8×10^7 and 8.5×10^3, respectively, in a decade. As discussed in the previous section, volumetric power density scales well to microscale MFCs and the highest volumetric power density in all MFCs (2333 W/m^3) was achieved using the microscale MFC. Figure 2.2 and Figure 2.3 show the areal and volumetric power density versus CE for exemplar macroscale, mesoscale and microscale MFCs reported before 2012. Microscale MFCs generally have lower areal power density and CE than those of macroscale and mesoscale MFCs, yet the gap among them close rapidly during the past few years. Unlike areal power density, the volumetric power density of microscale MFCs has already surpassed that of macroscale and mesoscale MFCs due to the significant increase in SAV. There are many aspects to address enhancing both areal and volumetric power densities, such as increasing SAV, reducing internal resistance (areal resistivity), mitigating the oxygen leakage, reducing the energy loss caused by high overpotential and seeking for solutions for the acidification in the anode chamber, *etc*.; however we believe that if these challenges are effectively mitigated, the performance of microscale MFCs substantially improve and exceed that of mesoscale and macroscale MFCs. We expect in the next ten years through worldwide research, one or two magnitudes of power density enhancement can be achieved, bringing microscale MFCs an attractive alternative as miniaturized power sources.

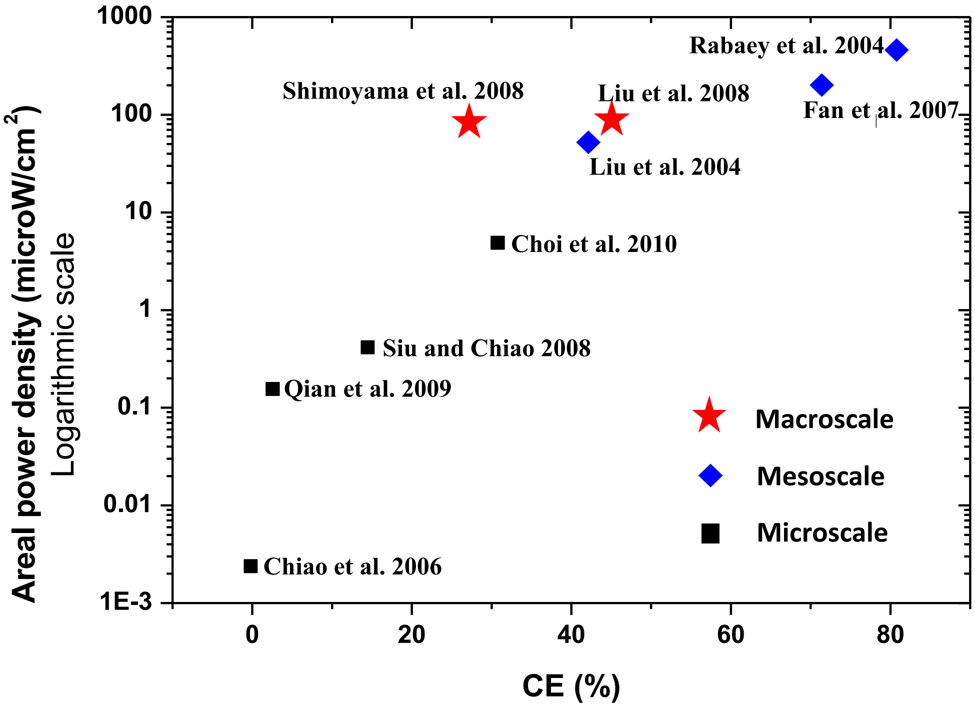

Figure 2.2. Areal power density versus CE of macroscale, mesoscale and microscale MFCs.

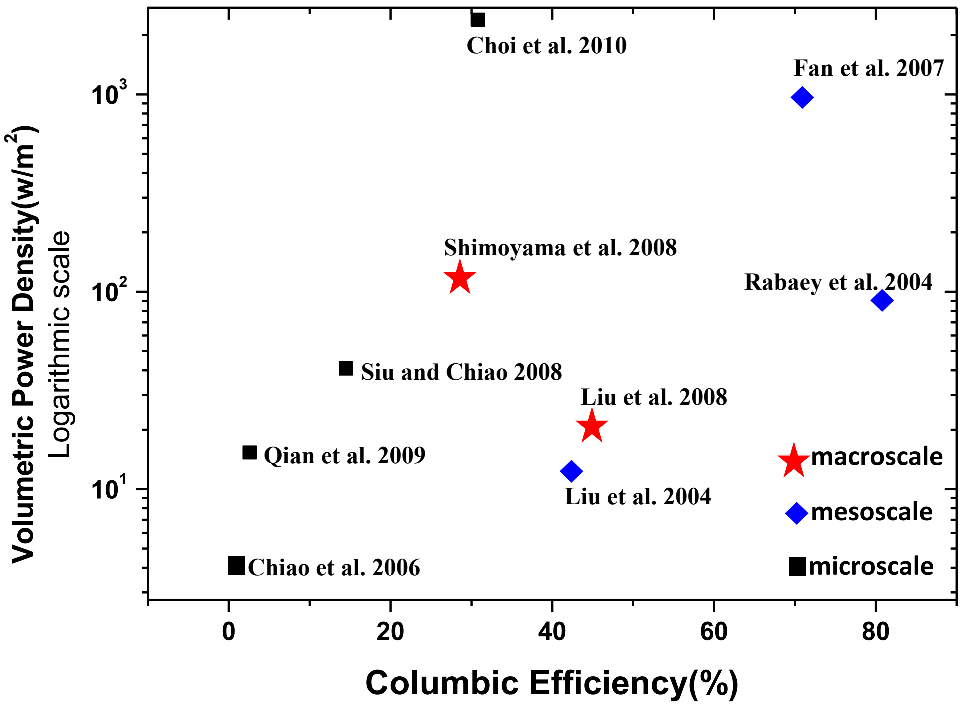

Figure 2.3. Volumetric power density versus CE of macroscale, mesoscale and microscale MFCs.

2.4. Challenges

Scaling effect. Micro-scale MFCs have shown significant potential; however, in order to convert these promises into reality, many challenges still remain unsolved, including high internal resistance (high areal resistivity), non-compatibility with microfabrication and oxygen leakage to anode. In this section, These challenges are discussed thoroughly and then present potential mitigations.

High internal resistance . Minimizing energy loss is the predominant task to improve the performance of microscale MFCs. Energy loss originates from the potential loss, which is the difference between the equilibrium electrical potential with no net current and the potential with a current. Typically, the total cell potential, $E^{o'}$ is determined by the Gibbs free energy. However when an external load is connected, energy loss is ubiquitous in practical applications, including different current densities, biofilm-anode compositions and thicknesses, substrate concentrations, pH, electrode materials, electrode distances, membrane, *etc*.

Generally, energy loss in chemical fuel cells including MFCs are divided into three categories: ohmic loss, activation loss and concentration loss. The ohmic loss is the energy loss due to electrical resistance of electrodes, and resistance of ions flow in the electrolyte and PEM; thus the ohmic potential loss is directly proportional to current density. The activation loss is the energy required for overcoming energy barriers across the electrode/electrolyte interference to generate net current. It is characterized by the Butler-Volmer equation or Tafel equation and it is significant at low current densities. Concentration loss arises from the concentration gradient between bulk liquid and electrode surface, which generally becomes significant at high current densities. These three energy losses correspond to three types of internal resistance: the ohmic resistance, the equivalent resistance of activation overpotential and the equivalent resistance of the concentration overpotential. The overall resistance is the sum of the three. The maximum areal/volumetric power is proportional to OCV of a MFC, surface area, and internal resistance, and therefore decreasing internal resistance directly impacts the maximum power. In the following sections, we discuss the three types of internal resistance in detail and then present approaches to reduce them.

The ohmic resistance can be divided into two parts: electrode resistance and electrolyte/membrane resistance. The former refers to the resistance caused by electrons movement through biofilm to anode, electrical contact, electrodes, and wires. The later refers to the resistance caused by movement of ion in electrolyte and ion exchange membrane for charge neutrality. Note that the ohmic resistance of membrane refers to the resistance of ions movement, not electrons, different from the electrical resistance of membrane. The equivalent ohmic resistance of ion exchange membrane is much larger than the electrical resistance of membrane. A standard method to measure the resistance of membrane can be found in Kim et al. [48]. They compared the resistance of an MFC with and without an ion exchange membrane, and deduced the resistance difference is the ohmic resistance of membrane. The ohmic resistance is critical to current/power density of MFCs as it dominates the overall internal resistance when current density increases. For instance, assuming E_{ocv} to be 0.8 V, the ohmic resistivity is 100 $\Omega\cdot cm^2$, the highest power/current density of an MFC can achieve is limited to 1.6 mW/cm^2 / 4 mA/cm^2, so the ohmic resistance directly determines the highest power density and current density. As a result, it is important to reduce the ohmic resistance.

For most scaled up MFCs, to reduce the electrode resistance, researchers replace large electrodes with multiple small electrodes. It is easy to see that this approach is not suitable for microscale MFCs whose electrode is very small. Also, as the internal resistance of microscale MFCs is larger than that of macroscale MFCs, for most cases the contact resistance between electrodes and wires is negligible.

It is critical to reduce the resistance for electrons to be transferred to electrodes. Researchers looked for materials having a high conductivity, low overpotential, biocompatibility with exoelectrogen, *etc*. Carbon-based materials such as carbon cloth, carbon mesh, carbon paper, graphite fiber brush, graphite foam, graphite plates and sheets are often used in macro or mesoscale MFCs as these materials provide very small internal resistance (areal resistivity). In contrast, currently most microscale MFCs reported so far uses a thin layer of metals such as gold, mainly because metals are readily used in microfabrication. However, high internal resistance is prevalent in those microscale MFCs, primarily due to high contact resistance at the interface of exoelectrogen and electrode, resulting in low performance. This motivates the search for carbon-based materials compatible with microfabrication to effectively mitigate the high internal resistance. One exemplar work is to use carbon nanotube (CNT) and graphene which offer superb conductivity and relatively good compatibility with microfabrication[49]. Though the use of CNT sometimes adversely impact the microorganisms growth [50], CNT has been successfully used as the anode material in macroscale or mesoscale MFCs by several researchers and the approach was adopted to microscale MFC anodes, which results in an 205% enhancement in the power density[42, 51, 52]. Graphene is another attractive material, yet to date fabricating a single layer, high quality graphene is still very challenging. The traditional fabrication approaches, such as mechanical exfoliation, chemical exfoliation, epitaxial growth on silicon carbide, and segregation of hydrocarbon in thin metal film, are challenging to be adopted to fabricate graphene on a large area for MFC electrodes. While graphene fabricated by epitaxial on metal and Chemical Vapor Deposition (CVD) can achieve a large area, it often contains multilayers of carbon, resulting in a very high resistance. Yet due to the unique 2D structure and superb conductivity, graphene has substantial potential in an alternative electrode material and we believe large-area high-quality graphene becomes available and can be used as electrodes material to effectively reduce the internal resistance (areal resistivity) of microscale MFCs in the future.

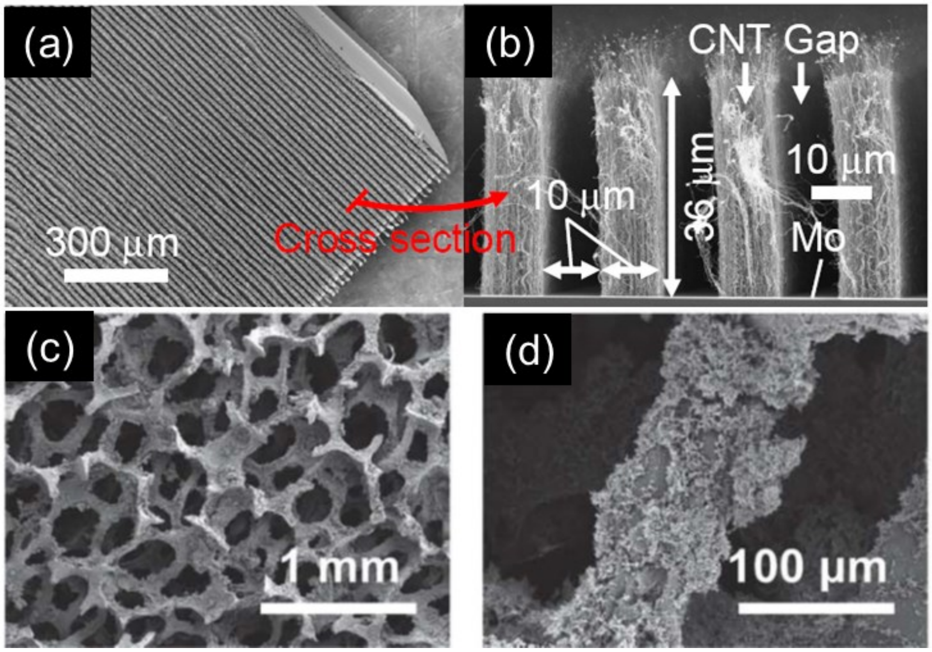

Figure 2.4. SEM images of CNT forest and graphene sponge anodes. (a, b) SEM images of biofilm on vertically aligned CNT forest electrodes presented by Inoue et al. 2012 (a) top view (b) cross section view; (c, d) SEM images of biofilm on graphene-sponge composite at different scales

Having a large electrode area is effective to lower the internal resistance as the resistance is inversely proportional to the area of electrodes. Carbon-based electrodes with a high surface area to volume ratio (for instance, graphite granules ($1100m^2/m^3$) and graphite brush ($7170\text{-}12800m^2/m^3$)) have been readily applied in macroscale and mesoscale MFCs. In microscale MFCs, carbon nanotube forest with a high surface area to volume ratio has been used as an anode material to reduce the internal resistance, as shown in Figure 2.4. Several work used microfabrication techniques to create large area to volume ratio electrodes. However, there should be a large enough distance between two microfabricated structures, such as between two carbon nanotube forests, two microfabricated trenches and pillars. The thickness of a typical biofilm is in the range of 50-100 μm. If the distance between two microfabricated structures does not allow accommodating a biofilm, clogging may occur during the formation of biofilm, depriving the advantage of large surface area to volume ratio of these structures.

The second component in ohmic resistance is the resistance associated with electrolyte and membrane. The electrolyte resistance can be reduced by increasing ions concentration in electrolyte, decreasing the distance between electrodes, and implementing separators with lower resistance.

When ions concentration of anolyte or catholyte is low, then MFC is limited by insufficient substrate, buffer or electron acceptor. On the other hand, when the concentration becomes high, exoelectrogen metabolism would be inhibited, due to high salinity. High concentrations of cations such as Na^+ and K^+ prevents the efficient transport of H^+ through membrane, resulting in acidification and consequently hampering the performance of MFC. Increasing buffer concentration, for most times, enhances the performance since it mitigates the acidification in the anolyte and biofilm. High buffer concentration can neutralize more protons accumulated in the anode chamber and can increase the mass transfer of the buffer into the biofilm to mitigate the acidification. Such approach can be implemented for microscale MFCs. Decreasing the distance between electrodes has been implemented in several macroscale MFCs, yet it can be easily implemented in microscale MFCs. Microfabrication allows miniaturizing geometrical dimensions including the distance between electrodes. For instance, Choi et al. reported a microscale MFC with a chamber thickness of only 20 μm. The ohmic resistance associated with membrane can be decreased by replacing ion exchange membrane by other porous separators, such as J-cloth, polycarbonate and nylon *etc*. with a large pore size to reduce the resistance of ions movement. Some researchers have built membraneless MFCs and successfully reported high power density. These approaches can be used for microscale MFCs to enhance their power density.

The activation overpotential exists when current density is low, in the range of 0-10 A/m^2, in chemical fuel cells, which covers main operating region of most MFCs. Although ohmic and concentration losses would prevail in this current range in MFCs, it is still critical to decrease the activation overpotential to enhance the performance.

The activation potential loss can be determined by the Tafel equation:

$$\Delta V_{act} = A \ln(\frac{i}{i_0}) \tag{2.14}$$

Here ΔV_{act}, A, I and i_o are the activation potential loss, the correlation coefficient determined by the reaction, the current density of MFC and the limit current density at which the overpotential is zero, respectively. The correlation coefficient can be calculated by:

$$A = \frac{RT}{2\alpha F} \tag{2.15}$$

Here R, T, F and α are universal gas constant ($R = 8.31\ \mathrm{JK^{-1}mol^{-1}}$), temperature, Faraday's constant ($9.65\times10^4\ \mathrm{Cmol^{-1}}$) and charge transfer coefficient, respectively. A is a function of temperature and the charge transfer coefficient, and a larger A results in smaller activation overpotential. Most MFCs operate at room temperature, thus in order to decrease the activation potential, α should be as small as possible. By adding catalyst on electrodes and redox mediator to medium α can be decreased. It is also feasible to decrease the current density, i, to lower the activation potential by increasing the surface area.

Many researchers have added catalyst on anodes and cathodes to reduce the activation overpotential. For instance, graphite anodes have been modified by electron mediators, such as Mn^{4+}, or made hydrophilic by plasma treatment or coated by polymers such as Polytetrafluoroethylene (PTFE), polypyrrole or modified by quinone groups, or treated by ammonia. On the cathode, noble metal for reducing the high overpotential for oxygen reduction, such as Pt, is coated on air-cathode MFCs as catalyst. Recently, noble metal-free catalysts, such as pyrolyzed iron phthalocyanine (FePc) or cobalt tetramethoxyphenylporphyrin (CoTMPP) were used to increase power density. Moreover, aerobic microbes were also used as bio-catalyst. Currently none of microscale MFCs has implemented catalysts for the reduction of activation overpotential. Considering the smaller power and current density in microscale MFCs which may be due to large activation loss, it is very feasible to reduce the overall internal resistance by adding catalysts on electrodes in microscale MFCs. Researchers have readily adopted materials with a larger surface area to volume ratio such as carbon cloth, carbon mesh, carbon paper, graphite fiber brush, graphite foam, graphite granules, graphite plates and sheets to reduce the activation loss. In microscale MFCs, researchers have used CNT, microfluidic channels and microfabricated pillars to increase the surface area to volume ratio to reduce the activation loss.

Concentration losses dominate when the consumption rate of substrate or oxidant in the anode or cathode chamber exceeds the rate of supply in chemical fuel cells. When the rate of substrate or oxidant supply is lower than the consumption rate of MFC operation, the current density hits the limit set by the supply. The maximum power density often can be achieved at the critical point that concentration loss begins in chemical fuel cells. In contrast, the concentration loss occurs in any operating condition in MFCs because biofilm on anode and substrate transport to the biofilm continue to change until steady state. When biofilm reaches at steady state (constant biofilm thickness and density) and produces a highest current density, mass transfer in biofilm mainly affects concentration loss. As a result, in order to reduce the concentration loss, the mass transportation of substrate, proton and oxidant should be enhanced.

Non-compatibility with microfabrication. In addition to the high internal resistance (high areal resistivity), another challenge of microscale MFCs is that manufacturing techniques involved in microscale MFCs is not completely compatible with all necessary components including membrane, gasket, and electrodes. Despite of attractive features of microfabrication, such as small size, light weight, batch fabrication and potentially low cost, the challenge of compatibility needs to be addressed to take advantage of the scaling effects on microscale MFCs.

The first and most urgent incompatibility challenge of microscale MFCs is the ion exchange membranes. So far, no microscale MFC has been fully microfabricated, primarily due to the necessity of ion exchange membranes. To address the incompatibility, we briefly explain why MFCs need ion exchange membranes.

An ion exchange membrane allows specific ions to cross while stops others. Two types of ion exchange membranes are typically used in MFCs, cation exchange membrane (CEM) and anion exchange membrane (AEM). CEMs allow only cations to pass and AEMs allow only anions to cross. The first and most famous CEM is PEM which was discovered in late 1960s by Dupont Inc. The operating principle of PEM is that on the tetrafluoroethylene (Teflon) backbone attaches hydrophilic sulfonate groups, which can transfer protons from one side to the other. The operating principle of the AEM is similar, except for the different functional group-the positive charged quaternary ammonium groups which aid the anion transport.

PEM was first used in hydrogen fuel cells during the Gemini space missions in the 1960s. Over the past 50 years, it has been widely used in fuel cells including MFCs to facilitate transport of H^+ to compensate for transport of electrons. The other role of PEM is to prevent short circuiting electrodes, the movement of exoelectrogen from anode to cathode chamber, toxic catholyte to transport into the anode chamber, and it reduces oxygen diffusion. However, as mentioned in section 2.3, an ion exchange membrane such as PEM increases internal resistance and cause acidification in anode chamber.

To address this issue, researchers have compared the performance of conventional separators, such as AEM, CEM, charge mosaic membrane (CMM) and bipolar ion exchange membrane (BEM). These works shows that the larger the pH gradient across the membrane is, the larger the internal resistance becomes. Generally AEM has better performance over other membranes, and monopolar ion exchange membranes perform better than BEM. Other separators have also been researched, such as ultrafiltration, Zirfon, J-cloth, glass wool, nylon, cellulose and polycarbonate. These work show that nylon, polycarbonate and glass wool perform better than traditional ion exchange membranes, and Zirfon has comparable performance as Nafion and ultrafiltration do not perform as good as AEM/PEM. It is interesting that the thinner and more porous the membrane is, the higher the power density and the lower the CE become.

Unfortunately none of aforementioned ion exchange membranes seem to be compatible with microfabrication. However, it is useful to look for an alternative such as thin nanoporous PMMA or PDMS which are compatible with microfabrication. These materials can be used for separators upon surface modifications, similar nanoporous nylon and polycarbonate, which were reported to achieve higher power density than Nafion. From the FESEM images of nylon, polycarbonate and Nafion shown in Figure 2.5(a)-(c), the pore size of nylon and polycarbonate is in the order of 200 nm, 40 folds larger than that of Nafion, and the larger pore size results in higher power density due to smaller resistance and alleviation of acidification.

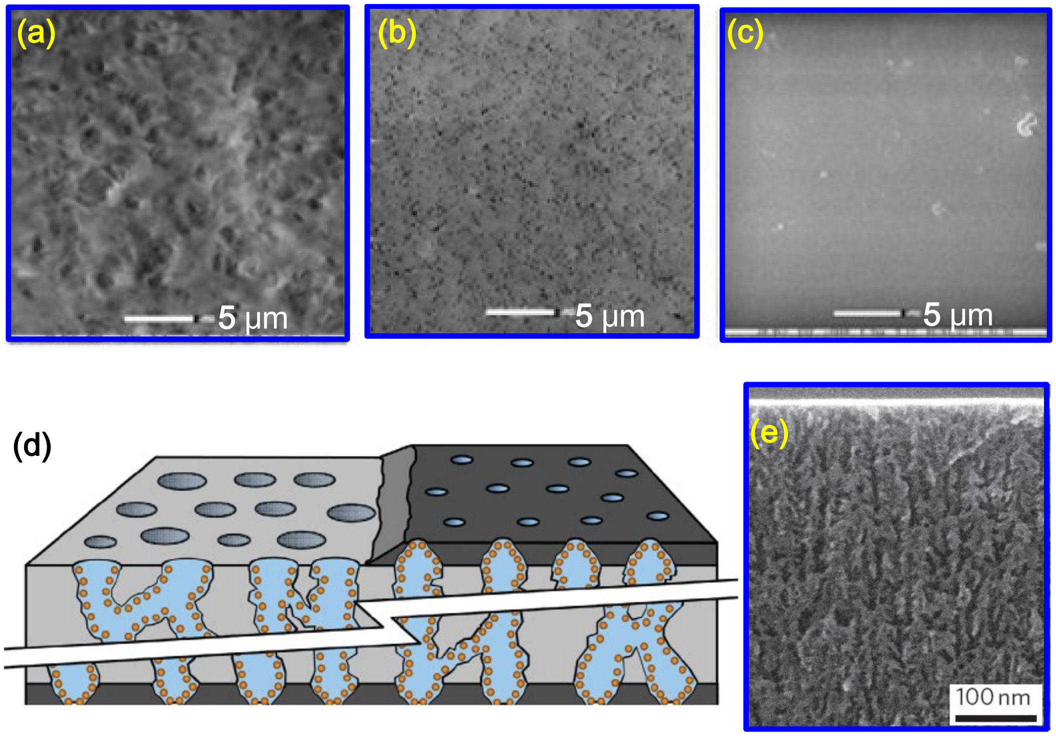

Figure 2.5. Ion exchange membranes. (a)(b)(c): FESEM images of nylon, polycarbonate and Nafion, the pore size of nylon and polycarbonate is in the order of 200 nm, 40 folds larger than that of Nafion (d) Schematic of the membrane with functionalized pore wall and thin layers of porous silica on both sides of the membrane (e) Cross-sections of the porous silicon membrane (front view)

Another alternative to replace conventional ion exchange membranes is nanoporous silicon membrane. Nanoporous silicon membrane has been implemented in PEM fuel cells due to its compatibility with microfabrication, stability at elevated temperatures, higher proton conductivity and free from volumetric size change. One of the first nanoporous silicon membranes, reported in 2004, has 5-20 nm nanopores fabricated by anodic etching of bulk silicon, which has comparable conductivity and formic acid permeability to Nafion. The nanoporous silicon membrane was optimized by the same group through adding self-assembled monolayer on nanoporous silicon with pore size of 5-7 nm, and then capping the SAM layer by a layer of porous silica, as shown in Figure 2.5 (d)-(e). Moghaddam et al. reported the nanoporous membrane produced one order of magnitude higher in power density than that of using Nafion[18]. So far, nanoporous silicon has not been used in MFCs and we believe nanoporous silicon membrane brings not only compatibility with microfabrication, but also high proton conductivity that mitigates the acidification in MFCs.

A gasket defines anode and cathode chambers, and holds a challenge to be microfabricated. PDMS was often used as a gasket material for microscale MFCs as it is compatible with microfabrication, easy to manipulate the film thickness, low cost, and it is biocompatible and nontoxic, which is critical for exoelectrogen growth. Elastomeric properties of PDMS allow it to conform to smooth, nonplanar surfaces and release from delicate features of the mold without damage. PDMS patterned by soft lithography has been used by many researchers. However, due to its high oxygen permeability, as high as PBS (phosphate buffered saline), the reported CE of a MFC was very low. Other alternatives have been reported such as defining chambers by deep reactive ion etching bulk silicon and fabricating gasket by electroplating metal, including Nickel. Both methods have potential to reduce the oxygen effect as silicon and metal has very low oxygen permeability.

Currently most microscale MFCs use a thin layer of metal film, such as gold as electrode material, mainly because these materials are readily used in microfabrication. Microscale MFCs suffer from high internal resistance (high areal resistivity), and this motivates researchers to explore using carbon-based materials for electrodes. However, most carbon materials are not fully compatible with microfabrication as conventional carbon materials are not ideal for microscale MFCs. 1D and 2D carbon-based materials-carbon nanotubes (CNT) and graphene are compatible with microfabrication and have potential to solve the challenge of high internal resistance.

Mitigation of oxygen intrusion. As discussed in section 1.2, the operation principle of MFCs is to let exoelectrogen respire at the anode and transfer electrons to the anode. When oxygen is presents in the anode chamber, which is often the case as it is difficult to completely eliminate oxygen leakage, oxygen scavenges electrons produced by exoelectrogen as oxygen has higher potential than the anode. This results in lowering CE and it is typically accompanied by a decrease in current density.

Unlike *Geobacter* species, *Shewanella* species suffer less from the oxygen leakage, and in fact they benefit from oxygen, as discussed in section 1.1. It is reported that under aerobic conditions the maximum power and short circuit current of a MFC using *Shewanella oneidensis* were approximately three times greater than those under anaerobic conditions. They attributed this effect as some genes or enzymes can be activated under aerobic conditions, which can help substrate utilization and finally more electrons are delivered to the anode. For instance, under anaerobic conditions, lactate is oxidized to acetate (acetate cannot be further oxidized under anaerobic conditions), and only 4 electrons are produced by one lactate molecule (one third of the stored electrons) for power generation. In contrast, under aerobic conditions *Shewanella* can oxidize acetate, thus producing 12 electrons per lactate molecule.

Microscale MFCs using *Geobacter* species, which are strict anaerobes, face an even severe challenge of oxygen diffusion to the anode as microscale MFCs may have smaller population of *Geobacter* and higher mass transfer coefficient. From Figure 2.2 and 2.3, CE of microscale MFCs are in the range of 0.03 – 31 %, much lower than that of macro/mesoscale MFCs of 42.5 - 81 %. It is urgent to alleviate the oxygen leakage in microscale MFCs using *Geobacter* in order to increase CE of microscale MFCs. A few potential approaches are proposed in the following paragraphs to circumvent this challenge.

The first approach is to use materials with lower oxygen permeability for construction of microscale MFCs. Most microscale MFCs reported so far uses PDMS. However, the oxygen permeability of PDMS is as high as water. The oxygen permeabilities of PDMS, silicone rubber and Polytetrafluoroethylene are substantially higher than those of other materials, such as parylene C, epoxy, PET (Polyethylene Terephthalate), metal, bulk silicon and glass. Here note that parylene C has been readily used in microfabrication and it has very low oxygen permeability; we believe parylene C is an excellent candidate for microscale MFCs.

The other approach is to use hermetic packaging which has been widely implemented in MEMS. Hermetic packaging can be accomplished by either ceramic packaging or polymer packaging. Ceramic packaging performs better in air tight and anti-interference ability, yet requires higher cost than polymer packaging. Perhaps one can use a low oxygen permeability material such as PTFE for microscale MFCs. Unlike traditional MEMS devices, microscale MFCs require microfluidic interfaces which certainly add additional challenges in hermetic packaging.

In order to mitigate the oxygen leakage, some researchers have attempted to add an oxygen scavenger, L-cysteine, into anolyte as it scavenges the dissolved oxygen. Choi et al. analyzed the influence of the addition of L-cysteine in anolyte on OCV in microscale MFCs. OCV of MFC with L-cysteine in fed-batch mode is around 600 mV, much higher than that without with L-cysteine, which is around 300 mV. This suggests the addition of L-cysteine in anolyte can alleviate oxygen leakage and reduce the potential loss, consequently enhancing the power density and CE.

By adding some aerobic microbe in the anode chamber may also mitigate the oxygen leakage by scavenging oxygen in anolyte and breaking down complex organic substrate which conventionally cannot be readily used by exoelectrogen. Investigating the positive syntrophic relations between some aerobic microbe and the exoelectrogen may mitigate the oxygen leakage and enhance the power generation, similar with the positive syntrophic relationship between exoelectrogen and homo-acetogens found in MECs and microbial electrochemical systems (MXCs).

One can use membranes with less oxygen mass transfer coefficient to alleviate the oxygen effect. However, more often this approach may result in a poor transport of proton and adds to the acidification of anolyte. Thus, a trade off exists as one wants to replace membranes. It is possible to develop membranes with low oxygen mass transfer coefficient yet high ion transfer coefficient; however, the small size of oxygen molecule is the challenge in this development. As proton has the smallest size in all atoms maybe one can develop a membrane having a high mass transfer coefficient and a very small pore size which only permits proton to pass, yet this approach imposes another severe challenge: the larger the pore size in a membrane becomes, the higher the power density of MFCs is.

CHAPTER 3

IMPROVED CURRENT AND POWER DENSITY WITH A MICRO-SCALE MICROBIAL FUEL CELL DUE TO A SMALL CHARACTERISTIC LENGTH

3.1 Introduction

An MFC is an electro-chemical device to convert organic compounds into electrical current. Key to MFCs is that they employ anode-respiring bacteria (ARB) as living catalysts at the anode [37, 53]. Unlike other techniques to convert organic material to electricity, the MFC is unique because it allows direct electricity generation [7]. The organic fuel for MFCs most often comes from wastewater, making the MFC a waste-to-energy technology that have led efforts to scale up MFCs [7, 29, 54]. In addition, MFCs hold promise for bioremediation of recalcitrant compounds [55] and supplying power for remote sensors in hazardous or hard-to-access conditions [56].

For remote applications, an interesting direction is miniaturizing MFCs: decreasing the characteristic length to the micrometer range, resulting in chamber volumes of 100s of μL [56]. Miniaturizing MFCs takes advantages of microfabrication [57, 58, 59, 60], adopted from standard integrated-circuits fabrication, which allows small-sized chip-scale devices for powering ultra-low-power electronics, especially in remote conditions [43, 56, 61]. Our prior work [44] reports the highest areal power density, up to 0.33 W/m^2, in a micro-scale MFC, but it is still far lower than that of macro-/meso-scale counterparts (up to 6.80 W/m^2) [62].

We utilize the ARB *Geobacter* because of their proven ability to deliver a high power density. *Geobacter* oxidize acetate at the anode to release electrons and protons:

$$CH_3COO^- + 2H_2O \rightarrow 2CO_2 + 8e^- + 7H^+ \qquad (3.1)$$

Acetate first must be transported from the bulk liquid to the biofilm, and then it diffuses into the biofilm, where it gets oxidized. Electrons are conducted to the anode and then pass through an external circuit to arrive at the cathode, where they reduce an oxidant. In our case, they reduced ferricyanide to ferrocyanide.

$$[Fe(CN)_6]^{3-} + e^- \rightarrow [Fe(CN)_6]^{4-} \qquad (3.2)$$

Ions also move from the anode to the cathode via the liquid medium and a proton exchange membrane (PEM) is to establish charge neutrality. Among the ions, the most critical one is the proton (H^+). Eq. 3.1 shows that 7 moles H^+ are produced per mole acetate; these H^+ must be transported out of the biofilm to avoid acidifying the biofilm, which retards the rate of biological reaction [63, 64]. The protons combine with an acid/base buffer, which diffuse out of the biofilm. Thus, increasing the mass-transport rate of the H^+ carrying buffer should improve MFC performance.

Here, we present a micro-scale, flat-plate MFC with a high surface area to volume ratio, which we postulate will enhance mass transfer of acetate and H^+-carrying buffer. Fig. 3.1 gives a schematic of the MFC. It has a PEM and two silicone gaskets sandwiched between two glass slides pre-fabricated with gold electrodes. One rectangular hole is patterned in each gasket, and they define the anode and cathode chambers with identical dimensions. Two nanoports provide microfluidic pathways for anolyte and catholyte that flows through the corresponding chambers, as shown in Fig. 3.1 (b). W and L are the lateral dimension and height of the cross-section of chambers, respectively. L is designed to be much smaller than W, resulting in a very high surface-area-to-volume ratio for each chamber. Furthermore, L is very small to make the distance between the anode and the cathode small.

Scaling down the characteristic length of a micro-scale MFC ought to result in increased mass transport, consequently enhancing the MFC's current and power density. When mass transport is limiting, the maximum current density is proportional to the flux defined by the diffusion of substrate or products to the electrode, as defined by

$$j_L = nFD\frac{\Delta C}{\lambda} \tag{3.3}$$

where n is the number of electrons equivalents corresponding to the limiting compound, F is the Faraday constant (96485 C/mol e^-), D is the normalized diffusivity of the limiting compound, ΔC is the concentration gradient of the limiting compound, and λ is the diffusion layer thickness. j_L can increase if λ is minimized in the MFC, thus increasing the possible power density obtained. A miniaturized MFC may benefit from faster mass transfer due to its inherently smaller L [65, 66]. In a laminar flow, likely in microfluidic environments[67], the Reynolds number, Re, and the mass transfer coefficient, k_c [m/s], can be defined as [68]:

$$Re = {}^{\rho v d_h}\!/_{\mu} \quad \text{and} \quad k_c = 0.664({}^{\rho v d_h}\!/_{\mu})^{1/2}({}^{\mu}\!/_{\rho D})^{1/3}(D/L)$$

(3.4)

where *ρ, v, d_h, L, μ, and* are the specific density of the fluid, the linear velocity of the fluid, the hydraulic diameter of the anode chamber, the characteristic length, the viscosity of the fluid, respectively. The hydraulic diameter is calculated by:

$$d_h = 4A/p \tag{3.5}$$

where $A = WL$ and $p = 2(W+L)$ are area and wetted perimeter of the cross section of the anode chamber, respectively. W and L are the lateral dimension and height of the cross section of chamber. L is also the characteristic length of the anode chamber, and the hydraulic diameter (d_h) becomes twice the characteristic length (L) when the lateral dimension of the anode chamber dominates the height (W>>L), which prevails in micro-scale MFCs. Based on Eq. 3.4, k_c should become larger as the linear velocity (v) increases or the characteristic length (L) decreases.

The diffusion-layer thickness, λ, can be calculated by:

$$\lambda = \frac{D}{k_c} = \frac{L}{0.664({}^{\rho v d_h}\!/_{\mu})^{1/2}({}^{\mu}\!/_{\rho D})^{1/3}} \tag{3.6}$$

Because d_h becomes $2L$ when the lateral dimension of the anode chamber dominates the height (W>>L), λ is proportional to $L^{1/2}$; hence, λ decreases as the characteristic length scales down, resulting in smaller diffusion-layer resistance. Fig. 3.2 illustrates how scaling down L, with all other parameters unchanged, causes the mass transfer coefficient to increase and the diffusion layer thickness to decrease at 5 μL/minute.

In summary, downscaling the characteristic length enhances the surface area to volume ratio and mass transfer coefficient, consequently improving the power density of a micro-scale MFC. The next section addresses the implementation of a micro-scale MFC to adopt the scaling effect on the characteristic length, including the fabrication of the micro-scale MFC and the experimental procedures. Then, the power density of the micro-scale MFC is evaluated, demonstrating both scaling effects.

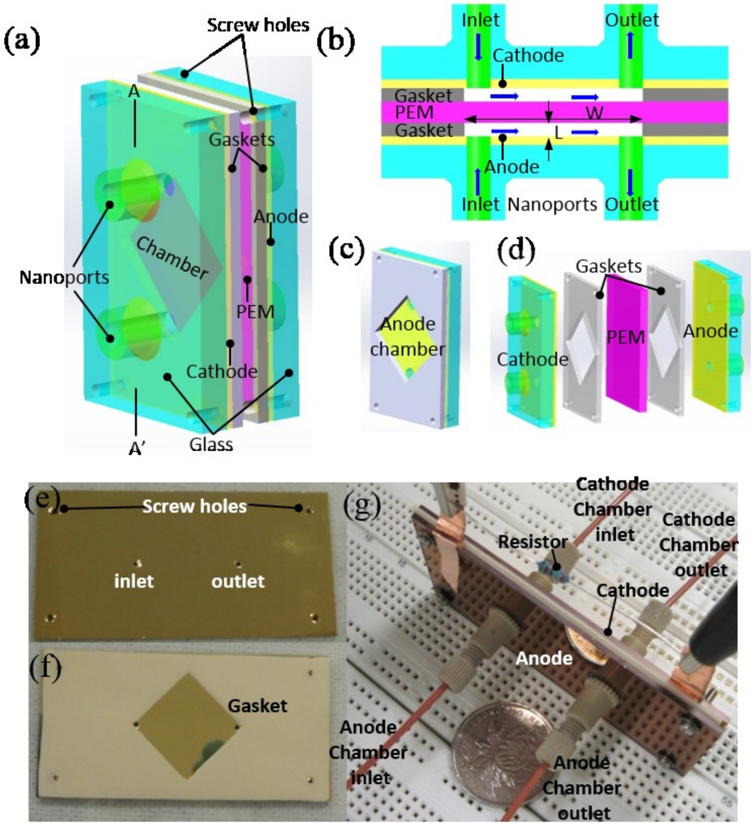

Figure 3.1. Schematic and images of the micro-scale MFC. (a) A lateral view of the MFC after assembly; (b) Cross-sectional of (a) via plane A-A', the height of the chambers is L and the width of the chambers is W, blue arrows indicate the

direction of anolyte and catholyte; (c) anode chamber defined by the gasket; (d) the different parts of the MFC before assembly; (e) Cr/Au electrode on top of a glass slide; 6 holes (one for inlet, one for outlet, and 4 for screws) mechanically drilled through the glass; (f) silicon gasket mounted on top of the Cr/Au electrode to define the anode/cathode chamber; (g) assembled MFC with microfluidic ports for inlet/outlet for anode/cathode chambers.

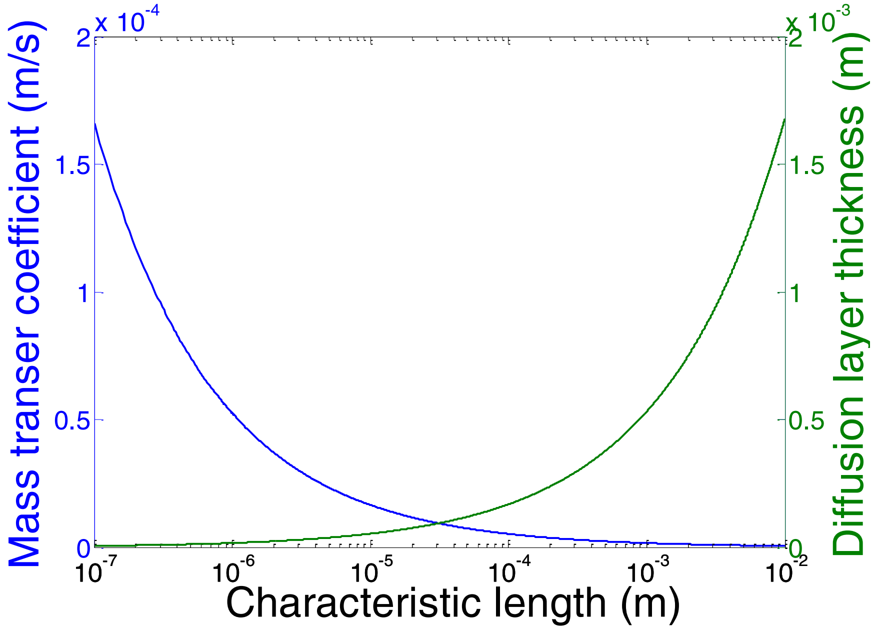

Figure 3.2. Scaling effect for micro-scale MFCs. Moving from L = 1 cm to L = 0.1 μm increases mass transfer coefficient from 5.2×10^{-7} to 1.7×10^{-4} m/s, and lowers diffusion layer thickness from 1.7×10^{-3} to 5.3×10^{-6} m. Fig. 2: Scaling effect for micro-scale MFCs; moving from L = 1 cm to L = 0.1 μm increases mass transfer coefficient from 5.2×10^{-7} to 1.7×10^{-4} m/s, and lowers diffusion layer thickness from 1.7×10^{-3} to 5.3×10^{-6} m.

3.2 Materials and Methods

Micro-scale MFC fabrication. MFC fabrication began with mechanically drilling six through holes on two glass slides (micro slides, 76 × 38 × 0.12 cm^3, VWR): one inlet, one outlet, and four for assembly. Afterwards, Cr/Au (20 nm/200 nm) was deposited by sputtering on the anode/cathode (Fig. 3.1(e)). Then, the nanoports (10-32 coned, IDEX) and fluidic tubing (PEEK polymer, IDEX) were aligned and glued to the inlets/outlets to supply anolyte and catholyte. Silicone rubber gaskets were patterned to define the chamber and electrode (Fig. 3.1(f)), and the PEM (Nafion 117) was cut to have the same dimension as the electrode. Finally the MFC was assembled with four screw bolts and four nuts to minimize oxygen/electrolyte leakage (Fig. 3.1(g)). The volume of each chamber was 100 μL, and the size of electrode was 4 cm^2.

Inoculum. The inoculum for the micro-scale MFC was obtained from an acetate-fed MEC that had a *Geobacteraceae*-enriched bacterial community originally enriched from anaerobic-digested sludge from the Mesa Northwest Water Reclamation Plant (Mesa, AZ). Clone libraries of the 16S-rRNA gene showed that the biofilm anode was a mixed bacterial culture dominated by *Geobacter sulfurreducens* [69]. The anolyte was 25 mM sodium acetate medium with 1,680 mg KH_2PO_4, 12,400 mg Na_2HPO_4, 1,600 mg NaCl, 380 mg NH_4Cl, 5 mg EDTA, 30 mg $MgSO_4 \cdot 7H_2O$, 5 mg $MnSO_4 \cdot H_2O$, 10 mg NaCl, 1 mg $Co(NO_3)_2$, 1 mg $CaCl_2$, 0.001 mg $ZnSO_4 \cdot 7H_2O$, 0.001 mg $ZnSO_4 \cdot 7H_2O$, 0.1 mg $CuSO_4 \cdot 5H_2O$, 0.1 mg $AlK(SO_4)_2$, 0.1 mg H_3BO_3, 0.1 mg $Na_2MoO_4 \cdot 2H_2O$, 0.1 mg Na_2SeO_3, 0.1 mg $Na_2WO_4 \cdot 2H_2O$, 0.2 mg $NiCl_2 \cdot 6H_2O$, and 1 mg $FeSO_4 \cdot 7H_2O$ (per liter of deionized (DI) water) (pH 7.8 ± 0.2). For start-up, inoculum and anolyte were mixed with a volume ratio of 1:1. The catholyte was 100 mM potassium ferricyanide in 100 mM phosphate buffer solution. The anolyte and catholyte were supplied into the micro-scale MFC using a syringe pump. The MFC operated at 25°C.

Operation and analysis. The current was monitored every minute by recording the voltage drop across an external resistor connected between the anode and the cathode using a data acquisition system (DAQ/68, National Instrument). During start-up process, a 148 Ω resistor was used, and the MFC operated at a flow rate of 1 μL/minute through each chamber. Once the start-up was completed, the flow rate, controlled by a syringe pump, was increased for a series of steady states at which polarization measurements were performed. To generate polarization curves, we measured voltage using a series of resistors from 148 Ω to 932 kΩ. The current through the resistor was calculated via Ohm's law ($I = U/R$, where I, U, and R are current, voltage and resistance, respectively), and the resulting output power was calculated via Joule's law ($P = I^2R$). The MFC's internal resistance was calculated by linearly fitting the Ohmic region, i.e., when the voltage drop (ΔU) was approximately linear with the increase of current (ΔI) of each curve of areal current density versus voltage across external resistor [54]: i.e., $R = \Delta U/\Delta I$.

The minimum CE of the micro-scale MFC was computed by integrating current profiles over the time [54] and dividing this cumulative current (C_p) by the current that could have been produced if all the influent acetate had been oxidized to produce current ($C_T = V \times b \times N_A \times e \times [\text{mol}_{\text{substrate}}]$): $CE = C_P/C_T \times 100\ \%$, where V is the volume of anode chamber [m^3], b is the number of moles of electrons produced by oxidation of substrate [8 mol e$^-$/mol acetate], N_A is Avogadro's number [6.023×10^{23} molecules/mol], e is electron charge [1.6×10^{-19} C/electron], and $mol_{substrate}$ is the moles of acetate oxidized.

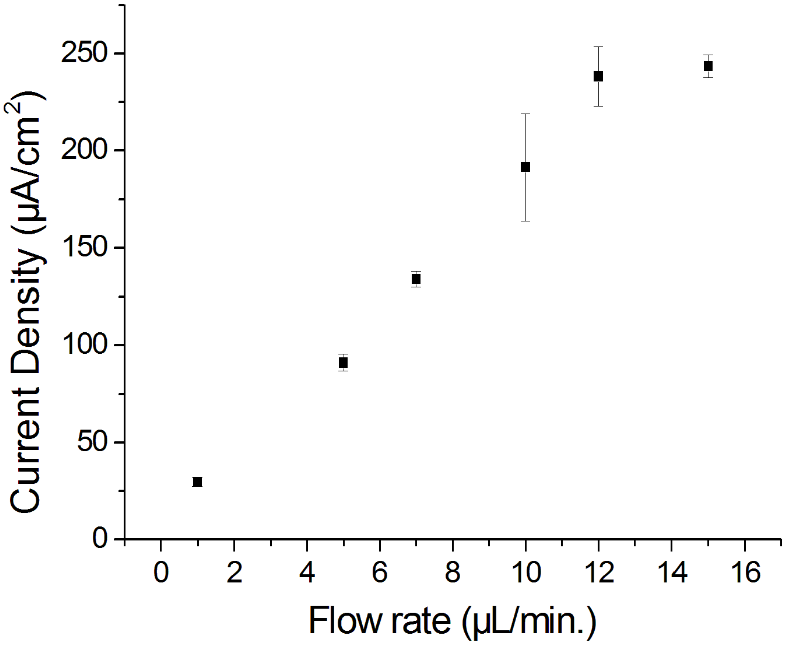

Figure 3.3. Current density as a function of different flow rates using a 148-Ω external resistor. The current density almost linearly increased with flow rate and up to 12 µL/min.

It took 6 days to complete the start-up process, at which time the current density exceeded 20 µA/cm^2. After start-up process, the flow rate was increased from 1 to 15 µL/minute to characterize the power density as a function of flow rate. Fig. 3.3 shows the current density recorded at different flow rates using a 148 Ω resistor. The current density increased almost linearly with the flow rate up to 12 µL/minute, where it saturated. The current density declined when the flow rate was further increased to 17 µL/minute due to cathode erosion from ferricyanide etching the cathode. SEM images of the biofilm at the end of the experiments showed a range of aggregation patterns on the anode surface, with an average coverage ratio of 30% and a per-cell electro-generation rate of about 10^6 electrons/second.

High flow rate in the MFC anode is not always synonymous with a decreased number of ARB on the anode surface, unless it is coupled with high shear rate and other advective flow patterns that promote detachment from biofilm surfaces. Previous studies have documented the ability of *Geobacteraceae* cells to accumulate to high cell numbers on the biofilm anode at high flow rates (or low hydraulic retention times (HRTs)) compared to this study [70, 71].

The voltages for a series of external resistors were recorded for fixed anolyte flow rates. Then, polarization curves (Fig. 3.4) were obtained from the data. The curves of the output voltage versus current density, Fig. 3.4(a), show a high OCV of 0.81 V. The internal resistances were calculated by linearly fitting the Ohmic region (i.e., where the voltage drop (ΔU) is approximately linear with the current density (ΔI)) for each individual polarization curve (Fig. 4(a)). The curves show similar internal resistances of the micro-scale MFC, independent of the flow rate (2.1 kΩ). However, the limiting current, j_L changed significantly from 91 μA/cm^2 at 5 μL/min. to 240 μA/cm^2 at 15 μL/min. These experiments confirm that a transport limitation to or from the bulk liquid limited the total current density produced by the *Geobacter*-enriched biofilm. Similar conclusions have been recently reached at using nuclear magnetic resonance techniques and rotating disk electrodes [72].

The mass-transfer rate is a product of the concentration difference and mass transfer coefficient. As a result, mass transfer is enhanced when the concentration and linear velocity of electrolyte are increased. Fig. 3.4(a) clearly shows current limitation for the lower flow rates, suggesting that the maximum current produced by *Geobacter*-enriched biofilm was controlled by a diffusive process. In a separate experiment, the total salts concentrations of the anolyte and the catholyte, with the exception of the anode buffer, were increased stepwise from 1 × to 1.5 × and to 2 ×. The concentration increase did not improve the areal power density (data not shown). This finding confirms that the transport of substrate was not limiting, and the only possible diffusion limitation was due to buffer transport at the anode biofilm. Proton transport limitations has been demonstrated previously due to the high proportion of H^+ produced by ARB (as shown in Eq. 3.1) [64, 73]; our studies provide further evidence of the limitations. Our micro-scale MFC provides a design in which such limitations can be minimized by increasing the flow rate conditions.

The curves of the areal power density as a function of current density for different flow rates, Fig. 3.4(b), demonstrate that the areal power densities were almost independent of flow rates at low current densities, but reached a higher j_L as the flow rate increased. The areal power density at 5 μL/minute. reached its maximum power density (44 $\mu W/cm^2$) at a low current density of 71 $\mu A/cm^2$, whereas that of 15 μL/min. had a maximum power density of 84 $\mu W/cm^2$ at a high current density of 214 $\mu A/cm^2$. This trend can be attributed to a higher rate of mass-transfer of deprotonated buffer (e.g., HPO_4^{2-}) into the anode's biofilm, providing more rapid transport of acetate to *Geobacter*-enriched biofilm and H^+-carrying buffer out of the biofilm (e.g., $H_2PO_4^-$) [74].

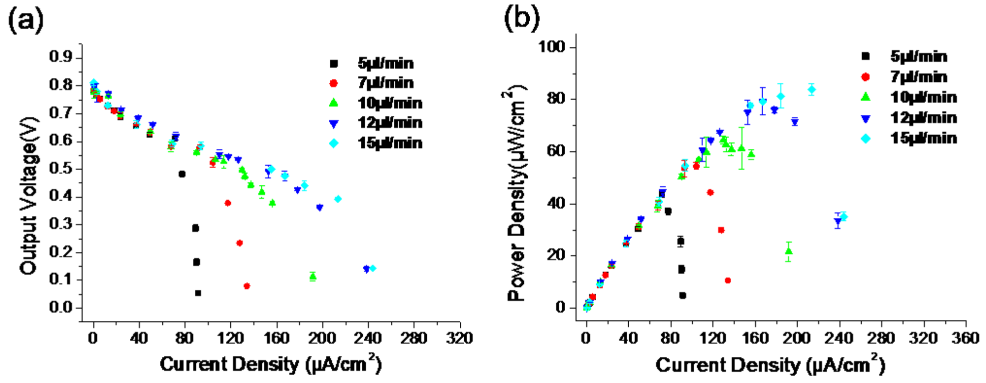

Figure 3.4. Polarization curves for the MFC at different flow rates. (a) output voltage versus areal current density; (b) areal power density versus areal current density.

The theoretical laminar mass transfer coefficient was calculated from Eq. 3.4, and it is compared in Fig. 3.5 to the current density obtained through the polarization curves in Fig. 3.4. The computed mass transfer coefficient of the limiting compound correlates well with the current density for the different flow rates. This further supports that the increased current density arose from enhanced mass transfer. We analyzed the computed mass transfer coefficient and found it to be consistent with the measured current and kinetics for acetate utilization.

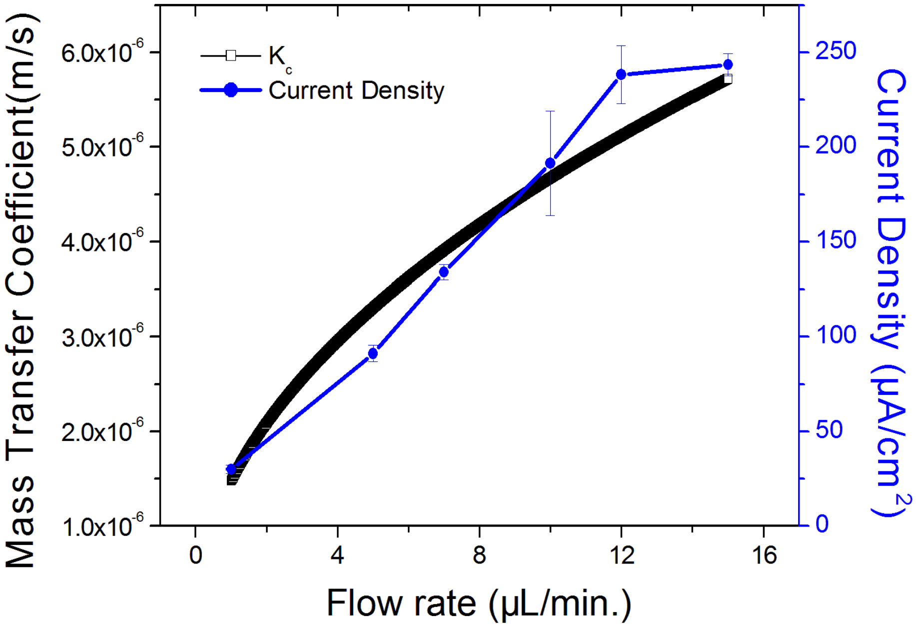

Figure 3.5. Mass-transfer coefficient of limiting compound (assuming normalized diffusivity of limiting compound is 0.76 m^2/day) and maximum areal current density versus flow rate. The maximum areal current density increases proportionally to the mass transfer coefficient.

Coulumbic efficiency (CE) is a measure of how efficiently an MFC harvests electrons, and low CE has been a challenge for micro-scale MFCs [43, 56]. The maximum CE reported by micro-scale MFCs so far is 31% [43], which is significantly lower than that of macro- and meso-scale MFCs, which often reach a CE higher than 80% [75]. The low range of reported CE values for micro-MFCs (0.03 to 31% [56]) is believed to be primarily due to high oxygen leakage into the anode chamber [43].

Anolyte flow was stopped and current over time domain was monitored while the catholyte kept flowing [43]. The minimum CE was 79%, at least 2.5 fold greater than previously reported CE for micro-scale MFCs; it is comparable to that of macro-/meso-scale MFCs. Thus, the anode chamber in our micro-scale MFC was well isolated from oxygen in the air. The micro-scale MFCs reported previously had PDMS for their gaskets, which is a common microfabrication material due to its low expense. However, PDMS is extremely oxygen permeable ($52{,}531 \pm 1{,}313\ \mathrm{cm^3 \cdot mm/m^2 \cdot day \cdot atm}$) [56]. This work eliminated the use of PDMS and deployed glass and silicon gasket as alternatives, which lowered oxygen permeability substantially.

Fig. 3.6(a) compares the volumetric power density and CE of this work with those of reported macro-/meso- and micro-scale MFCs. Our micro-scale MFC obtained 3,300 $\mu W/cm^3$, the highest volumetric power density for all MFCs, regardless of scale. Fig. 3.6(b) lists the key performance parameters of this work compared with those of prior art. Notable is the high volumetric power density, which is due to the very small characteristic length, resulting in the high SAV of the micro-scale MFC and relatively fast mass transfer. The corresponding areal power density was 83 $\mu W/cm^2$, also the highest among all micro-scale MFCs. As noted before, our micro-scale MFC achieved a CE of 79%, more than 2.5 times higher than that of the micro-scale MFCs and is comparable to the CE of macro/meso-scale MFCs.

(a)

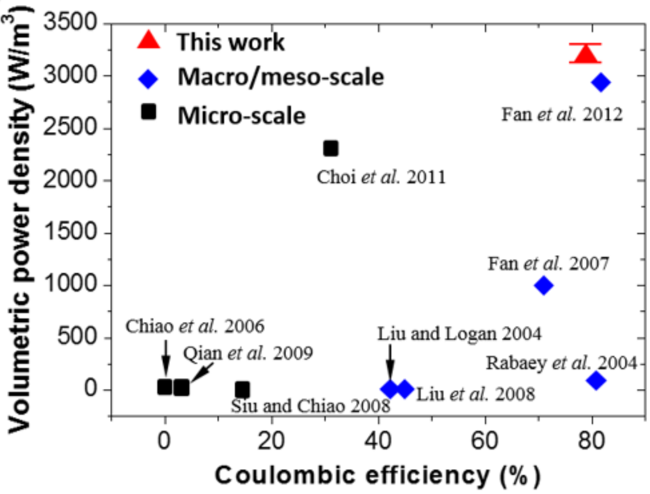

(b)

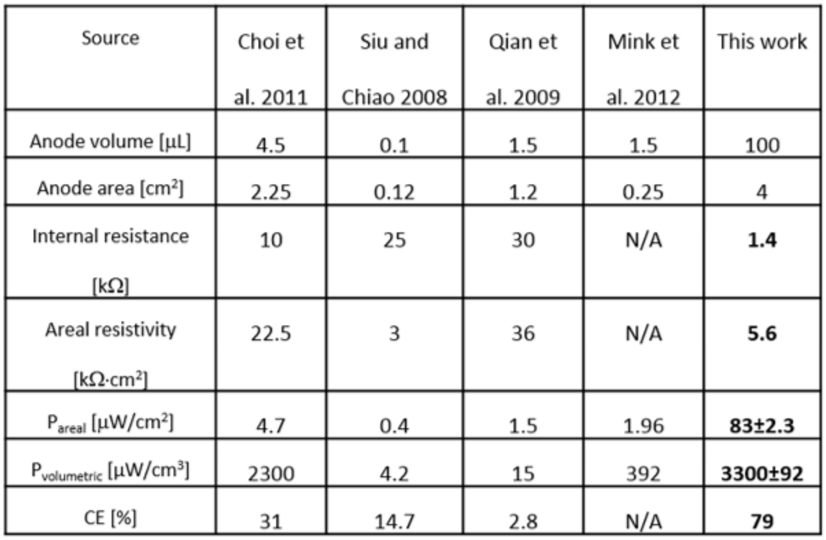

Source	Choi et al. 2011	Siu and Chiao 2008	Qian et al. 2009	Mink et al. 2012	This work
Anode volume [μL]	4.5	0.1	1.5	1.5	100
Anode area [cm^2]	2.25	0.12	1.2	0.25	4
Internal resistance [kΩ]	10	25	30	N/A	**1.4**
Areal resistivity [kΩ·cm^2]	22.5	3	36	N/A	**5.6**
P_{areal} [μW/cm^2]	4.7	0.4	1.5	1.96	**83±2.3**
$P_{volumetric}$ [μW/cm^3]	2300	4.2	15	392	**3300±92**
CE [%]	31	14.7	2.8	N/A	**79**

Figure 3.6. A Comparison of performance of the microscale MFC with prior arts. (a) Comparison of volumetric power density and CE of this work with existing macro-/meso- and micro-scale MFCs[43, 75, 76, 77, 78, 79, 80, 81, 82]; the CE of this work is substantially higher than those of micro-scale MFCs and is comparable with those of macro-/meso-scale MFCs, and the volumetric power density of this work is highest ever reported, regardless of scale; (b) specifications and performance of prior micro-scale MFCs and the MFC of this work (based on relative standard deviation (RSD)).

High internal resistance could still be a stumbling block for further enhancement of micro-scale MFCs. Our earlier work showed that the cathode/PEM/electrolyte resistance is low (all less than 100 $\Omega\cdot\text{cm}^2$) [43]; thus, in our current micro-scale MFC, the anode overpotential seems to dominate the overall potential losses at high current densities due to the limiting transport of buffer that counteracts proton accumulation, as shown in Fig. 3.4. Increasing the linear velocity in micro-scale MFCs can be a simple alternative to maximize current and power densities in MFCs.

The high power density and CE of the micro-scale MFC may find its application in powering sub-100 μW electronics, such as passive radio frequency Identification (RFID) tags, ultra-low power wireless sensor network and ultra-low power microcontroller unit (MCU), especially for applications in remote or hazardous conditions, where conventional powering units are hard to establish. Micro-scale MFCs also may be attractive in space exploration for power supply and waste treatment.

CHAPTER 4

A HIGH POWER DENSITY MINIATURIZED MICROBIAL FUEL CELL HAVING CARBON NANOTUBE ANODES

4.1. Introduction

Amidst global warming and the energy crisis, there has been significant interest in the development of sustainable energy sources[83]. Bioenergy could potentially constitute a large part of the renewable energy portfolio, provided that the Earth's abundant biomass can be economically converted[84]. Unlike conventional biomass energy conversion techniques, a MFC is an electro-chemical fuel cell which directly converts chemical energy of organic compounds to electrical energy through catalytic reactions of specific microbes called exoelectrogens or anode-respiring bacteria[37, 53, 85]. This direct conversion process allows electricity to be generated without intermediate products or equipment, and benefits MFCs' high energy conversion efficiency. During the past few decades, various types of MFCs have been reported in applications for wastewater treatment and renewable energy production[7, 29, 86, 87, 88], bioremediation of toxic components[89, 90], and power supplies for remote sensors in hazardous or environmentally unfriendly conditions[20].

Researchers have adopted different materials, such as carbon cloth, carbon mesh, graphite felt, foam, fiber brush, reticulated vitreous carbon, tungsten carbide powder, *etc*., which have a high SAV as well as mechanical and electrochemical stability[32, 81, 91, 92, 93, 94]. Recent research has been focusing on implementing two dimensional (2D) and three dimensional (3D) nanostructured materials with high SAV such as carbon nanotubes (CNT) and graphene. CNT and graphene are two nanostructured carbon allotropes, which are attractive materials due to their high SAV, high conductivity, excellent electrochemical characteristics, superb mechanical and chemical stability, and manufacturing compatibility with batch-mode microfabrication[49, 95, 96, 97]. Both CNTs and graphene have been used as 2D and 3D carbon based anode materials for MFCs, such as in graphene sponge[98], reduced graphene oxide on carbon fiber[99], CNT/polyaniline or CNT/chitosan composite[50, 100], multi-walled CNT[52, 101, 102], polyaniline hybridized graphene[103], chitosan/vacuum-stripped graphene scaffold[104], 3D graphene on Ni foam[105, 106], and reduced graphene oxide/CNT coated scaffold[107], resulting in a SAV as high as 20,000 m^{-1}; however, the reported maximum areal power density ranges from 19 mW m^{-2} to 1.57 W m^{-2}. Based on the projected electrode area, the volumetric power density ranges from 6.3 W m^{-3} to 392 W m^{-3} [98, 101, 108], which still does not have a significant leap over conventional MFCs. Moreover, the biocompatibility of CNTs remains questionable[109] and some prior studies of CNT-based MFCs show lower performance than MFCs having anodes of conventional carbon-based materials[50, 51, 52, 110]. Besides implementing high SAV materials as anode, the cathode impacts the performance of MFCs significantly as well - especially air-cathode MFCs [30]. CNTs and graphene based materials have also been used as cathodes materials in air-cathode MFCs, of which the cathode becomes the bottleneck, as reported by Wang *et al.* 2011 and Khilari *et al.* 2013 [111, 112].

Miniaturized MFCs reduce the characteristic length scales of MFCs to the micrometer range, which results in chamber volumes which are on the µL scale[25, 39, 42, 45, 56, 108]. In this chapter, we report the formation and morphology of biofilm on three different CNT-based electrode materials, and correlate the biofilm formation and morphology to the characteristics of the miniaturized MFC, including coulombic efficiency and areal/volumetric power density. The three types of anodes using CNT materials with different sheet resistance and morphology are: (1) Vertically Aligned Carbon Nanotubes (VACNT), (2) Randomly Aligned Carbon Nanotubes (RACNT), and (3) Spin-Spray Layer-by-Layer Carbon Nanotubes (SSLbL CNT).

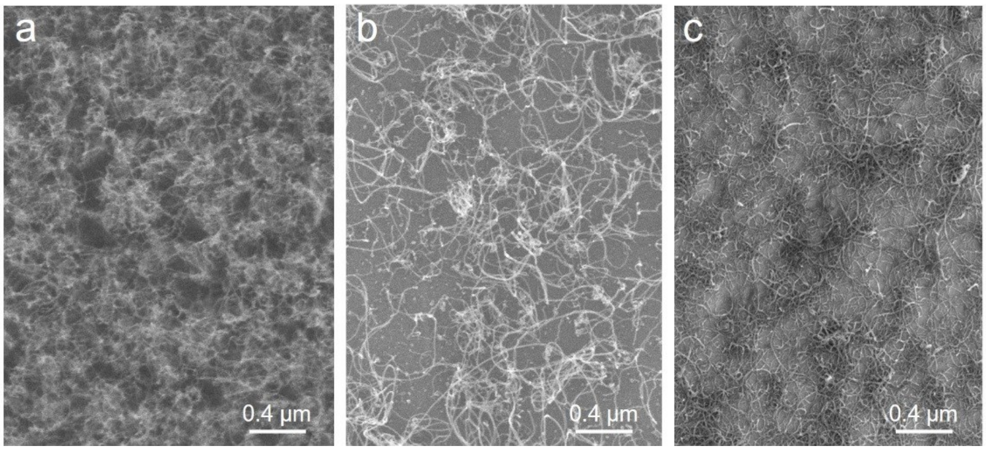

Figure 4.1 SEM images of three types of CNT based anodes. (a) VACNT, (b) RACNT, and (c) SSLbL (scale bar: 400 nm).

4.2. Materials and Methods

Bare gold electrode. The bare gold electrodes were deposited on a glass slide (micro slides, 4.6 × 2.6 × 0.1 cm^3, VWR) with six through holes pre-drilled mechanically (12 inch Bench Drill, Craftsman): one inlet, one outlet, and four for assembly. Afterwards, Cr/Au (20 nm/200 nm) films were deposited on the glass slides via sputtering on the glass slides (Emitech K675XD Turbo Sputter Coater). We chose a bare gold anode as control, following prior work that reported little difference exists on the attraction of *Geobacter* on carbon based material and gold [113].

VACNT and RACNT. The VACNTs were directly synthesized on a quartz slide ($5.08 \times 2.54 \times 0.1$ cm^3, Alfa Aesar) by catalytic chemical vapor deposition (CVD)[114]. After 5 nm-thick iron (Fe) catalysts were deposited on the quartz slide by electron-beam evaporation, the quartz slide was placed into a growth chamber. The temperature and pressure for CNT synthesis was 700 °C and 4 Torr, respectively. When the growth conditions were stabilized, the chamber was purged with nitrogen (N_2) gas of 10 sccm. The CNTs were then grown under acetylene (C_2H_2) ambience after ammonia (NH_3) pretreatment for 30 minute. The NH_3 pretreatment is necessary for the vertical alignment of CNTs[115]. In contrast to the synthesis of VACNTs, RACNTs were synthesized without NH_3 pretreatment. VACNT shows highly directional CNT growth due to strong van der Waals interaction between densely grown CNTs. NH_3 prevents Fe catalysts from being covered by amorphous carbon during synthesis, resulting in a high density of nucleation sites for CNTs growth. Without NH_3 pretreatment, curved and randomly oriented CNTs are synthesized and amorphous carbon is found between the CNTs.

SSLbL CNT. The SSLbL apparatus and experimental procedure for assembling polymer-CNT nano-composite films has been described previously[116]. Briefly, the

SSLbL apparatus allows the sequential spraying of polyelectrolyte solutions and the rinsing of water onto a horizontal rotating substrate using three vertically-oriented sprayers and a spin-coater. For SSLbL anode films, an aqueous solution of 1 % poly(styrene sulfonate) with 0.5 mg/mL multi-walled carbon nanotubes was prepared with three hours of bath sonication followed by 45 minutes of tip sonication and 1.5 hours of centrifugation at 3000 rpm to produce a stable dispersion. A solution of 10 mM poly(vinyl alcohol) at a pH of 2.8 was used as the polycation. Bare gold-coated glass slides were mounted onto the SSLbL vacuum chuck and rotated at 3000 rpm while solutions and rinse water were sprayed. A single bilayer was assembled using a spray/dry procedure of polycation, rinse, dry, polyanion, rinse, and dry. Deionized water matching the pH of the polycation solution was used for the rinse. Between bilayers, the substrate was dried at approximately 45 °C for 4 s. The multi-walled carbon nanotubes used in SSLbL CNT electrodes have a median diameter of 6.6 nm and an aspect ratio ~1000.

Inoculum. The inoculum for the micro-scale MFC was obtained from an acetate-fed microbial electrolysis cell (MEC), which had a *Geobacter*-enriched bacterial community originally from anaerobic-digestion sludge. The anolyte was composed of a 25-mM sodium acetate medium with 1,680 mg KH_2PO_4, 12,400 mg Na_2HPO_4, 1,600 mg NaCl, 380 mg NH_4Cl, 5 mg EDTA, 30 mg $MgSO_4 \cdot 7H_2O$, 5 mg $MnSO_4 \cdot H_2O$, 10 mg NaCl, 1 mg $Co(NO_3)_2$, 1 mg $CaCl_2$, 0.001 mg $ZnSO_4 \cdot 7H_2O$, 0.001 mg $ZnSO_4 \cdot 7H_2O$, 0.1 mg $CuSO_4 \cdot 5H_2O$, 0.1 mg $AlK(SO_4)_2$, 0.1 mg H_3BO_3, 0.1 mg $Na_2MoO_4 \cdot 2H_2O$, 0.1 mg Na_2SeO_3, 0.1 mg

$Na_2WO_4 \cdot 2H_2O$, 0.2 mg $NiCl_2 \cdot 6H_2O$, and 1 mg $FeSO_4 \cdot 7H_2O$ (per liter of deionized water) (pH 7.8 ± 0.2). For the start-up process, inoculum and anolyte were mixed at a volumetric ratio of 1:1. The catholyte was composed of 100-mM potassium ferricyanide in a 100-mM phosphate buffer solution. The anolyte and catholyte were supplied into the micro-scale MFC using a syringe pump.

Start-up and Data acquisition. Anolyte/catholyte solutions were pumped into the corresponding chambers at a flow rate of 0.25 µL/min. It typically takes 5-7 days to form a mature biofilm. Once the start-up process completes, the output current begins to reach steady state.

The current generated by the MFCs was recorded every minute by measuring voltage drop across an external resistor connected between the anode and the cathode using a data acquisition system (DAQ/68, National Instrument). During start-up, the MFCs were operated at 0.25 µL/min and the external resistor was set to 148-Ω. Once the start-up process completed, the flow rate was increased and polarization measurement was performed. For the polarization curve measurement, a series of resistors was employed, ranging from 148 Ω to 932 kΩ.

CE and energy conversion efficiency measurement. Coulombic efficiency and energy conversion efficiency were measured by stopping the anolyte supply while keeping the catholyte supply; the current over time domain was monitored while the catholyte kept flowing. Coulombic efficiency is the ratio of total coulombs transferred to the anode from the substrate to the maximum possible coulombs transferred if all substrate removal produced current. That is, $CE = C_P/C_T \times 100\%$, where C_P is the total coulombs calculated by integrating the current over the time for substrate consumption and C_T is the maximum possible coulombs of the substrate $C_T = V \times b \times A \times e \times (mol_{substrate})$. V is the volume of anode chamber (m^3), b is the number of moles of electrons produced by oxidation of substrate (b = 8 mol e^-/mol acetate), A is Avogadro's number (6.023×10^{23} molecules/mol), e is the electron charge (1.6×10^{-19} C/electron), and $mol_{substrate}$ is the moles of acetate oxidized.

Energy conversion efficiency is the ratio of total energy harvested by the MFC to the maximum possible energy that the biomass can produce (standard molar enthalpy of biomass): $\eta = E_P/E_T \times 100\%$, where E_P is the total energy calculated by integrating the power output over the time for substrate consumption and E_T is the maximum possible energy of the biomass $E_T = V \times c \times \Delta_f H°$. V is the volume of the anode chamber (m^3), c is the concentration of biomass in the anode chamber (c = 25 mol/m^3, sodium acetate), and $\Delta_f H°$ is the standard molar enthalpy of formation (708.8 KJ/mole for sodium acetate).

4.3. Results and Discussions

Biofilm morphology and thickness on three CNT-based anodes. Figure 4.1 shows the SEM images of the three CNT-based materials. Sheet resistance of the anodes was measured by a four-point probe method. The sheet resistance of VACNT, RACNT, SSLbL CNT, and bare gold electrodes were measured to be 1.48×10^3, 2.98×10^3, 3.84×10^0, and 3.68×10^0 ohm/square respectively. VACNT and RACNT electrodes have substantially higher sheet resistance than those of SSLbL CNT and bare gold electrodes.

Ex-situ characterization of morphology and thickness of biofilm on the CNT-based anodes were performed by scanning electron microscopy (SEM) as shown in Figure 4.2 (procedure of biofilm fixation is shown in supplementary materials). VACNT, RACNT, SSLbL CNT and bare gold anodes have biofilms thicknesses of approximately 3.3 μm, 6.5 μm, 9.0 μm and 1.8 μm respectively (Figure 4.2 (i)-(iv)). The bare gold anode, despite having very low sheet resistance, has a biofilm considerably thinner than others, suggesting CNTs attract more exoelectrogens.

16S rRNA analysis reveals that the *Geobacter* species dominate the biofilm, which is 40.8% of the total biofilm. The remainder of the biofilm is made up of unclassified bacterial species. The observed phylogenetic diversity likely reflects syntrophic interactions between exoelectrogens and nonexoelectrogens[117].

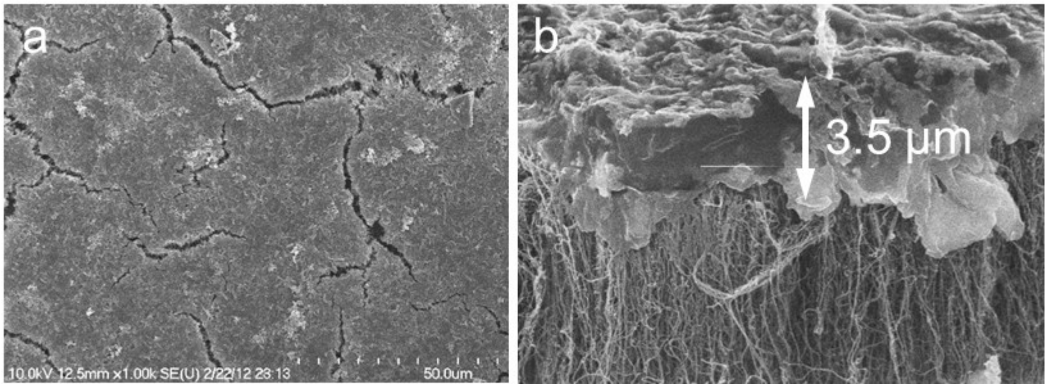

(i)

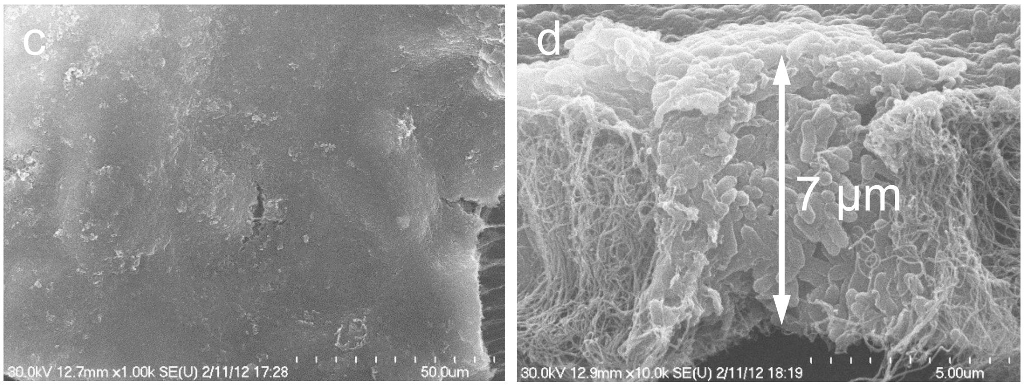
c
30.0kV 12.7mm x1.00k SE(U) 2/11/12 17:28
50.0um
d
7 µm
30.0kV 12.9mm x10.0k SE(U) 2/11/12 18:19
5.00um

(ii)

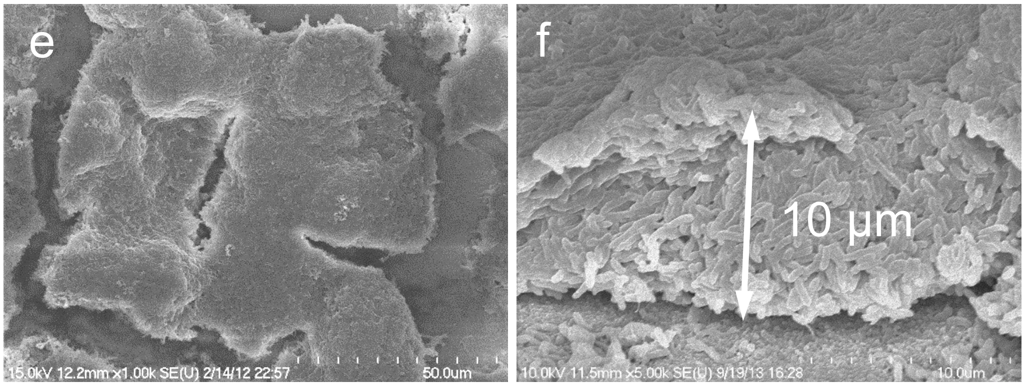
e
15.0kV 12.2mm x1.00k SE(U) 2/14/12 22:57
50.0um
f
10 µm
10.0kV 11.5mm x5.00k SE(U) 9/19/13 16:28
10.0um

(iii)

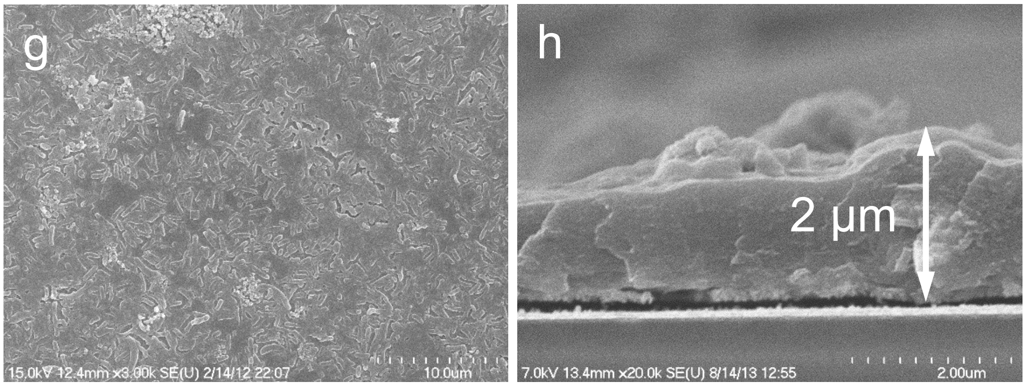
g
15.0kV 12.4mm x3.00k SE(U) 2/14/12 22:07
10.0um
h
2 µm
7.0kV 13.4mm x20.0k SE(U) 8/14/13 12:55
2.00um

(iv)

Figure 4.2. Top and cross-sectional view SEM images of (i) VACNT anode, (ii) RACNT anode, (iii) SSLbL CNT anode, and (iv) bare gold anode. The thickness of biofilm of these anodes are 3.3±0.2 μm, 6.5±0.5 μm, 9±1 μm and 1.8±0.2 μm thick, respectively (the figures show the thickest part), suggesting CNT-based anodes attract more exoelectrogen than the gold anode to form thick biofilm. (ii) shows the exoelectrogen and RACNT weaves together well, suggesting high biocompatibility of RACNT.

The biofilm morphology and thickness characterization suggests that CNT-based materials attract more exoelectrogens to form thicker biofilms than does bare gold. Prior art reports that cell growth is significantly accelerated on a nanostructured material-TiO_2 nanotube [118]. Although the promotion mechanisms of the nanostructured material on cell proliferation are still not fully understood[119], it is plausible that the thicker biofilm generation may be due to the nanostructured CNTs, which provide a larger surface area for *Geobacter sp*: cell adhesion. The thicker biofilm on the CNT-based anodes also implies the biocompatibility of the CNT-based materials with *Geobacter sp*. The previous study by Ren *et al.* 2011 reported a discrepancy between the microbial and electrochemical responses on the anode, yet our results suggest an indirect link between the thickness of the biofilm and current and power generation capability[120].

Of the three CNT anodes, the SSLbL CNT has a lowest sheet resistance of 3.84×10^0 ohm/square, which is significantly lower than those of VACNT and RACNT, $\sim10^3$ ohm/square, and the thickest (9.0 μm) biofilm, suggesting the sheet resistance of the anode impacts the biofilm thickness. Xie *et al.* has shown that a graphene sponge sandwiched by a stainless-steel current collector produces significantly higher current than a bare graphene sponge anode. Here the stainless-steel electrode has a lower resistance than the graphene sponge, providing a “highway” for electrons [98]. This work suggests that the high electrode resistance (graphene sponge itself, ~180 Ω) limits the current production from *Shewanella* MR1. The sheet resistance of the VACNT and RACNT anodes are 1.48×10^{3}, and 2.98×10^{3} ohm/square respectively, which are on the same order of internal resistance of MFCs having them as anodes, 4.3 kΩ and 2.3 kΩ respectively. The high sheet resistance of VACNT and RACNT electrodes likely limits the current from exoelectrogens. The SSLbL CNT anode possesses relatively high surface area and low sheet resistance, which result in the thickest biofilm. The measured data, however, does not provide conclusive evidence as to which aspect of features impact biofilm formation most extremely.

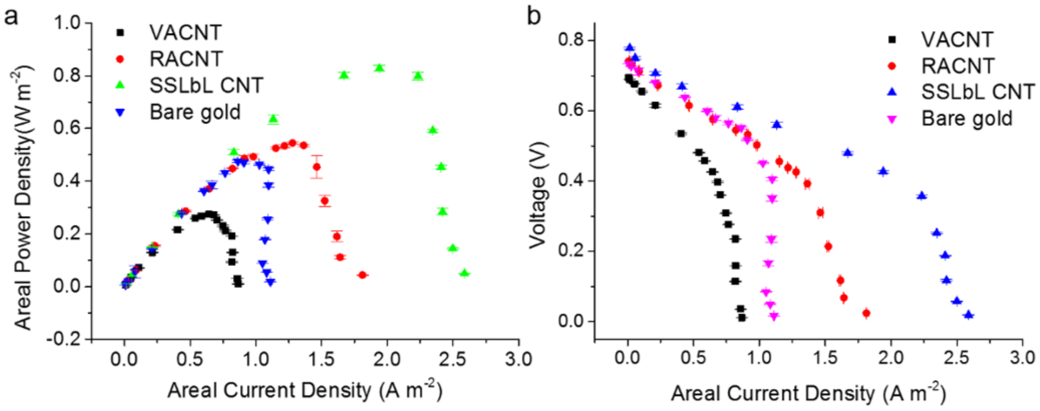

Figure 4.3. Polarization curves of miniaturized MFCs with CNT-based and gold anodes. (a) Power density versus current density and (b) voltage versus current density. The measured current is assumed to be solely from oxidizing acetate in the anolyte[37, 121, 122].

Current/power density and efficiency of miniaturized MFCs. The current/power density of miniaturized MFCs that have CNT-based anodes was characterized via polarization curves (Figure 4.3). The flow rate of anolyte/catholyte was set to be 2 µL/min. All MFCs show 0.7-0.8 V open circuit voltage, suggesting oxygen intrusion is successfully mitigated. The maximum current and power densities of 2.59 A m^{-2} and 0.83 W m^{-2}, respectively, were obtained from the SSLbL CNT MFC, in accordance with the biofilm thickness measurements (Figure 4.2). Maximum volumetric power density of 3320 W m^{-3} was obtained by the SSLbL CNT MFC, which is the highest among all MFCs.

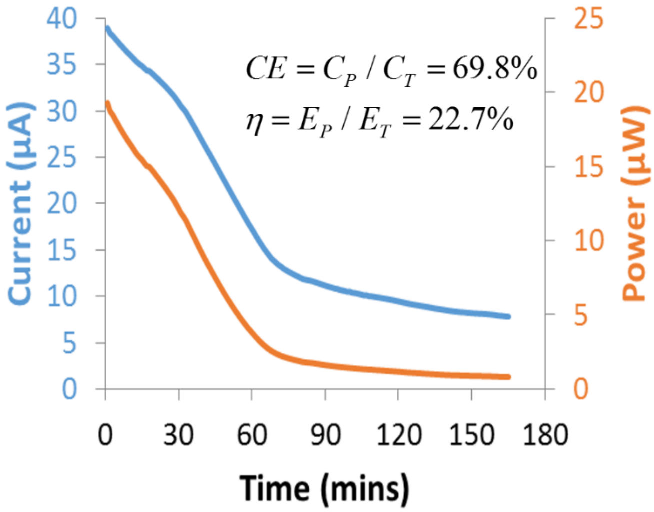

Figure 4.4. Current and power versus run time in the MFC with SSLbL CNT anode for Coulombic efficiency (CE) and energy conversion efficiency measurement. The calculated CE and energy conversion efficiency are 69.8 % and 22.7 %, respectively.

Figure 4.4 shows the transient current profile to measure CE and energy conversion efficiency of the SSLbL CNT MFC. The anolyte flow was stopped, while keeping the catholyte running to measure harvested charges from the anolyte in the anode chamber[43] A high CE of 69.8% and an energy conversion efficiency of 22.7% were achieved (calculation of CE and EE from Figure 4 is shown in supplementary materials). CEs of 61.3%, 73%, 80.9% were also achieved for the VACNT, RACNT, and bare gold anodes, respectively.

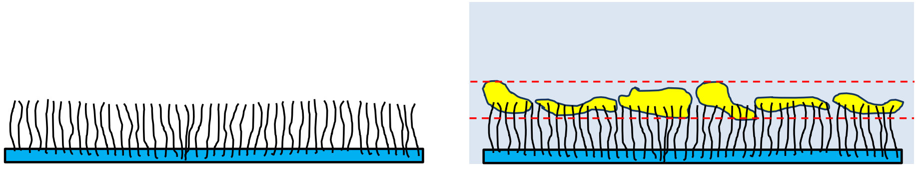

(a) VACNT anode

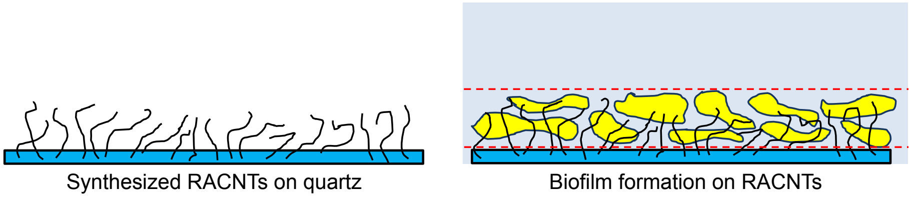

(b) RACNT anode

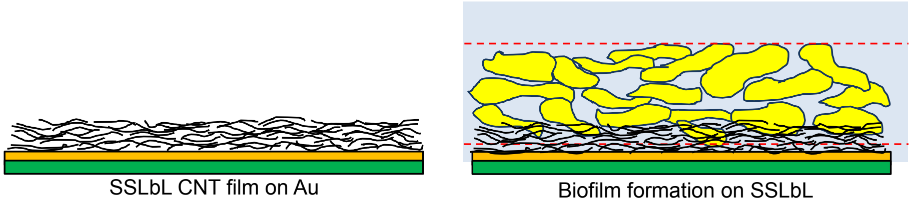

(c) SSLbL anode

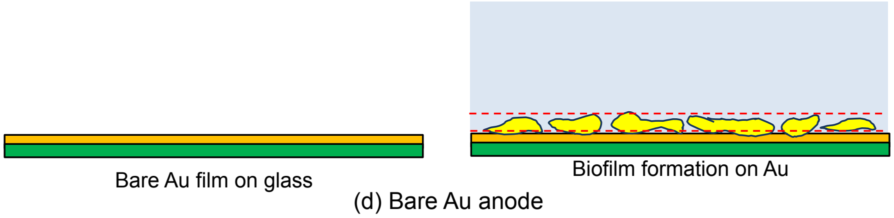

(d) Bare Au anode

Figure 4.5. Schematic illustration of three types of CNT-based anodes. (a) VACNT (Vertically Aligned Carbon Nanotubes), (b) RACNT (Randomly Aligned Carbon Nanotubes), (c) SSLbL (Spin-Spray Layer-by-Layer Carbon Nanotubes) and (d) Bare gold anode. Geobacter sp. form their biofilm on those anodes and the thickness of the biofilm is a function of types of anodes.

Correlation between biofilm and current/power density. A schematic illustration of the biofilm formation on three types of CNT-based and bare gold anodes is shown in Figure 4.5. The high density and vertical structure of VACNT stops exoelectrogens from placing themselves inside the VACNT forest, which results in a thin biofilm and low current/power density. In contrast, RACNT film offers rather porous features and thus can accommodate exoelectrogens between CNTs, resulting in a thick biofilm. The SSLbL CNT film is comprised of horizontally oriented CNTs conjugated with polymers. A stratified-rod-network model of the electrical conductance of these SSLBL films can be found in a previous study[123]. Here we show that this structure results in the thickest exoelectrogen biofilm while the bare gold control anode has the thinnest biofilm.

The schematic illustration matches well with experimental result. The VACNT and RACNT electrodes show similar sheet resistances, while the RACNT anode forms a thicker biofilm and generate a higher current/power density than the VACNT films. The RACNT film may allow exoelectrogens to penetrate between the individual CNTs whereas exoelectrogens cannot penetrate inside the dense VACNT forest (Figure 2(i), (ii)). Exoelectrogens, similar to cells, generate mechanical force for adhesion on electrodes[124]. The dense VACNT forest may resist the bending of CNTs and thus exoelectrogens cannot penetrate. Prior studies by Ren *et al.* 2011 and Lyon *et al.* 2010 report the external loads impact not only current/power density but also the biofilm architecture and bacterial communities. Higher external resistance (5-10 kΩ) results in a lower current/power density as well as a lower cell count [125, 126]. Our finding aligns well with these prior arts with regards to parameters that impact the biofilm structure, including materials and sheet resistance of anode.

The electron generation rate of the SSLbL CNT biofilm is estimated to be 4.22×10^5 electrons/second. This calculation is similar to that of *Shewanella MR1*, which can generate 10^6 electrons/second[127]. This calculation supports the postulation that the electron generation rate and exoelectrogen population have a major impact on the performance of MFCs. Porous electrodes were reported to enhance the mass transfer of acetate and H^+ carrying buffer, which aid the electron generation capability of *Geobacter sp.* deep inside the biofilm[103, 104]. Therefore, anode materials having high surface-area-to-volume ratio, high porosity, and high biocompatibility help to reduce areal resistivity, consequently improving current and power density.

Table 4.1: Measured specifications of 4 different anodes in miniaturized MFCs

	Sheet resistance [ohm/square]	Areal resistivity [kΩ·cm^2]	Biofilm thickness [μm]	Current density [A m^{-2}]	Power density [W m^{-2}]
VACNT	1.48×10^3	4.3	3.3	0.87	0.27
RACNT	2.98×10^3	2.3	6.5	1.81	0.54
SSLbL CNT	3.84×10^0	1.2	9.0	2.59	0.83
Bare gold	3.68×10^0	2.2	1.8	1.11	0.48

Discussion on the impact of the resistivity of the anode. Energy loss in micro-scale MFCs involves two parts, ohmic loss and overpotential. The ohmic loss can be measured using the slope of the ohmic region in polarization curves, while the total overpotential is comprised of overpotentials at the anode, cathode, and overpotential induced by the existence of a pH discrepancy between the anode and cathode chambers, etc[7, 56, 128, 129, 130, 131].

The areal resistivity may be used to obtain the ohmic loss. According to chapter 2, areal resistivity can be expressed as:

$$r_i = r_a + r_c + r_m + r_e \tag{4.1}$$

where r_i is the total areal resistivity and r_a, r_c, r_m, r_e are areal resistivity of anode, cathode, ion exchange membrane, and electrolyte, respectively. r_a is comprised of the resistance of the anode itself and electron generation/transfer from exoelectrogens to the anode. r_c involves the resistance of the cathode itself, potassium ferricyanide ion transfer from the bulk solution to the vicinity of the cathode and reduction of the ions at the cathode. r_m is mainly determined by the resistivity of the ion exchange membrane for movement of counter ions across the membrane. r_e is a function of the distance between the two electrodes and the conductivity of the acetate medium:

$$r_e = \frac{l}{K} \tag{4.2}$$

where l is the distance between the two electrodes, and K is the specific conductivity of the electrolyte.

The distance between anode and cathode (l) is the sum of the thicknesses of the two gaskets, 500 μm total, and ion exchange membrane, 178 μm, for a total distance of 678 μm. The specific conductivity of the anolyte and catholyte were measured as 5.7 mS/cm and 2.5 mS/cm, respectively. Based on these measured and given parameters, r_e is equal to 14.4 $\Omega\cdot\text{cm}^2$. r_m, the resistivity of the ion exchange membrane (Nafion 117), was measured to be 10 $\Omega \cdot cm^2$, in phosphate buffer medium. r_c, the resistivity of the cathode, is also low, in the magnitude of 10 $\Omega \cdot cm^2$. Consequently, r_a, the anode resistivity, is responsible for the majority of total areal resistivity.

Of r_a, the areal resistivity of the anode, the resistivity of the anode material itself is negligible for the SSLbL CNT and bare gold, and therefore the majority of the areal resistivity is attributed to the resistance of electron generation by exoelectrogen metabolism and transfer from exoelectrogens to anode. On the other hand, the VACNT and RACNT anodes have high sheet resistance, which significantly adds to the anode resistivity. This limits current/power density. Figure 4.3 shows that all MFCs suffer from concentration loss at high current density. This concentration loss is believed to be associated with the limited extracellular electron transfer (EET) at high current density[132] and a mass transfer limitation of the transfer of acetate and H^+ carrying buffer from bulk to biofilm. It is also helpful to compare the performance of miniaturized MFCs with different anodes to provide helpful information for future performance improvement. Because exoelectrogens are the catalysts for current/power generation in MFCs, biofilm morphology/thickness has a significant impact on the current/power generation. On the other hand, anode sheet resistance also impacts current/power generation. High sheet resistance increases the overall internal resistance of MFCs, which in turn limits the current/power generation. Based on biofilm thickness characterization of four types of anodes, the SSLbL CNT anode has the thickest biofilm, at 9.0 μm, as well as the highest current/power generation capability, shown to be 2.59 A m^{-2} and 0.83 W m^{-2} respectively. The RACNT has the second thickest biofilm, 6.5 μm, and delivers the second highest current/power generation capability, 1.81 A m^{-2} and 0.54 W m^{-2}. VACNT anode has the third thickest biofilm, 3.3 μm, which is thicker than bare gold control at 1.8 μm, yet had the lowest current/power generation capability, 0.87 A m^{-2} and 0.27 W m^{-2}, lower than the bare gold control at 1.11 A m^{-2} and 0.49 W m^{-2}. This result implies that the high sheet resistance of VACNT anode degrades current/power generation capability. The measured specifications are summarized in Table 4.1.

Comparison with prior studies. Table 4.2 summarizes measured specifications of the SSLbL CNT in comparison with previously reported miniaturized MFCs. Areal and volumetric power densities and the CE of this work are substantially higher than those of prior studies; correspondingly, areal resistivity of this work is much lower than that of prior studies. Miniaturized MFCs using CNT anodes exist, yet their areal and volumetric power density are very low[42, 108]. The improvements suggest successful biocompatibility of the CNT materials in this work.

Table 4.2: A comparison of specifications of this work compared with prior art.

Performance parameters	Mink et al. [108]	Inoue et al. [42]	Choi et al. [43]	Qian et al. [39]	Siu et al. [25]	Biffinger et al. [133]	This work (SSLbL CNT)
Anode material	CNT	CNT	Gold	Gold	Gold	Carbon/Pt ink	CNT+polymer

Anode volume [μL]	1.5	40	4.5	1.5	15	25**	**12.5**
Anode area [cm^2]	0.25	0.24	2.25	0.15	1.2	0.45	**0.5**
Areal resistivity [kΩ·cm^2]	N/A	N/A	22.5	4.5	30	3.375	**1.2**
P_{areal} [W m^{-2}]	0.0196	0.0738	0.047	0.015	0.004	0.06	**0.83**
$P_{volumetric}$ [W m^{-3}]	392	343	2333	15.3	4.24*	10	**3320**
CE [%]	N/A	N/A	31	2.8	14.7	NA	**60%-80%**

**Calculated based on the reported data.*

***The volume of the device.*

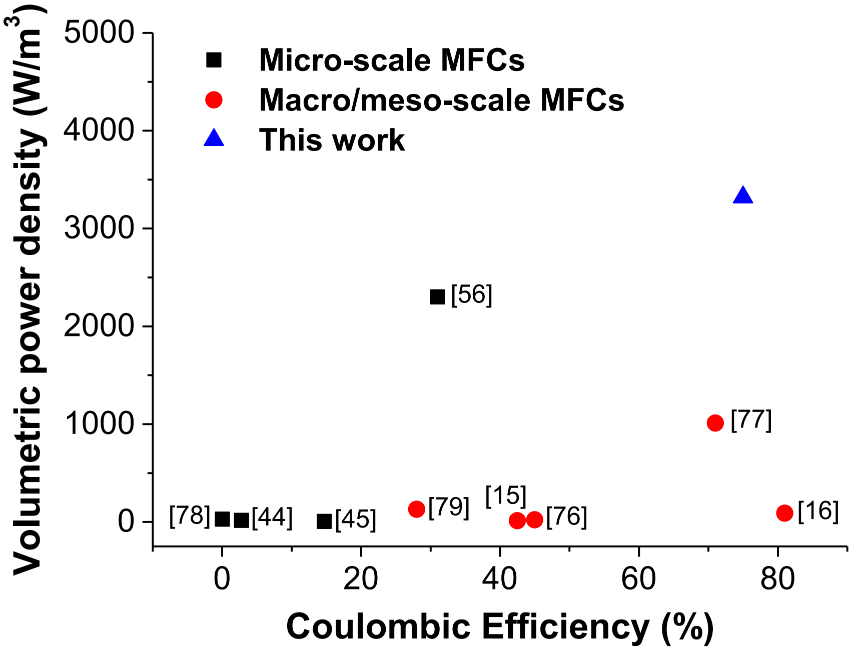

Figure 4.6. A comparison of volumetric power density and CE of SSLbL CNT with existing macro-/meso- and micro-scale MFCs[25, 31, 38, 39, 43, 81, 92, 134, 135]. The volumetric power density of this work is higher than all previous MFCs, regardless of scale, and the CE of this work are substantially higher than those of most micro-scale MFCs and are comparable with those of macro-/meso-scale MFCs.

Figure 4.6 shows the areal power density, volumetric power density and CE of the SSLbL CNT compared to prior studies - including macro/meso-scale and micro-scale MFCs. The volumetric power density of the SSLbL CNT MFC is 3320 W m^{-3}. Both the areal power density and CE of this work are also substantially higher than those of most micro-scale MFCs and are comparable with those of macro-/meso-scale MFCs. Most micro-scale MFCs deploying *Geobacter* reported previously used PDMS as their gaskets, which has substantial oxygen permeability. This results in severe oxygen intrusion into the anode chamber, leading to a very low CE. Our work implemented a silicone gasket, which has an oxygen permeability (19685 $cm^3 \cdot mm/m^2 \cdot day \cdot atm$), 2.7 times lower than that of PDMS (52531 $cm^3 \cdot mm/m^2 \cdot day \cdot atm$), which yields a higher CE.

The areal/volumetric power density of 0.83 W m^{-2} and 3320 W m^{-3}, respectively, are comparable or higher than those of other types of renewable energy conversion techniques, such as thermoelectric[136], piezoelectric[137], and indoor photovoltaics[138], suggesting that the miniaturized MFC may be an attractive candidate for renewable energy conversion approaches. Approximately 50-80 μW can be generated from the miniaturized MFCs at a voltage of 0.4-0.5 V, which may fit well to sub-100 μW applications such as ultra-low power MCUs (microcontroller units), data storage, passive RFID tags, transmitters for wireless sensor network, implantable medical devices, *etc*[138, 139, 140, 141]. Furthermore, the miniaturized MFCs can be integrated into low-power electronics for autonomous operation in rural and environmentally unfriendly places where stand-alone maintenance and free operation are demanded[32, 133].

CHAPTER 5

IMPROVING THE CURRENT AND POWER DENSITIES OF MINIATURIZED MICROBIAL FUEL CELLS WITH THREE-DIMENSIONAL GRAPHENE SCAFFOLD ANODE[142]

5.1. Introduction

There is a surplus of harvestable, green, renewable energy stored in biomass which has the potential to offset concerns of global warming and energy depletion. Biomass in wastewater contains approximately 1.5×10^{11} kWh of potential energy, equivalent to 1.7×10^{10} W. Agricultural practices could produce 1.34×10^{12} Kg of biomass, equivalent to a power of 6×10^{11} W, which is equivalent to 120% of the United States' annual electricity generation[85, 143, 144, 145]. Many pursuits are being made to capture this major source of green renewable energy.

A MFC is an electrochemical fuel cell that directly converts the chemical energy of organic compounds from biomass to electrical energy. This is accomplished via catalytic reactions of microbes - named exoelectrogens or anode respiring bacteria[86]. MFCs are particularly attractive when compared to traditional biomass utility technologies such as incineration and gasification, primarily due to the direct electricity conversion which enables high efficiency. Many different microbe communities have been discovered to reduce various organic substances such as wastewater, marine sediment, nuclear waste, and even inorganic waste[91]. The catalytic living microbes in MFCs regenerate themselves, which allows for higher efficiency when compared to enzymatic fuel cells which require the continuous supply of an external catalyst[91].

The catalytic activity of the anode is often one of severe bottlenecks of current/power generation, and therefore has critical influence on the viability of MFCs with an efficient electron acceptor. Consequently, the anode performance limits the power density. To date, the highest power reported for an MFC is 3320 W/m^3, which is at least several folds to two orders of magnitudes lower than conventional power sources/converters such as lithium ion batteries and hydrogen fuel cells[146]. In order to enhance the catalytic activity of the anode and improve the performance of MFCs, studies on reducing the electrode resistance, improving the mass transfer of organic compounds and H$^+$ carrying buffers, implementing materials with properties of high surface area to volume ratios and high electrical conductivities, and improving the configuration of MFCs, have been actively sought[56].

Miniaturized power sources/converters have become an active area of research, focusing specifically on devices such as piezoelectric nanogenerators[147], ultra-fast charge-discharge batteries[148], and ultrahigh-power micrometer-sized supercapacitors[149]. These devices all benefit from a small footprint, a high surface area to volume ratio, and short a charging time. Miniaturized MFCs have been reported[42, 43, 56, 108, 150, 151] which demonstrate an areal power density comparable to that of their macro/meso-scale counterparts and with substantial improvements to volumetric power density[151].

While many different materials have been adopted as anodes, carbon based materials such as carbon cloth, carbon mesh, carbon paper, graphite fiber brush, graphite foam, graphite granules, and graphite plates and sheets have been adopted due to their ease of access, decent conductivity, and stability[32, 81, 91, 92, 93, 94]. More recently, nanostructured carbon based materials have become widely used for the anode due to their further magnified low cost, good electrical conductivity, high surface area to volume ratio, and mechanical and thermal stability. These carbon based nanostructured anodes were implemented to be planar or 3D configurations. Planar electrodes incorporate carbon-based nanostructured materials, such as CNT and graphene on top of a planar surface where the exoelectrogens form a biofilm[101, 150]. Such constructs have shown areal / volumetric power densities of 0.83 W/m^2 and 3320 W/m^3 based on the projected anode area and anode chamber volume. 3D electrodes are attractive to allow for the growth of a thick exoelectrogen biofilm; this is especially true when 3D electrodes are porous and have dimensions of tens of micrometers to a few fold larger. According to prior studies on the electron transfer of biofilms, the exoelectrogens located tens of micrometers away from the anode have difficulty transferring electrons to the anode due to EET limitation[132, 152, 153, 154]. A variety of 3D nanostructured carbon based electrodes have been adopted in MFCs, such as CNT textile based anodes[155], graphene sponge[156], chitosan/vacuum-stripped graphene scaffold[104], reduced graphene oxide/CNT coated scaffold[107], polyaniline hybridized graphene[103], graphene modified carbon fiber[99], electronspun nanofiber[157], reduced graphene oxide on carbon fiber[99], CNT/polyaniline or

CNT/chitosan composite[50, 100], multi-walled CNT[42, 52], 3D graphene on Ni foam[105, 106], to capitalize on this increased biofilm formation. Such constructs feature a high effective surface area and conductivity and deliver maximum areal / volumetric power densities of 1.57 W/m^2 and 394 W/m^3 respectively.

In this chapter, we have analyzed the effects of 3D carbon nanostructured anodes on the current and power densities of MFCs. We present miniaturized MFCs having 2D and 3D graphene anodes including a 2D mercapto reduced graphene oxide (mRGO) anode on a current collector (CC, which is a gold or platinum thin film with low sheet resistance), a 2D laser scribed graphene (LSG) anode on CC, a 3D graphene scaffold on CC, and a 2D bare CC as a control. This comparative study illuminates many ways for future improvements to power density for MFCs using 3D anodes.

5.2. Materials and Methods

Innoculum. The inoculum for the miniaturized MFC was obtained from an acetate-fed MEC that had been continuously operated for more than 6 months and had a *Geobacter*-enriched bacterial community originally from anaerobic-digestion sludge. The anolyte was comprised of a 25 mM sodium acetate medium with 1,680mg KH_2PO_4, 12,400mg Na_2HPO_4, 1,600mg NaCl, 380mg NH_4Cl, 5mg EDTA, 30mg $MgSO_4 \cdot 7H_2O$, 5mg $MnSO_4 \cdot H_2O$, 10mg NaCl, 1mg $Co(NO_3)_2$, 1mg $CaCl_2$, 0.001mg $ZnSO_4 \cdot 7H_2O$, 0.001mg $ZnSO_4 \cdot 7H_2O$, 0.1mg $CuSO_4 \cdot 5H_2O$, 0.1mg $AlK(SO_4)_2$, 0.1mg H_3BO_3, 0.1mg $Na_2MoO_4 \cdot 2H_2O$, 0.1mg Na_2SeO_3, 0.1mg $Na_2WO_4 \cdot 2H_2O$, 0.2mg $NiCl_2 \cdot 6H_2O$, and 1mg $FeSO_4 \cdot 7H_2O$ (per liter of deionized water). The inoculum and anolyte were mixed at a volumetric ratio of 1:1 for the start-up process. The catholyte was composed of 50-mM potassium ferricyanide in a 100-mM phosphate buffer solution. The anolyte and catholyte were fed into the miniaturized MFC using a syringe pump (Harvard Instrument Inc.). Prior to the introduction of the anolyte and catholyte to the MFCs, both anolyte and catholyte were purged with nitrogen for 30 minutes. The MFCs operated at 40 ± 3°C.

Data acquisition. The current generated by the MFCs was recorded every minute by measuring the voltage drop across an external resistor connected between the anode and the cathode using a data acquisition system (DAQ/68, National Instrument) using Labview Interface. During start-up, the MFCs were operated at 0.25 μL/minute and the external resistor was set to 148 Ω. Once the start-up process completed, the flow rate was increased until the maximum current and power densities were obtained and polarization measurement was performed. For the polarization curve measurement, a series of resistors were employed, ranging from 148 Ω to 1 MΩ and open circuit.

Calculation and Analysis. The current through the resistor was calculated via Ohm's law ($I = V/R$), where V is the voltage measured across resistor. MFC output power was calculated via Joule's law ($P = I^2R$). Areal and volumetric current/power density were calculated by $I_{areal} = I/A, P_{areal} = P/A$ and $I_{volumetric} = P/V, P_{volumetric} = P/V,$ where A and V were the projected anode area and anode volume. Polarization curves were plotted according to the voltage output and current and power densities. Internal resistance (R_i) is obtained by linearly fitting the ohmic region of the polarization curve. Areal resistivity is obtained by $r_i=R_i \cdot A$.

SEM Imaging. The MFCs were disassembled and rinsed by phosphate buffer saline (PBS). Adherent exoelectrogen on the anodes were fixed in a 2% glutaraldehyde solution for 24 hours at 4 °C (Glutaraldehyde solution, Grade I, 25% in H_2O, Sigma Aldrich). Samples were then dehydrated by serial 10 minute transfers through 50, 70, 90, and 100% ethanol. A layer of gold with a thickness of ~10 nm was deposited onto the sample to increase conductivity. Biofilm on anodes was then examined using a Field Emission Scanning Electron Microscopy (FESEM) (Hitachi S-4700-II). The anodes before biofilm growth were imaged using an environmental SEM (XL30 ESEM-FEG).

Fabrication of the 2D single layer graphene. A 2D single layer graphene was manufactured by chemical vapor deposition (CVD) on copper foil (25 μm, Alfa Inc.) at 1000 °C. CH_4 and H_2 are utilized for CVD. After CVD, the 2D single layer graphene on copper foil was first spin-coat on polymethyl methacrylate (PMMA). Afterwards, the copper was removed by copper etchant, and it was later cleaned by de-ion water by two times, 30 hour each time and afterwards it was dried for one day.

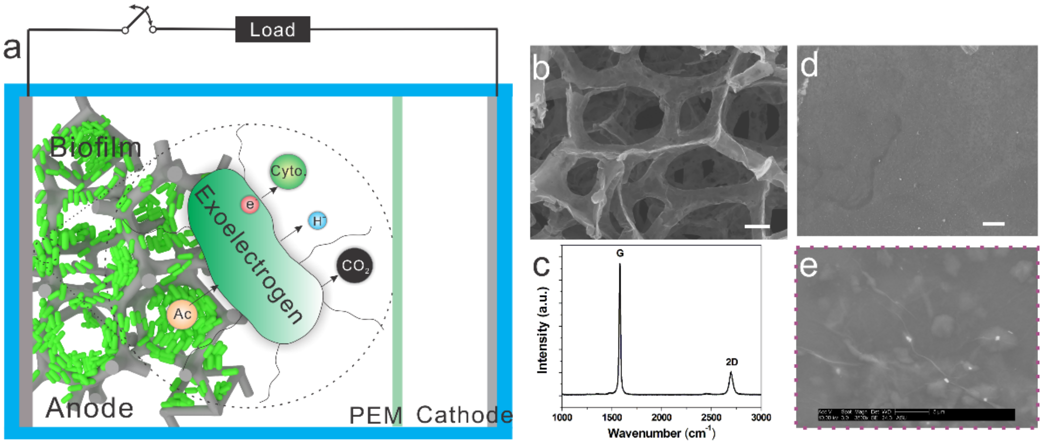

Figure 5.1. Schematic of the miniaturized MFC and characterization of different anode materials implemented in the miniaturized MFC. (a) Schematic of the miniaturized MFC having 3D graphene macroporous scaffold anode. The high specific area and macroporosity of the 3D anode allows the growth of larger quantity of biofilm; (b) SEM image of the 3D graphene macroporous scaffold; the 3D free-standing graphene scaffold was fabricated by chemical vapor deposition (CVD) on a nickel template, which was subsequently etched to form a free-standing 3D macroporous graphene scaffold; (c) typical Raman spectra of 3D scaffold; (d) SEM image of the single layer graphene (scale bar: 50µm; (e) is the zoomed-in view of (d)).

Fabrication of 3D graphene macroporous scaffold. 3D graphene macroporous scaffold was prepared by following fabrication procedures which has been described previously[158]. Briefly, nickel were used as 3D scaffold templates. Graphene was grown by CVD at 1000 °C. Afterwards, a thin PMMA layer was used as a support to reinforce the graphene scaffold structure for subsequent Nickel foam removal. The Ni foams covered with graphene were drop-coated with a PMMA solution, and then baked at 180 °C for 30 min. Then the samples were put into HCl (3 M) solution at 80°C for 3 h to completely dissolve the nickel. Finally free-standing graphene scaffold was obtained by dissolving the

PMMA with hot acetone at 55°C. The Raman spectrum of the 3D graphene scaffold is shown in Fig. 1(c), there are two sharp peaks, 2D-band peak at ~2697 cm^{-1} and G-band peak at ~1581 cm^{-1}. The 2D to G ratio is 0.18, indicating that it is few-layer graphene.

5.3 Results and Discussions

Miniaturized MFCs with 2D and 3D graphene based anodes. Fig. 5.1(a) shows a schematic of a miniaturized MFC having 1 cm^2 graphene-based anode variants, including 2D single layer graphene and a 3D graphene scaffold. The SEM images of corresponding anodes are illustrated in Fig. 5.1(b, d). 3D graphene scaffolds are spaced by approximately 100-200 μm. This spacing provides efficient mass transfer to facilitate EET. Fig. 5.1(c) shows the typical Raman spectra of 3D graphene scaffold. There are two sharp peaks, a 2D-band peak at ~2697 cm^{-1} and a G-band peak at ~1581 cm^{-1}. The 2D to G ratio is 0.18, indicating that it is few-layer graphene, which is in agreement with previous reported Raman of 3D graphene scaffold[158].

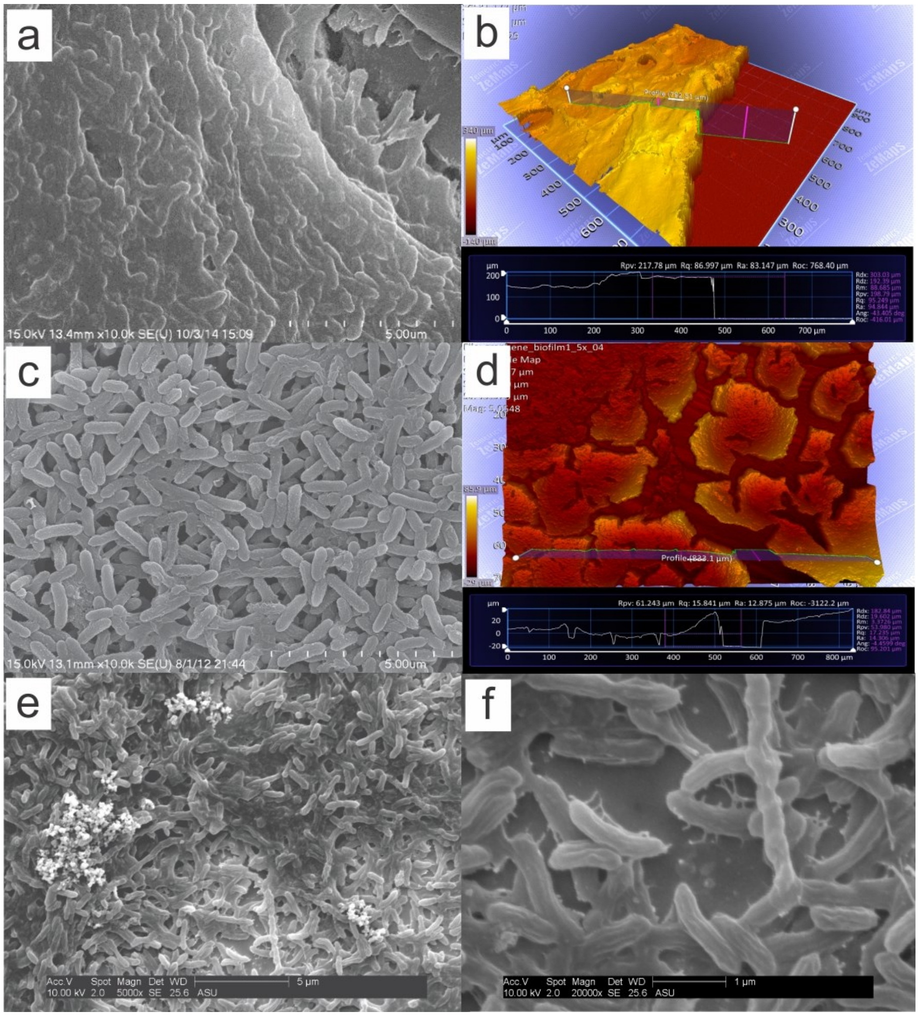

Figure 5.2. Morphology of biofilm on anodes imaged by SEM and optical profilometer. (a, b) 3D graphene macroporous scaffold; (c, d) 2D single layer graphene; (e, f) control - bare gold current collector; the biofilm formation on the 3D scaffolds showed a thick and dense biofilm, ~ 150-200 μm thick and 1.6×10^{11} Geobacter sulfurreducens / cm^2, on the 3D scaffolds (a, b), matching well with the highest current and power density results found in this study. The biofilm thickness is a total of 5-6 stacks of graphene scaffolds. The biofilm on the 2D single layer graphene (c, d) had a ~ 20-40 μm thick biofilm, which delivered the highest current and power density recorded among planar 2D anodes. The biofilm on the control was approximately 2-3 μm (e, f), only several layers of exoelectrogen were present.

Biofilm Formation on 2D and 3D Graphene Anodes. The MFCs with variant anodes were all successfully started up in 7-14 days. Biofilms on 2D and 3D graphene anodes were visualized to characterize the morphology of their respective biofilms. The SEM and optical profilometer images after biofilm growth, as shown in Fig. 5.2(a, b), demonstrate thick and dense biofilm formation. This thickness of 150-200 μm and density of 1.6×10^{11} *Geobacter sulfurreducens* / cm^2, formed on the 3D graphene scaffold generated the highest current and power density reported. The biofilm thickness is comprised of 5-6 stacks of graphene scaffolds. The single layer graphene (Fig. 5.2(c, d)) yielded a thick biofilm of ~ 20-40 μm - equivalent to a density of 2.8×10^{10} *Geobacter sulfurreducens* / cm^2 - which is consistent with the highest current and power density recorded among planar 2D anodes. The biofilm on the control was thin, at ~ 2-3 μm, 2.3×10^{9} *Geobacter sulfurreducens* / cm^2 (Fig. 5.2(e, f)), only a few layers of exoelectrogen were present yielding correspondingly low current and power densities.

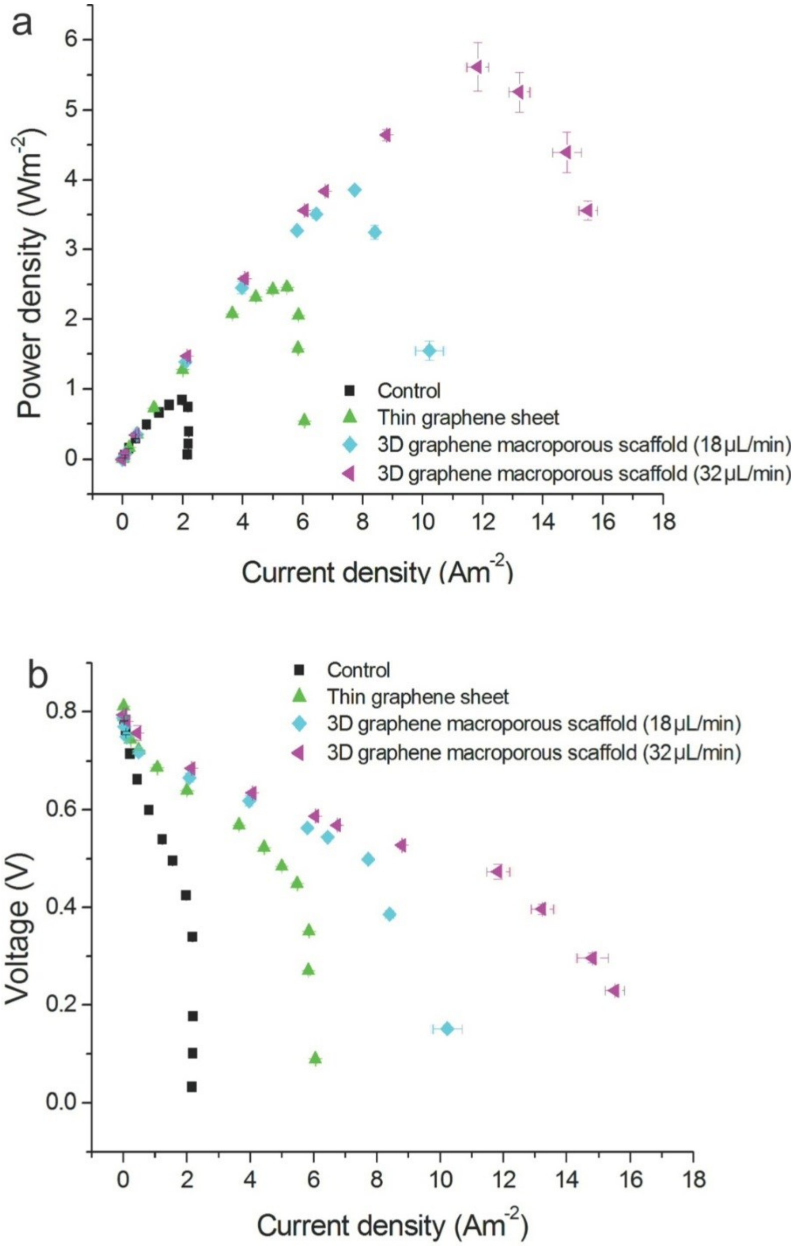

Figure 5.3. Polarization curves of the MFCs with different anodes: control, 2D single layer graphene, and 3D graphene macroporous scaffold. all data are collected at 18µL/min, unless specified. The 3D scaffold demonstrated substantially higher current and power density of 15.51 ± 0.30 Am^{-2} and 5.61 ± 0.35 Wm^{-2} at a flow rate of 32 µL/min.

Current and Power Density of Miniaturized MFCs. Fig. 5.3 shows the polarization curves of miniaturized MFCs with variant electrodes. The control showed a low sheet resistance of 3.65 Ω/square, and delivered a maximum current density of 2.20 Am^{-2} / 8800 Am^{-3} with a power density of 0.84 Wm^{-2} / 3360 Wm^{-3}. The 2D single layer graphene was fabricated by chemical vapor deposition (CVD) and showed sheet resistance of 4.13 Ω/square, current density of 6.06 Am^{-2} / 24240 Am^{-3} and power density of 2.46 Wm^{-2}/ 8840 Wm^{-3}, a 1.75 and 1.96 fold improvement respectively over those of the control. The high performance of the 2D single layer graphene is believed to be due to excellent conductivity, biocompatibility, and electrochemical characteristics of the 2D graphene[159] which results in a thicker and denser biofilm formation as illustrated by the SEM and optical profilometry results.

The 3D graphene scaffold was fabricated by CVD on a nickel foam template, which was subsequently etched to form a free-standing 3D macroporous graphene scaffold. The fabrication process of the graphene based electrodes are detailed in appendix C. This fabrication strategy is a low-cost approach to construct 3D graphene with a high surface area to volume ratio[158]. The 3D graphene macroporous scaffold was spaced by approximately 100-200 μm and showed very low sheet resistance at 0.335 Ω/square. The 3D graphene macroporous scaffold addresses two of the stubborn bottlenecks comprised of the reduction of electron transfer efficiency of microbes located far from the anode, and insufficient buffer supply to the bacterial biofilm which have impeded MFCs in their ability to achieve high power density. The 3D scaffold provides high specific surface area, high porosity, excellent conductivity, and biocompatibility. All of these features offer a spacious and optimized environment for the exoelectrogen to form a thick and dense biofilm. Specifically, the excellent conductivity mitigates the ineffective electron transfer of microbes far from the anode, and the high porosity mitigates the insufficient buffer supply to the bacterial biofilm. This biofilm demonstrated substantial current and power density improvements over its 2D counterparts. Maximum current and power densities of 10.23 Am^{-2} / 20460 Am^{-3} and 3.86 Wm^{-2} / 7720 Wm^{-3} were obtained at a flow rate of 18 μL/minute. As the flow rate increased to 32 μL/minute, the miniaturized MFC delivered maximum current and power densities of 15.51 Am^{-2} / 31020 Am^{-3} and 5.61 Wm^{-2} / 11220 Wm^{-3}, which corresponds to a more than 3.3 fold improvement when compared to the control. The volumetric power density of 11220 Wm^{-3} reported here is the highest power density reported and is over 28.5 times that of 3D nanostructured carbon-based electrodes[108].

Internal Resistance and Current/Power Density of Miniaturized MFCs Having Planar 2D and 3D Anodes. The internal resistance of MFCs significantly impacts current and power generation. According to chapter 2, the maximum areal current and power densities of an MFC are calculated as[56]:

$$i_{\max,areal} = \frac{I_{\max}}{A} = \frac{E_{OCV}}{R_i \cdot A}$$
$$p_{\max,areal} = \frac{P_{\max}}{A} = \frac{E_{OCV}^{\ 2}}{4R_i \cdot A} \tag{5.1}$$

where $i_{max, areal}$, $p_{max, areal}$, I_{max}, P_{max}, E_{ocv}, R_i, *and* A are the maximum areal current density, maximum areal power density, maximum current, maximum power, open circuit voltage, internal resistance, and electrode projected area, respectively. At a given configuration, both E_{OCV} and A are constants, so as the internal resistance decreases, the maximum areal and volumetric current/power densities increase. Internal resistances of the MFC with differing anodes were calculated by linearly fitting the ohmic region of the polarization curves in Fig. 5.3(a). Areal resistivity is internal resistance normalized to the anode area of 1 cm^2. The lowest internal resistance/areal resistivity of 219 Ω / 219 $\Omega \cdot cm^2$ is obtained by the 3D graphene scaffold. The single layer graphene and the control show relatively high internal resistance/areal resistivities, which are 2.2 and 7.4 times that of the 3D graphene scaffold, respectively. The areal resistivity of the 3D graphene anode is at least 4 fold lower than in previously reported carbon-based anode MFCs[150].

According to chapter 2, the internal resistance of the MFC can be subdivided by the following expression:

$$R_i = R_a + R_c + R_m + R_e \tag{5.2}$$

where R_i is the total internal resistance and R_a, R_c, R_m, R_e are the ohmic resistance of the anode, cathode, ion exchange membrane, and anolyte/catholyte, respectively. R_a is comprised of the ohmic resistance of the anode which includes the equivalent ohmic resistance of electron generation/transport from the exoelectrogen to the anode. R_a is a function of the electrical conductivity of the anode, the population of exoelectrogen, the mechanism of electron transfer from exoelectrogen to anode, the acidification inside the biofilm, as well as many other factors[43, 150]. R_c involves the ohmic resistance of the cathode, including the equivalent charge transfer resistance of reducing ions at the cathode. R_m is determined by the equivalent ohmic resistance of the proton exchange membrane. R_e is a function of the distance between the anode and cathode as well as the specific conductivity of the electrolyte. Prior studies report that R_e, R_m, and R_c are all low, in the order of 10 Ω or sub 10 Ω range[150]. Therefore R_a, the anode resistance, dominates the internal resistance. The anode resistance is believed to arise from the limited catalytic capability of the biofilm on the anode.

Catalytic reactions at the anode limit the power density of MFCs regardless of the planar 2D or 3D electrode configuration. The 2D graphene marks a lower internal resistance and higher current/power generation capability, suggesting that graphene has better electrochemical characteristics and biocompatibility when compared to the control. The 3D scaffold anode shows significantly lower internal resistance and higher current/power density over 2D counterparts. This agrees with prior studies on the rate-limiting step of the EET of exoelectrogens[132, 153, 160]. As the biofilm grows, the catalytic reactions of the biofilm become ineffective for current generation due to two contributing factors: (1) limited EET of exoelectrogens far from the anode and (2) an acidification effect derived from exoelectrogen proximity to the anode resulting in insufficient H^+ carrying buffer[63, 64, 132]. 3D porous electrodes solve these two challenges by including conductive grids. They are spaced by approximately 100-200 μm to minimize the ineffective EET of microbes located far from anode and potentially alleviate acidification inside the biofilm, which is supported by a uni-directional mass transfer model and experimental results. The two effects of facilitating EET and alleviating acidification yield substantially higher current / power densities when compared to planar 2D electrodes.

Besides the two effects, minimizing oxygen intrusion is also critical for obtaining a high power density of the *Geobacter*-enriched MFC. Unlike another commonly-adopted microbe, *Shewanella oneidensis* MR-1, *Geobacter sulfurreducens* demands oxygen-free environment to effectively harvest electrons. In macro-/meso-scale settings creating oxygen-free environment may not be a big challenge, however it is often very difficult to achieve oxygen-free environment in micro-scale devices. Many prior miniaturized MFCs used PDMS as the building material, which has a rather high oxygen permeability (52,531 cm^3 $mm/m^2/day/atm$)[13]. In a previous work by our group, Choi *et al.* 2011, we added *L-cysteine* into the anolyte to observe the impact of oxygen on the current/power density of *Geobacter sulfurreducens* based MFC[21]. The result suggested removing oxygen in the anode chamber becomes very effective to enhance current / power density. Since then, we replaced PDMS with glass, which has little oxygen permeability to minimize the oxygen intrusion for the formation of an optimized biofilm. The 3D graphene macroporous scaffold anode MFC was characterized for its CE to verify the mitigation in oxygen intrusion. The MFC marked a high CE of 83%, which suggests the successful mitigation of oxygen intrusion, when compared to 31% CE in previous work[21].

Table 5.2 lists a comparison of performance specifications of this work with prior art. Both the volumetric current and power densities are the highest among all MFCs, regardless of scale [25, 39, 42, 43, 108, 133]. The areal/volumetric current and power densities are 5.99/2.99 and 6.76/3.83 fold higher than previously reported miniaturized MFCs, respectively. These high current and power densities are attributed to the excellent biocompatibility characteristics of graphene and the high specific surface area of the 3D graphene scaffold structure.

Potential of Geobacter Sulfurreducens MFCs. Jiang *et al.* predicted a maximum current density of 10^6 Am^{-3} for *Geobacter sulfurreducens*[161]. This extrapolated prediction was calculated from the measured current of a single *Geobacter sulfurreducens* cell. Our record of 3.1×10^4 Am^{-3} is only 3.1% of the predicted maximum current density, leaving plenty of room for improvement. A number of different approaches to further improve the current density exist and include implementing sophisticated nanomaterial-based electrodes and genetically engineering exoelectrogens[162, 163].

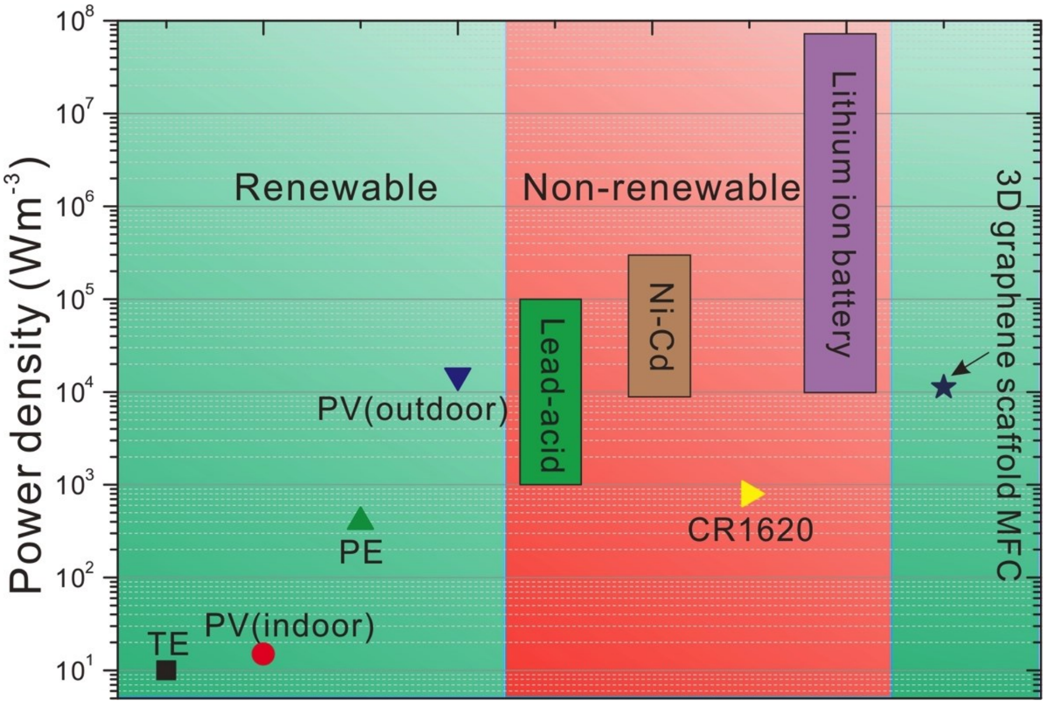

Figure 5.4. A comparison of the power density of the MFC with 3D graphene scaffold anode with different power sources and converters. Both renewable and non-renewable power sources are compared, including thermoelectricity (TE), piezoelectricity (PE), indoor photovoltaics (indoor PVindoor), outdoor photovoltaics (outdoor PV), lead-acid battery, nickel-cadmium (Ni-Cd) battery, lithium manganese dioxide battery (Sony CR1620) and lithium ion battery. The power density of the MFC with 3D graphene scaffold anode is one to three orders of magnitudes higher than TE, PE, PV(indoor) and lithium manganese dioxide battery (Sony CR1620), and comparable with PV(outdoor), lead-acid battery, Ni-Cd battery and lithium ion battery.

When compared to other types of both renewable and non-renewable power sources/converters, as illustrated in Fig. 5.4, the volumetric power density of the MFC with a 3D graphene scaffold is one to three orders of magnitudes higher than thermoelectricity (TE), piezoelectricity (PE), indoor photovoltaics, and commercially available lithium manganese dioxide batteries (Sony CR1620[137, 146]), and is comparable to commercially available outdoor photovoltaics (outdoor PV), lead-acid batteries, nickel-cadmium batteries, and lithium ion batteries[146]. The miniaturized MFC may find potential applications to supply power for low power electronics including sub-1mW low power microcontroller units, neural signal acquisition systems, wireless sensor networks, and implantable medical devices. Miniaturized MFCs also continue to show increasing potential within space exploration for power supply and waste treatment[138, 139, 140, 141, 164]. Several studies have reported higher power demands being met by stacking individual MFCs, indeed many of the technical challenges associated with stacking have been effectively addressed[165, 166]. The miniaturized MFCs may take a similar approach, being stacked in series and parallel to increase voltage and current readouts to enhance output power.

CHAPTER 6

ENHANCED CURRENT AND POWER DENSITY OF MICRO-SCALE MICROBIAL FUEL CELLS (MFCS) WITH ULTRAMICROELECTRODE (UME) ANODES

6.1. Introduction

Fossil energy is projected to deplete in the next one to two centuries, motivating the exploration of renewable energy sources as alternatives. Bioenergy is an attractive candidate due to the abundant biomass on the earth, its carbon-neutrality, and renewability. MFCs, which convert organic mass directly to electricity, are electro-chemical fuel cells harvesting electrons from organic substances, i.e., acetate, by catalytic reaction of specific bacteria species, named anode respiring bacteria (ARB) or electroactive bacteria, via their unique EET. The direct electrochemical conversion of MFCs results in high energy conversion efficiency. Miniaturized MFCs feature with small footprint, light weight, and potentially low cost, suitable for applications such as passive Radio Frequency (RF) tags, ultra-low power wireless sensor networks, implantable medical devices, and scientific research on ARB [56, 138, 141, 167, 168, 169].

Despite steady success of miniaturized MFCs over several years, the current and power densities of micro-scale MFCs, reported up to date, are magnitudes lower, compared with commercially available power sources, such as lithium ion battery (~100 W/m^2) [170]. Many approaches have been attempted to enhance the current/power density of micro-scale MFCs since the first report of a micro-scale MFC by Chiao *et al.* in 2002 [36]. Chiao *et al.* later used microfluidic channels to increase SAV [171], and Siu and Chiao implemented micropillars to further increase SAV [25]; Inoue *et al.* [42] and Mink *et al.* [108] presented high SAV anodes using carbon nanotubes; Jiang *et al*. implemented conductive nanofiber as 3D anode to reduce the start-up time and improve the performance[172]; Qian *et al.* [39] and Choi *et al.* [43] shortened the distance between anode and cathode to reduce the internal resistance, thereby enhancing the power density. We have presented micro-scale MFCs, having a high current and power densities up to 2.5 A/m^2 and 0.83 W/m^2 [150, 151, 170], respectively, the highest reported in micro-scale MFCs. However they are still one order of magnitude lower than that of macro-sized counterparts (30 A/m^2 and 6.8 W/m^2) [30].

Ultramicroelectrode (UME) is defined as an electrode having at least one dimension (such as width of band or radius of disk) smaller than 25 µm [173]. As the dimension of UME approaches the diffusion layer thickness, which describes the region at the vicinity of an electrode where concentration of organic substrate and buffer is different from that in the bulk, the diffusion of the substrate and buffer greatly enhances. UMEs have been used in many applications, including chemical sensing, material synthesis, and energy conversion, etc., where the performance significantly improves as the diffusion rate substantially enhances [174, 175].

Recently, Liu *et al.* 2010 implemented gold line UMEs, with a width of 10 µm, in ARB biofilm, and achieved a high current density of 16 A/m^2 [176]. Similarly, Pocaznoi *et al.* used a fine, 25 µm in diameter of platinum wire as UME in ARB biofilm, enhanced the diffusion of acetate, and thereby remarkably improved the current density, up to 66 A/m^2 [47].

The UME effect can be effectively adopted in a micro-scale MFC through microfabrication technique as geometries of MFC can be precisely controlled in accordance with the scale of diffusion layer thickness. This work aims to adopt the UME effect in a micro-scale MFC using micro-fabrication techniques to substantially improve the current/power density of micro-scale MFCs. In the next section, materials and methods are presented, including design, fabrication and operation of the UME anodes and micro-scale MFCs, as well as data analysis. Subsequently, experimental results are demonstrated, including the polarization curves, areal resistivity, biofilm/efficiency characterization. Following a discussion of the micro-scale MFCs along with other types of energy converters, a conclusion is drawn.

6.2. Materials and Methods

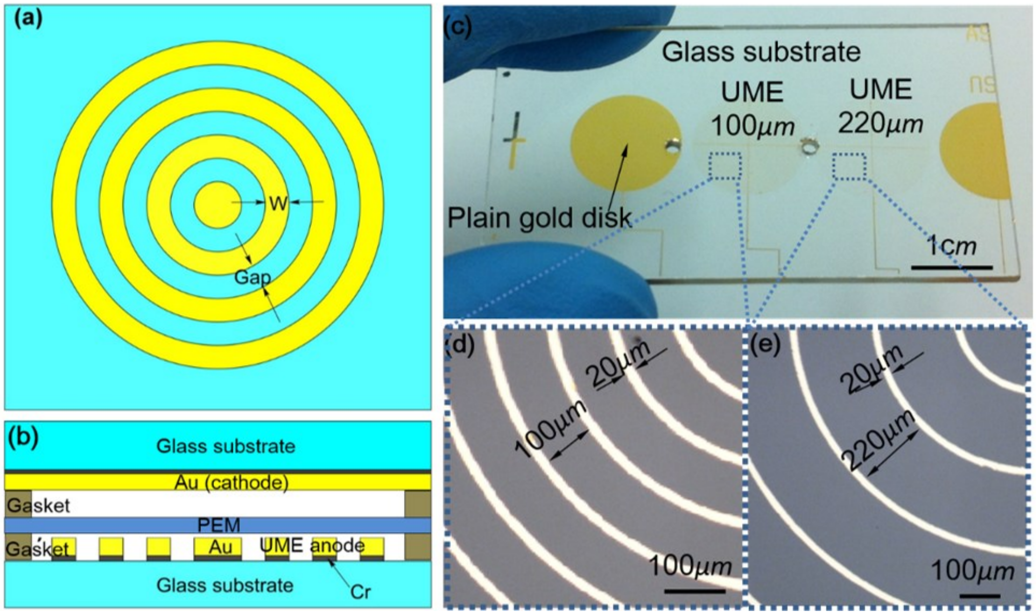

Figure 6.1. Schematic and optical image of the UME anodes. (a, b) Schematic of ultramicroelectrode (UME): top and cross-section views; the gap between the concentric rings is designed to improve diffusion rates of substrate and buffer; (c) Photo of the UME and plain gold disk anode; (d, e) Microscopic images of two UMEs; both have a concentric ring width of 20 µm, (d) one has a gap of 100 µm and (e) the other has a gap of 220 µm.

Micro-scale MFC Fabrication and assembly. Figure 6.1 shows a concentric ring-shape UME. The UME serves as the anode of a micro-scale MFC. The UME on a glass slide has a ring width of 20 µm. In order to explore the UME effect, we adopted two UMEs, having the ring width of 20 µm, in which the gaps between ring electrodes are 100 µm (Figure 6.1(d)) and 220 µm (Figure 6.1(e)), respectively, and a plain disk of having 5040 µm in radius is implemented as a control.

Diffusion layer thickness (δ) can be described by:

$$\delta = \frac{D}{k_d} = \frac{nFDcA}{l_i} = \frac{nFDc}{l_{i,areal}} \tag{6.1}$$

where D is the diffusion coefficient (0.88×10^{-9} m^2/s for acetate), k_d is the heterogeneous diffusion rate constant, F is the Faraday constant (96500 Cmol^{-1}), c is the concentration of substrate (acetate in this work), A is the geometric area of the electrode, n is the number of electrons in redox reaction, l_i is the limiting current, and $l_{i,areal}$ is the areal limiting current density. When n is 8 and c is 25 mol/m^3, areal limiting current density is computed at 165 A/m^2, projected based upon the prior art of using UME anodes, 66 A/m^2 at acetate concentration of 10 mM. Assuming the limiting current density is linearly proportional to the substrate concentration[173], we chose 165 A/m^2 of 25 mM acetate concentration, which gives δ of ~100 μm. The two UME gaps are chosen to be equal or larger than the diffusion layer thickness, to facilitate the mass transfer by the UME effect. The two UMEs and a disk-shaped plain gold disk anode are taken to explore the UME effect.

The fabrication of micro-scale MFC having UMEs starts with inlet/outlet formation. First, six through holes were drilled on a glass slide (46 mm × 26 mm × 1 mm, VWR), one as inlet, one as outlet and the rest four as screw holes. Then the glass slides were cleaned by piranha solution. Subsequently a layer of photoresist (AZ 4330, 4 μm thick) was patterned on the glass slide, and a layer of Cr/Au (20/400 nm) was deposited using a magnetron sputter (0.7 Pa, 150 mA for Cr and 45 mA for Au). The UME made of Cr/Au was patterned by lifting Cr/Au off in acetone. The optical microscopy images of the UMEs with a gap of 100 and 220 μm are shown in Figure 6.1 (d) and (e), respectively. A gold disk anode, control, was fabricated by the same process. Areas of the UME 100μm, 220 μm, and plain gold disk are 18.6 mm^2, 12.0 mm^2 and 82.6 mm^2, respectively. Three micro-scale MFCs are started for each type of anode.

The fabrication of cathodes also started with inlet/outlet formation. First, six through holes were drilled on a glass slide (46 mm × 26 mm × 1 mm, VWR), one as inlet, one as outlet and the rest four as screw holes. Then the glass slides were cleaned by piranha solution (concentrated H_2SO_4 and 30% H_2O_2, 3:1 volume ratio). Afterwards, a layer of Cr/Au (20/200 nm) was deposited using a magnetron sputter (0.7 Pa, 150 mA for Cr and 45 mA for Au).

Anodes, cathodes, proton exchange membrane (PEM, Nafion 117), silicone gaskets (250 µm thick, Fuel Store Inc.), nanoports (10-32 Coned assembly, IDEX), bolts and nuts were assembled to build the micro-scale MFCs, as shown in Figure 6.2. First, nanoports were glued to the inlet and outlet of anode and cathode glass slides by instant epoxy glue. Second, two rectangular silicone gaskets with dimensions of 46 mm × 26 mm × 0.25 mm were patterned with a hole of 1.414 cm in diameter at the center, in order to define the anode and cathode chamber volume of 39.25 µL. Third, a rectangular PEM with a dimension of 46 mm × 26 mm was cut. Finally, anode, cathode, conductive copper tape as interconnect, PEM and silicone gaskets were assembled, as illustrated in Figure 6.2 (a). Figure 6.2(b) shows the fabricated micro-scale MFC.

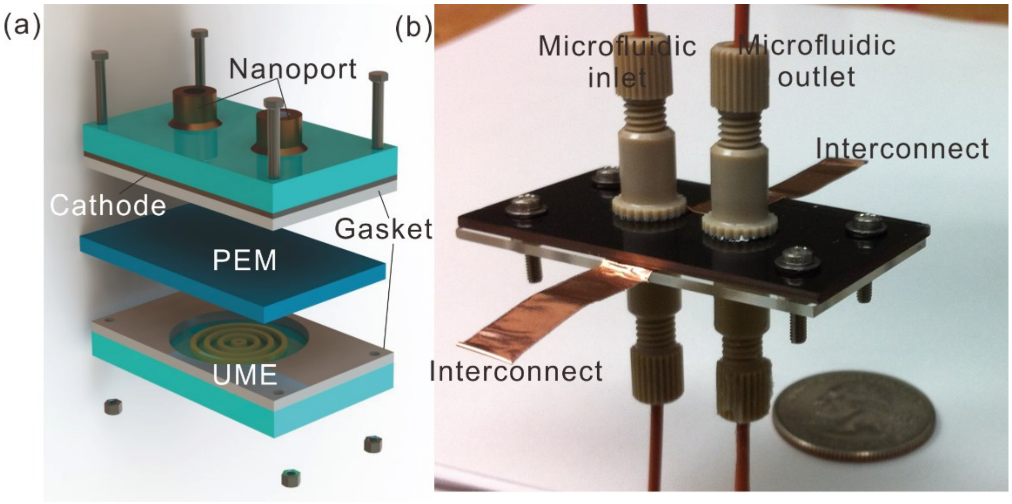

Figure 6.2. Schematic and optical image of the MFC with UME anode. (a) A schematic of a micro-scale MFC having UME anode and (b) Optical image of a fabricated micro-scale MFC.

Inoculum and Electrolyte. The inoculum for the micro-scale MFC was obtained from an acetate-fed microbial electrolysis cell (MEC) that had *Geobacter*-

enriched bacterial community originally from anaerobic-digestion sludge [177]. The anolyte is 25-mM sodium acetate in 100-mM Phosphate Buffer Solution (PBS) with 1,600 mg NaCl, 380 mg NH_4Cl, 5 mg EDTA, 30 mg $MgSO_4 \cdot 7H_2O$, 5 mg $MnSO_4 \cdot H_2O$, 10 mg NaCl, 1 mg $Co(NO_3)_2$, 1 mg $CaCl_2$, 0.001 mg $ZnSO_4 \cdot 7H_2O$, 0.001 mg $ZnSO_4 \cdot 7H_2O$, 0.1 mg $CuSO_4 \cdot 5H_2O$, 0.1 mg $AlK(SO_4)_2$, 0.1 mg H_3BO_3, 0.1 mg $Na_2MoO_4 \cdot 2H_2O$, 0.1 mg Na_2SeO_3, 0.1 mg $Na_2WO_4 \cdot 2H_2O$, 0.2 mg $NiCl_2 \cdot 6H_2O$, and 1 mg $FeSO_4 \cdot 7H_2O$ (per liter of deionized water) (pH 7.8 ± 0.2). For start-up process, inoculum and anolyte are mixed with 1:1 volume ratio as anolyte. The catholyte is 50-mM potassium ferricyanide in 100-mM PBS (pH 7.4). Anolyte and catholyte were supplied to the MFC through a syringe pump (PHD 2000, Harvard Apparatus).

Operation Conditions. The voltage profiles of the MFCs were recorded by a data acquisition system (DAQ/68, National Instrument). Voltage drop across an external load resistor connected between the anode and cathode was recorded every minute using a Labview Interface (National Instrument). The MFCs run on continuous mode unless specifically mentioned. During the start-up process, the MFCs were operated at a flow rate of 0.5 μL/min and at an external load resistor of 148 Ω. Once the start-up process completed, flow rates were increased to 2 μL/min, 4 μL/min, 6 μL/min, and 8 μL/min. Upon changing the flow rate, the MFCs were left to reach quasi-steady state, usually in approximately 12 hours. Then polarization curves were obtained by recording voltage across a series of resistors connected between the anode and cathode, ranging from 148 Ω to 1 MΩ.

For each resistor, a period of 10-15 minutes are waited until the voltage is stable. Coulombic efficiency (CE) and energy conversion efficiency measurements were performed by stopping the anolyte supply while maintaining the catholyte supply. By limiting the anolyte supply we were able to measure the current over time until the current became less than 10 μA. Integrating the current over time allows to calculate total coulombs produced by *Geobacter* at a given anode chamber volume, indicating how effectively a MFC can harvest electrons.

Data Analysis. The current through external load resistor was calculated via Ohm's law: $I = V/R$, where V is the voltage across the resistor, measured by the data acquisition system. MFC output power was calculated via Joule's law: $P = I^2 \cdot R$. The current and power densities reported in this paper were all normalized on unit of anode surface area and anode volume, and the corresponding areal and volumetric current/power density were calculated by $I_{areal} = I/A$, $P_{areal} = P/A$ and $I_{volumetric} = I/V$, $P_{volumetric} = P/V$, where A and V are the anode surface area and anode chamber volume, respectively. Polarization curves were obtained by measuring the voltage across a series of external loads, plotting current densities versus voltage and power densities. The highest areal and volumetric current/power densities were determined by locating the maximum current/power density in the polarization curves. Internal resistance of MFCs were obtained by linearly fitting the linear region of the polarization curve, and areal resistivity was calculated by normalizing the internal resistance of each MFC to the anode area. CE is the ratio of total coulombs harvested by MFCs from breaking down organic substrates (in our case, acetate) to the maximum possible coulombs if all organic substrates are consumed to produce current: $CE = C_P/C_T \times 100\%$, where C_P is the total coulombs calculated by integrating the current over the time and C_T is the maximum available coulombs of the substrates, $C_T = V \times b \times A \times e \times c$. V is the volume of anode chamber (m^3), b is the number of moles of electrons produced by oxidation of 1 mole of substrate (b = 8 mol e^-/mol acetate), A is Avogadro's number (6.023×10^{23} molecules/mol), e is electron charge (1.6×10^{-19} C/electron), and c is concentration of biomass in the anode chamber (c = 25 mol/m^3, sodium acetate).

Energy conversion efficiency is the ratio of the total energy harvested by a MFC to the maximum possible energy that the biomass can produce (standard molar enthalpy (heat) of biomass): $\eta = E_P/E_T \times 100\%$, where E_P is the energy harvested by MFC, calculated by integrating output power over the time and E_T is the maximum possible energy of the biomass $E_T = V \times c \times \Delta_f H°$. V is the volume of anode chamber (m^3), c is the concentration of biomass in the anode chamber (c = 25 mol/m^3, sodium acetate), $\Delta_f H°$ is the standard molar enthalpy (heat) of formation (872.711 KJ/mol for acetate)[178].

SEM Imaging of Biofilm. The MFCs were disassembled, rinsed in PBS, and biofilm on the UME anodes were fixed in 2 % glutaraldehyde solution overnight at 4 °C (Glutaraldehyde solution, Grade I, 25 % in H_2O, Sigma Aldrich). Samples were then dehydrated by serial, 10 minutes transfers through 50%, 70%, 90%, and 100% ethanol. Samples were examined using a Field Emission Scanning Electron Microscopy (FESEM) (Hitachi S-4700-II). Voltage of the electron gun was set to be 15 kV.

6.3. Results

Polarization curves. All MFCs completed their start-up process in 3.5 days. Then, flow rates were increased and polarization curves were obtained, as illustrated in Figure 6.3. As flow rate increases, the current and power densities increases for all three types of anodes, which is due to improved mass transfer of acetate and H^+ carrying buffer into the biofilm, and it is in accordance with previous studies[151]. At a higher flow rate (i.e., 8 μL/minute), the current and power density decreases, we believe it might be due to the detachment of biofilm at a high flow rate. The plain gold disk MFC for the control group demonstrate a maximum current and power density of 5.31 A/m^2 and 1.98 W/m^2. The MFC with 100 μm gap UME anode marked a highest current and power density of 17.7 A/m^2, 7.72 W/m^2, which is 3.3-fold and 3.9-fold respectively of the corresponding performance of the plain gold disk MFC (Figure 6.3). The MFC with 220 μm gap UME marked a highest current and power density of 15.03 A/m^2 and 6.75 W/m^2, which is 2.8-fold and 3.4-fold, respectively of the corresponding performance of the plain gold disk MFC. The performance enhancement between the two UMEs are similar. This enhancement is primarily due to the UME anodes, allowing higher the mass transfer of acetate and H^+ carrying buffer into the biofilm, which is in agreement with previous studies[47, 176]. As is shown, both UME anodes mark higher current densities over the control at any given potential, suggesting that the enhanced mass transfer of the substrate is account for the current and power improvement.

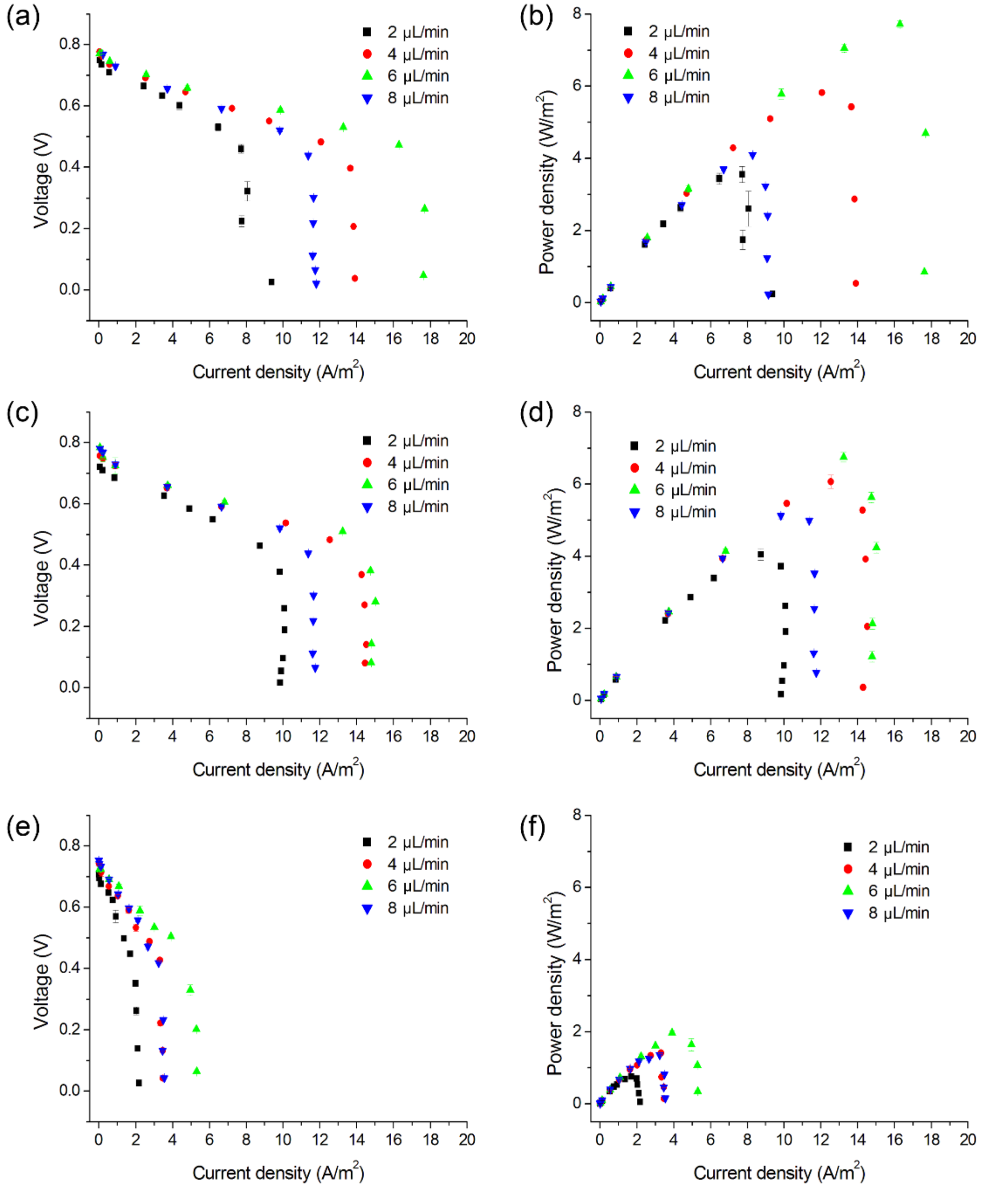

Figure 6.3. Polarization curves for the MFCs. (a, b) voltage and power density versus current density of MFC with 100 μm UME, (c, d) of MFC with 220 μm UME, and (e, f) of MFC with plain gold disk anode (control).

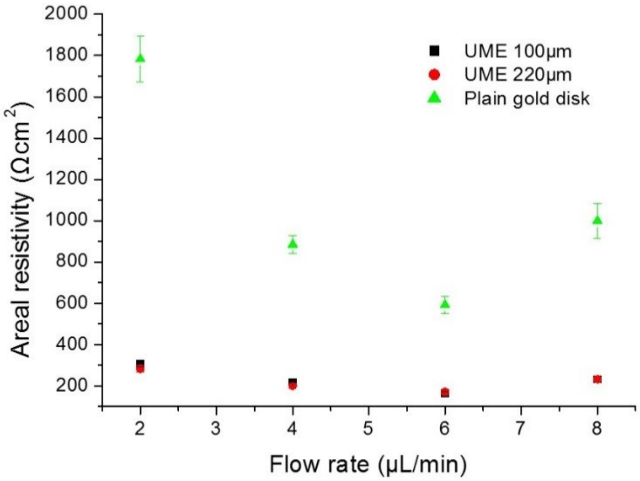

Figure 6.4. Areal resistivity versus flow rates of the MFCs. As flow rate increases, the areal resistivity reduces, and the lowest values are all obtained at 6 μL/min. When flow rate further increases, the areal resistivity increases, possibly due to high flow rate cause the detachment of biofilm.

Areal resistivity. Internal resistance and areal resistivity were calculated based on the polarization curves (Figure 6.4). According to Ren et al. 2012, areal resistivity, which is the internal resistance normalized to a unit surface area, is effective for comparing different MFCs and thus we compared the areal resistivity. As flow rates increased from 2 μL/min. to 6 μL/min., areal resistivity for all MFCs decreased, in accordance with the increase of the power and current density. At a higher flow rate (i.e., 8 μL/minute), areal resistivity of all three MFCs increased; similar to the power density, this is possibly due to the detachment of biofilm. The areal resistivity of 165 Ω·cm^2 and 171 Ω·cm^2 were at least one order of magnitudes lower than that of prior art of micro-scale MFCs.

Biofilm Characterization. Figure 6.5 shows SEM images of the biofilm on the UME and control. *Geobacter* formed a thick and dense biofilm on the UME anodes. The width of metal ring (20 µm) and biofilm (50 µm) were marked. The biofilm extended out of the UME laterally by ~15 µm on both sides. Outside of the 15 µm from the anode, *Geobacter* spread sparsely on the glass slides. This biofilm profile is similar to the SEM images of Liu *et al.* [176], and the extension limit of 15 µm agrees well. It was believed that when *Geobacter* are located far away from anode, they cannot form a thick and dense biofilm due to the limitation in long range EET [132, 176, 179]. The sparse *Geobacter* on the glass slide may rely on oxygen or minute EET to the anode, and their electricity generation capability is negligible.

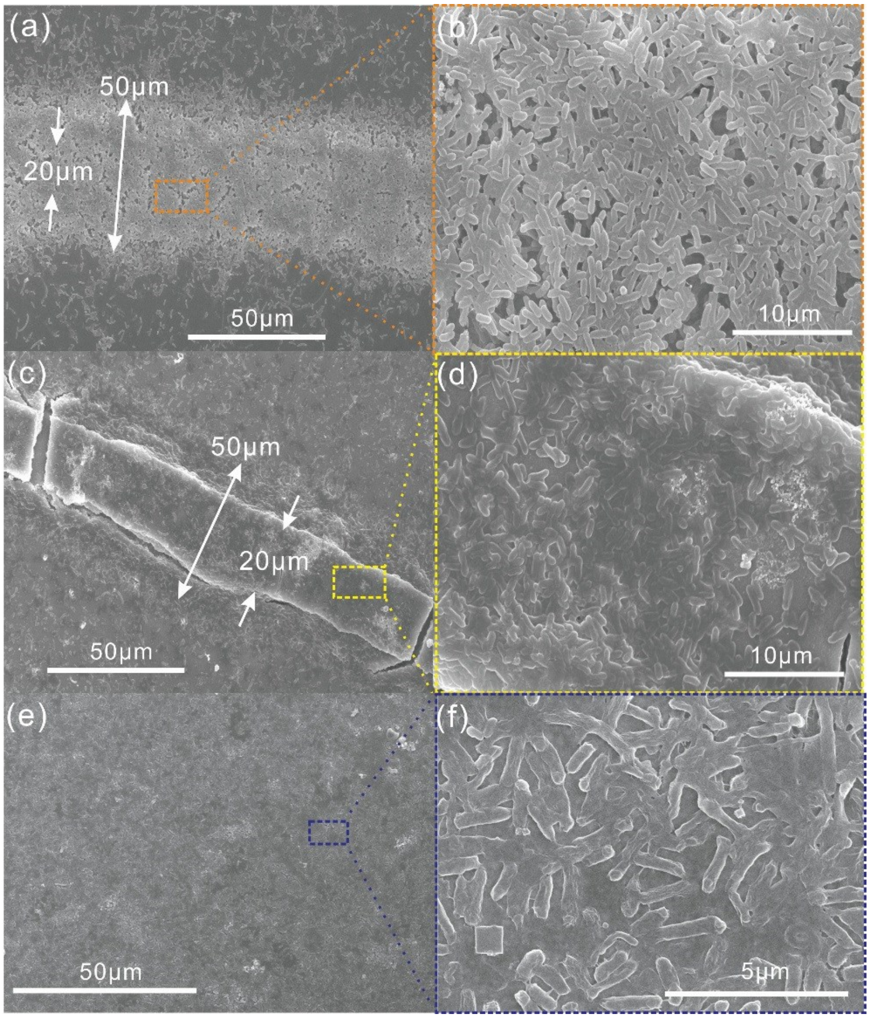

Figure 6.5. SEM images of the biofilm on UME anodes. (a) biofilm on UME 100 µm: the metal ring of 20 µm and the biofilm on the ring of 50 µm show the biofilm extends outwards ~ 15 µm of the edge of electrode; (b) Zoomed-in view of (a); (c) biofilm on UME 220 µm. Similar to (a) biofilm extends outwards ~ 15 µm of the edge of electrode; (d) Zoom-in view of (c). (e) biofilm on plain gold disk anode, biofilm on the plain gold disk anode is not as thick as (a) and (c), only a few layers of *Geobacter* exist; (f) Zoom-in view of (e).

The effective area of biofilm, which denote the area where thick biofilm forms, was 2.5 times of the anode area of the concentric ring-shape UMEs whereas that of the plain gold disk electrode remained almost constant. This was because the area of the disk electrode, 82.6 mm^2, was significantly larger than the increased biofilm area. Taking into consideration of the increase of effective area of biofilm, the areal power density normalized to the biofilm area were 3.09 W/m^2 and 2.70 W/m^2 for 100 μm and 220 μm gap UMEs, resulting in a power density of 56 % and 36 % improvement compared with that of the control. This power density enhancement was due to the mass transfer improvement induced by the edge effect of UME anode.

Significant power enhancement was expected on MFCs equipped with UME anodes over the plain gold disk electrode. However, the power densities of these two MFCs with UMEs demonstrated rather moderate improvement, less than expected. Two possible reasons accounted for the rather incremental power enhancement: (i) although the mass transfer at the vicinity of biofilm on the UME was enhanced, yet the mass transfer inside the biofilm was still limited. Effective diffusion coefficient of acetate inside biofilm is one fourth of that in aqueous solution, due to the presence of microbial cells, extracellular polymers, *etc.* [180]. Consequently, mass transfer of acetate and H$^+$ carrying buffer was lower in the biofilm than in the anolyte, which resulted in insufficient acetate and acidification inside biofilm, limiting the current and power; (ii) the electrons generated by *Geobacter* far from the anode had lower transfer rate into the anode, resulting in the limitation of breathing for *Geobacter* far from anode, impeding the growth of biofilm. Liu *et al.* reported the maximum biofilm extension from the edge of electrode is also 15 μm and one possibility of the maximum extension is due to the limitation on EET for the *Geobacter* located far from the electrode [176].

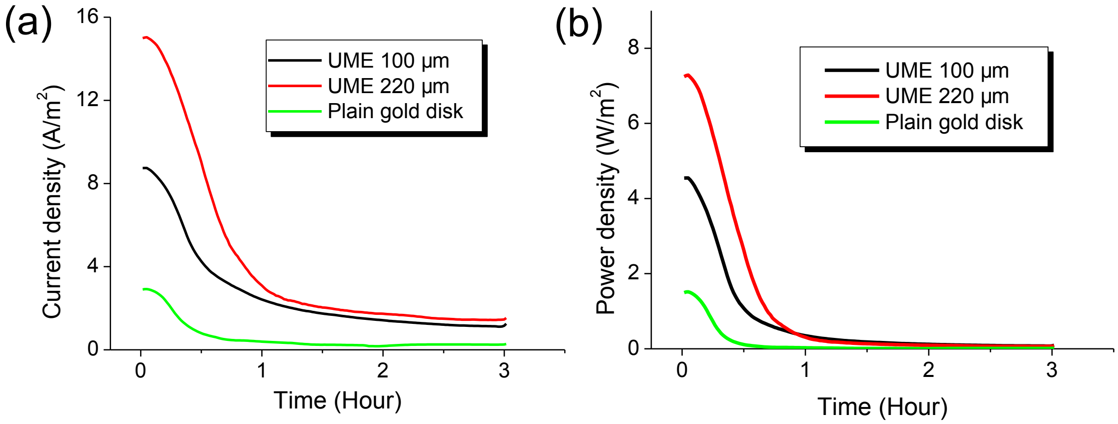

Figure 6.6. Coulombic efficiency and energy conversion efficiency measurement of the MFCs with UME anodes. (a) Current density versus time chart for CE measurement and (b) Power density versus time for energy conversion efficiency measurement for the micro-scale MFCs with different anodes.

Efficiency Characterization. CE and energy conversion efficiency measurements are depicted in Figure 6.6. All three MFCs achieved high CEs: the UME 100 µm, 220 µm and plain gold disk anodes of MFCs marked 70.2 %, 71.4 %, and 67.4 %, respectively. These high CEs indicate that the micro-scale MFCs successfully mitigated oxygen intrusion to the anode chamber. The energy conversion efficiency for the micro-scale MFCs were 16.2 %, 17.2 % and 15.1 %, respectively. Table 6.1 shows typical conversion efficiencies of various electricity conversion techniques[181]. The energy conversion efficiency in our work is comparable to some of these electricity conversion techniques.

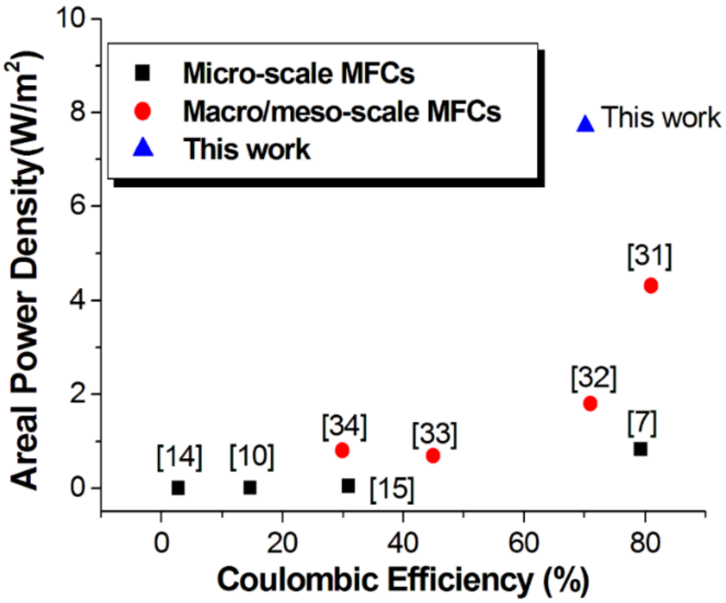

Figure 6.7. A comparison of areal power density and CE of this work with those of existing macro/meso (Rabaey et al. 2003 [92], Fan et al. 2007 [31], Liu et al. 2008 [134], Shimoyama et al. 2008[135]) **and micro-scale MFCs** (Siu and Chiao 2008 [25], Qian et al. 2009 [39], Choi et al. 2011 [43], Ren and Chae 2012 [170]).

Table 6.1. Efficiency of electricity conversion techniques in comparison with this work.

Electricity conversion techniques	Efficiency
Steam turbine fuel-oil power plant	38-44%
Steam turbine coal-fired power plant	39-47%
Large gas turbine (MW range)	up to 39%
Wind turbine	up to 35%
Nuclear power plant	33%-36%
Geothermal power plant	up to 15%
Photovoltaic cells	up to 15%
Protons Exchange Membrane Fuel Cell (PEMFC)	40%
Biomass gasification combined cycle power plant	40%
Waste-to-electricity power plant	22-28%
MFC with UME anode	17%

6.4. Discussions

Table 6.2 summaries the performance matrix of this work versus that of prior art. The areal power density of this work marks the highest among all micro-scale MFCs to date, very close to that of macro-scale counterparts. Figure 6.7 shows the chart of areal power density and CE of this work versus some representative micro-scale (Siu and Chiao 2008 [25], Qian et al. 2009 [39], Choi et al. 2011 [43], Ren and Chae 2012 [170]) and macro/meso-scale MFCs (Rabaey et al. 2003 [92], Fan et al. 2007 [31], Liu et al. 2008 [134], Shimoyama et al. 2008[135]).

Table 6.2. Summary table of this work in comparison with prior art.

Reporters	[4]	[9]	[11]	[39]	This work
Anode volume [μL]	100	1.5	4.5	350	**39.3**
Anode area [cm^2]	4	0.25	2.25	0.01	**0.186**
Anode/cathode material	Gold	Gold	Gold	Gold	**UME/gold**
Anolyte	Acetate	Lactate	Acetate	Acetate	**Acetate**
Catholyte	Ferricyanide	Ferricyanide	Ferricyanide	Ferricyanide	Ferricyanide
Ion exchange membrane	Nafion	Nafion	Nafion	Nafion	**Nafion**
Inoculum	Geobacter enriched	Shewanella MR-1	Geobacter enriched	Geobacter enriched	Geobacter enriched
Internal resistance [kΩ]	1.39	NA	10	NA	**0.9**
Areal resistivity [$k\Omega\cdot cm^2$]	2	NA	22.5	NA	**0.167**
P_{areal} [W/m^2]	0.83	0.0196	0.047	0.12	**7.72**
$P_{volumetric}$ [W/m^3]	3320	392	2333	3.4	**3658**
Power output **[**μ**W]**	332	0.49	10.6	0.12	**144**
CE [%]	79.4	NA	31	NA	**70.2**
Energy conversion efficiency [%]	NA	NA	NA	NA	**15-17**

A more suitable UME to be investigated is the wire type UME, which benefit from the diffusion enhancement from all the directions, while the planar UME in this dissertation can only benefit from the diffusion enhancement from on top of the planar electrode. Thus, we believe in the future, if the wire type UME is implemented, the performance of the MFC will further improved.

The micro-scale MFCs in this work may find applications in powering ultra-low power electronics, such as low-power wireless sensor network and passive RFID tags, especially in long-term environmentally unfriendly conditions, where it is difficult to approach for regular maintenance [138, 140, 141, 182]. The power density presented in this work is comparable, or slightly higher than conventional energy conversion techniques (Table 6.3) [136, 137, 138].

Table 6.3. A comparison of the power density of micro-scale MFCs in this work with existing conventional energy conversion approaches.

Energy source	Harvested power density
Ambient light (indoor)	0.1 W/m^2
Ambient light (outdoor)	100 W/m^2
Vibration/motion	4 W/m^3
Thermoelectric energy	60 W/m^3
RF energy	0.01 W/m^2
MFC with UME anode (bioenergy)	**7.72 W/m^2 & 3658 W/m^3**

CHAPTER 7

REGULATING THE RESPIRATION OF MICROBE: A BIO-INSPIRED HIGH PERFORMANCE MICROBIAL SUPERCAPACITOR WITH GRAPHENE BASED ELECTRODES AND ITS KINETIC FEATURES[179]

7.1. Introduction

Supercapacitors, or electro-chemical capacitors, are attractive due to their high current and power densities, free of maintenance, and high shelf/cycle lifetime [183, 184]. Most supercapacitors utilize materials of either high specific area, such as activated carbon, carbon nanotubes, and graphene; others utilize pseudo-capacitive materials, such as metal oxides (RuO_2) [185]. Inspired by the recent bloom of bio-inspired materials and devices research [186, 187, 188, 189], biological pseudo-capacitance, which includes redox cofactors inside biological entities, might be promising energy storage materials, due to its abundance, renewability, carbon neutrality and environmental friendliness, to replace conventional redox-based pseudo-capacitance made from non-renewable materials [190]. However, biological pseudo-capacitance often fails to transfer electrons between biological entities and electrodes as the outer membranes of cells prohibit the exchange of electrons between redox cofactors inside of cells and the electrodes. One exception to this is specific species of bacteria used in microbial electrochemical technologies, named exoelectrogens or air respiring bacteria (ARB). Their unique capability allows transferring electrons outside their bodies to electrodes to complete their respiration, named extracellular electron transfer (EET).

Exoelectrogens are implemented in various microbial electrochemical technologies (METs), such as microbial fuel cells (MFCs), microbial electrolysis cells (MECs), microbial reverse electrodialysis cells (MRCs), *etc.* [37, 85, 128, 191, 192, 193]. Recently, several reports have demonstrated that exoelectrogens, such as *Geobacter, Shewanella,* and *Proteobacteria*, store electrons, which could be used as capacitors [194, 195, 196, 197, 198, 199, 200, 201], having current density in the range of 1.2 – 90 A/m^2. The high current density observed in these reports demonstrated the ability to use biological pseudocapacitance as a potential carbon-neutral and renewable method for energy generation and storage.

In this chapter, we present a high performance microbial supercapacitor with both single layer graphene and 3D graphene scaffold anodes which store and release electrons produced by the metabolism of *Geobacter spp*. The microbial supercapacitor significantly enhances the current and power density by more than one order of magnitude over those of conventional microbial electrochemical technologies. Stability of the microbial supercapacitor is evaluated by high cycle stability of more than one million cycles. The charging and discharging characteristics of microbial supercapacitor also allows us to study the kinetics of electron transfer without significant damage to biofilm. By fitting a kinetics model to the discharging current profiles at initial-stage and fully-grown biofilms, the microbial supercapacitor offers quantitative measurements of kinetics parameters, which are critical for understanding EET of ARB.

7.2. Materials and Methods

Inoculum. The inoculum for the microbial supercapacitor was obtained from an acetate-fed microbial electrolysis cell (MEC) that had a *Geobacter*-enriched bacterial community originally from anaerobic-digestion sludge. The anolyte was composed of a 25-mM sodium acetate medium with 1,680 mg KH_2PO_4, 12,400 mg Na_2HPO_4, 1,600 mg NaCl, 380 mg NH_4Cl, 5 mg EDTA, 30 mg $MgSO_4 \cdot 7H_2O$, 5 mg $MnSO_4 \cdot H_2O$, 10 mg NaCl, 1 mg $Co(NO_3)_2$, 1 mg $CaCl_2$, 0.001 mg $ZnSO_4 \cdot 7H_2O$, 0.001 mg $ZnSO_4 \cdot 7H_2O$, 0.1 mg $CuSO_4 \cdot 5H_2O$, 0.1 mg $AlK(SO_4)_2$, 0.1 mg H_3BO_3, 0.1 mg $Na_2MoO_4 \cdot 2H_2O$, 0.1 mg Na_2SeO_3, 0.1 mg $Na_2WO_4 \cdot 2H_2O$, 0.2 mg $NiCl_2 \cdot 6H_2O$, and 1 mg $FeSO_4 \cdot 7H_2O$ (per liter of deionized water). For the start-up process, inoculum and anolyte were mixed at a volumetric ratio of 1:1. The catholyte was composed of 50 mM potassium ferricyanide in a 100 mM phosphate buffer solution. Both anolyte and catholyte were purged by nitrogen for 30 minutes before supplying to the supercapactor by a syringe pump (Harvard Instrument).

Total DNA extraction and 16S rRNA gene pyrosequencing. Biofilm was broken into small pieces using a traditional pestle. Total genomic DNA was extracted using a PowerSoil DNA isolation kit (MO-BIO) according to the manufacturer's protocol. Amplicon libraries were constructed for 454 sequencing using the primer set 926F (5′-AAACTYAAAKGAATTGACGG-3′) and 1392R (5′-ACGGGCGGTGTGTRC-3′). The amplification of 16S rDNA was performed in a final volume of 50 μL containing 5 μL of 10X buffer, 1μL of dNTP mixture (200 mM), 0.5 μL of (20XU) FastStart Taq DNA Polymerase (Roche), 1 μL of each primer (10 μM), 1 μL of DNA template (50 ng/μL) and water. The PCR conditions were as follows: 94 °C for 3 min; 30 cycles of 94 °C for 45 secs, 55 °C for 45 secs, followed by 72 °C for 1 min; and a final extension at 72 °C for 10 min. The PCR products were gel purified on 1% agarose gels using a Quick Gel Extraction Kit (Invitrogen). The purified 16 s amplicons were quantified with Picogreen and pooled in equal concentrations prior to emulsion PCR. Amplicon pyrosequencing was performed using a 454/Roche GS Junior instrument (454 Life Sciences). DNA quantification was performed using Nanodrop 2000 spectrophotometer (Nanodrop Technologies, Wilmington, USA). Sequencing was performed on the GS Junior system (454 Life Sciences).

Sequence analysis. The sffinfo command was used to extract fasta format (sequence data) and quality (quality scores) files from a raw.sff file with –s and –q options, respectively. The following steps were carried out by the QIIME (Quantitative Insights into Microbial Ecology). Output fasta and quality files were filtered to exclude sequences with lengths (<150 bp) and quality score (<50). Raw sequences with uncorrectable barcodes were removed. The remaining sequences were sorted by a mapping file to their relevant samples according to the barcode. The denoised dataset was clustered into operational taxonomic units (OTUs) with 97% similarity threshold, using the UCLUST algorithm. The representative sequences were selected and aligned with greengenes core set of aligned sequences using Pynast. Taxonomy was assigned using the greengenes database. Phylogenetic trees were constructed using the software MEGA V5 with the neighbor joining criterion, and 1,000 times of bootstrap resampling was performed to assess the confidence of tree topologies.

Start-up and Data acquisition. Anolyte/catholyte solutions were pumped into the corresponding chambers at a flow rate of 2 µL/min. A resistor of 148 Ω was connected across the anode and cathode of the supercapacitor. It typically took 5-6 days to form a mature biofilm. Once the start-up process completed, the flow rates slowly increased to 18 µL/min, and after reaching steady state, the supercapacitor was characterized through different electrochemical techniques.

Cyclic voltammetry. Cyclic voltammetry (CV) was measured by a potentiostat (Gamry Instruments). Anode potential was swept from -0.8 V to 0.3 V (all versus Ag/AgCl reference electrode in 3 M NaCl), at a scan rate of 10 mV/second and 100 mV/second respectively.

Measurement of cytochrome concentration in biofilm and conversion to charge storage. Biofilms were removed from electrodes using a pre-cleaned plastic blade and washed with PBS (phosphate buffered saline). Collected biofilms was immediately frozen in liquid nitrogen for 20 minute, and then stored in -80 °C freezer. After thawing, vortexing, sonicating, and centrifuging for 20 min at 5000 RPM, absorbance spectrum of supernatants were measured by UV-Vis spectrum analysis between 370-600 nm wavelength, as illustrated in Figure 7.4(c). The oxidized cytochrome heme had a distinct peak at 410 nm and the obtained absorbance value of that peak was used to calculate heme content weight (W_t) by fitting to a standard curve made with oxidized bovine heart *cytochrome* c (Sigma, MO, USA). For the conversion of *cytochrome* c to charge storage amount, one heme stores one electron. Thus the charge stored inside *cytochrome* c heme was calculated as $Q=W_t/M_r \cdot N_A \cdot e$, where M_r is the molecular weight of *cytochrome* c heme (M_r = 616.5 g/mol)[152, 195], N_A is the Avogadro's number (6.023×10^{23} molecules/mole), e is electron charge (1.6×10^{-19} C/electrons).

Non-linear fitting of discharging current derivation. Biofilm catalytic process is illustrated, including a series of 4 steps[201] (Figure D.1): (1) irreversible acetate turnover by exoelectrogens; (2) electron transfer from inside exoelectrogens to extracellular redox cofactors (ERC) in biofilm; (3) electron transfer from ERC in biofilm to ERC at the anode interface; (4) oxidization of the ERC at the anode:

$$\frac{1}{8}CH_3COOH + Mic_{ox} \xrightarrow{k_{ac}} Mic_{red} + \frac{1}{4}CO_2 + H^+ \tag{7.1}$$

$$Mic_{red} + \mathrm{Erc}_{ox} \xrightarrow{k_{mic}} Mic_{ox} + Erc_{red} \tag{7.2}$$

$$Erc_{red} + Erc_{ox,i} \xrightarrow{k_{erc}} Erc_{ox} + Erc_{red,i} \tag{7.3}$$

$$Erc_{red,i} \xrightarrow{k_{\mathrm{int}}} Erc_{\mathrm{ox},i} + e^- \tag{7.4}$$

where Mic_{ox}, Mic_{red}, Erc_{ox}, Erc_{red}, $Erc_{ox,i}$, $Erc_{red,i}$ denote the oxidized and reduced redox cofactor inside exoelectrogen, extracellular redox cofactors in biofilm matrix, and interface extracellular redox cofactors, respectively[201].

We fitted the kinetics parameters of the 4-step EET process to the transient discharging current profile for both initial and fully-grown biofilms. Detailed description of these kinetics parameters is described in appendix D. According to the models in appendix D, first-order rate constant parameters ($k_1=k_{int}$, $k_2=k_{erc}Erc_{total,i}$, $k_3=k_{mic}Erc_{total}+k_{ac}$), as well as Mic_{ox}, Mic_{red}, Erc_{ox}, Erc_{red}, $Erc_{ox,i}$, $Erc_{red,i}$ are extracted for initial and full biofilms. The current generated during discharging process can be written as:

$$\mathrm{I}_{total} = A\exp(-k_1 t) + B\exp(-k_2 t) + C\exp(-k_3 t) + D(1-\exp(-k_3 t)) \tag{7.5}$$

where

$$\begin{aligned}
&\mathrm{A} = F \cdot k_{\mathrm{int}} \cdot \mathrm{Erc}_{red0,i} \\
&B = F \cdot k_{\mathrm{erc}} \cdot \mathrm{Erc}_{\mathrm{total},i} \cdot Erc_{red0} \\
&C = F \cdot k_{erc} \cdot Erc_{total} \cdot Mic_{red0} \\
&D = \frac{F \cdot k_{ac} \cdot Mic_{total}}{k_{mic} Erc_{total} + k_{ac}} \\
&k_1 = k_{\mathrm{int}} \\
&k_2 = k_{\mathrm{erc}} \cdot Erc_{\mathrm{total},i} \\
&k_3 = \mathrm{k}_{mic} \cdot Erc_{total} + \mathrm{k}_{ac}
\end{aligned} \tag{7.6}$$

As a result, discharge profile for both initial and fully-grown biofilms were fitted through equation 7.5, as shown in Figure 7.4(a) and (b). The non-linear fitting constants (A, B, C, D, k_1, k_2, and k_3) were obtained during fitting and kinetic parameters are deduced (Table 7.1(a) and (b)).

6.3. Results and Discussions

A schematic of the exoelectrogen, *Geobacter spp.*, grown on both single-layer graphene and 3D graphene scaffold is shown in Figure 7.1(a) and (b). A high speed electrical switch was implemented to characterize a microbial supercapacitor, as shown in Figure 7.1(c). When the switch is turned off, *Geobacter* are unable to complete their breathing process, resulting in the storage of electrons in redox cofactors (charging step) (Figure 7.1(d)). When the switch is turned on, electrons stored inside redox cofactors are transferred to the anode, and then get oxidized at the cathode by oxidizers (discharging step) (Figure 7.1(e)).

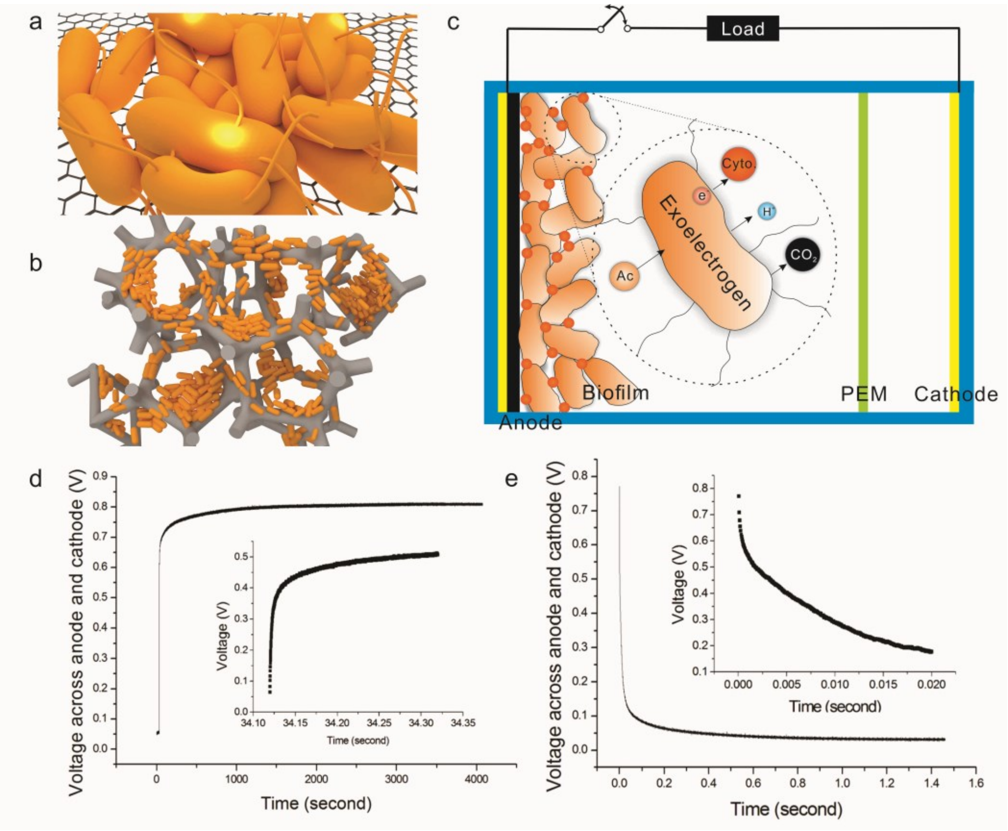

Figure 7.1. Schematic, charging and discharging profile of the microbial supercapacitor. (a) Schematic of the exoelectrogen grown on both single-layer graphene (a) and on 3D graphene scaffold (b); (c) schematic of the operation principle of the microbial supercapacitor: when the high speed switch is off, electrons are stored in redox cofactors; when the switch is on, electrons stored inside redox cofactors transfer to the anode and are oxidized at the cathode; (d) voltage across the microbial supercapacitor during charging step (inset: enlarged view of the first 0.2 seconds); (e) voltage across the microbial supercapacitor during discharging step, when a load of 100 Ω was used (inset: enlarged view of the first 20 mili-seconds).

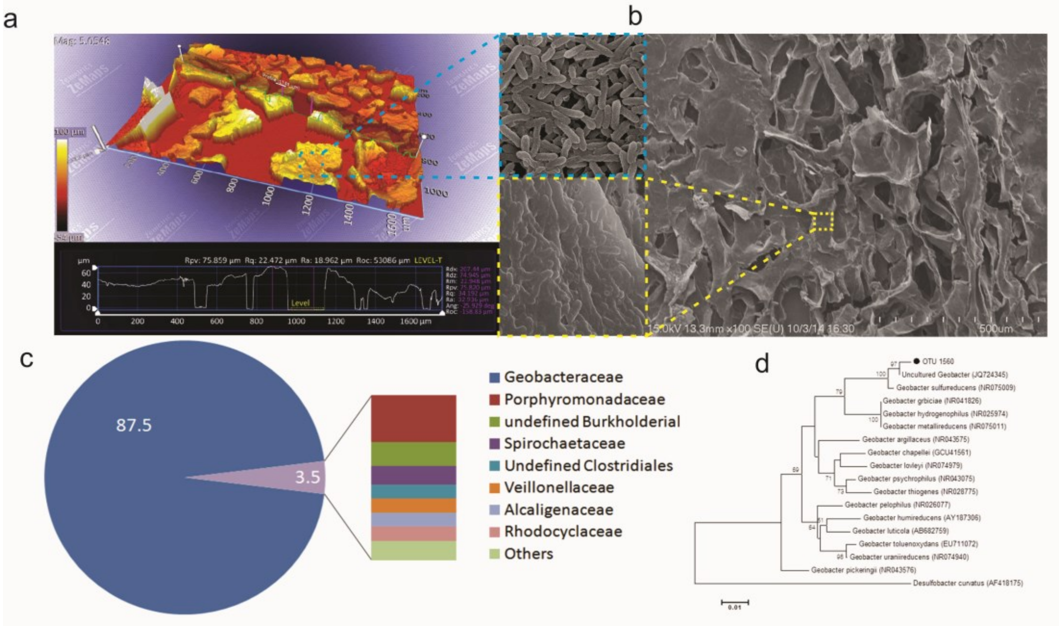

Figure 7.2. SEM images and community analysis of the microbial supercapacitor. (a) Morphology of biofilm on the single-layer graphene film imaged by optical interference microscopy and scanning electron microscopy. The thickness of biofilm was between 20-80 µm; (b) SEM image of biofilm on the 3D graphene scaffold, dense biofilm grew on the 3D scaffold; (c, d) representative bacterial families in the library of 16S rRNA sequence and neighbor-joining phylogenetic tree illustrating the relationship between OTU 1560 and related members of the family Geobacteraceae. The scale bar represents 1% difference in nucleotide sequences.

A single-layer graphene film prepared by chemical vapor deposition (CVD) on a thin film gold was used as a current collector due to its high conductivity and excellent electrochemical characteristics [202]. The sheet resistance of single-layer graphene film on the thin film gold was measured at 4.13 Ω/square. A 3D graphene scaffold prepared by CVD was also implemented due to its higher specific area and lower sheet resistance (Figure C.4). The specific surface area of 3D graphene is 850 m^2g^{-1} [158], which is comparable with those of activated carbon reported by Alvarez-Gallego *et al.* 2012 (299-745 m^2g^{-1}) [203] and

Zhang *et al.* 2014 (267-922 m^2g^{-1}) [204]. The sheet resistance of 3D graphene scaffold was measured at 0.335 **Ω**/square. Morphology and thickness of biofilm grown on the single-layer graphene was imaged with optical interference microscopy (Figure 7.2(a)). The thickness of biofilm islands was between 20 μm and 80 μm. A scanning electron microscope (SEM) image of biofilm shows rod-shaped bacteria (Figure 7.2(a) inset), commonly found in the biofilm of MFCs [69, 205, 206]. Morphology of biofilm grown on the 3D graphene scaffold was visualized using SEM, and dense biofilm grew on the graphene scaffold (Figure 7.2(b)). 16S rRNA gene pyrosequencing identified the most predominant family *Geobacteraceae* accounting for 87.5% of total 9,813 sequences. The neighbor-joining phylogenic tree showed that the majority of OTU 1560 in the family *Geobacteraceae* had 98.9% similarity to uncultured *Geobacter* (JQ724345), and *Geobacter sulfurreducens* (NR075009, 97.9% sequences similarity) (Figure 7.2(c) and (d)). This result shows that *Geobacter spp.* are the major exoelectrogen in the biofilm.

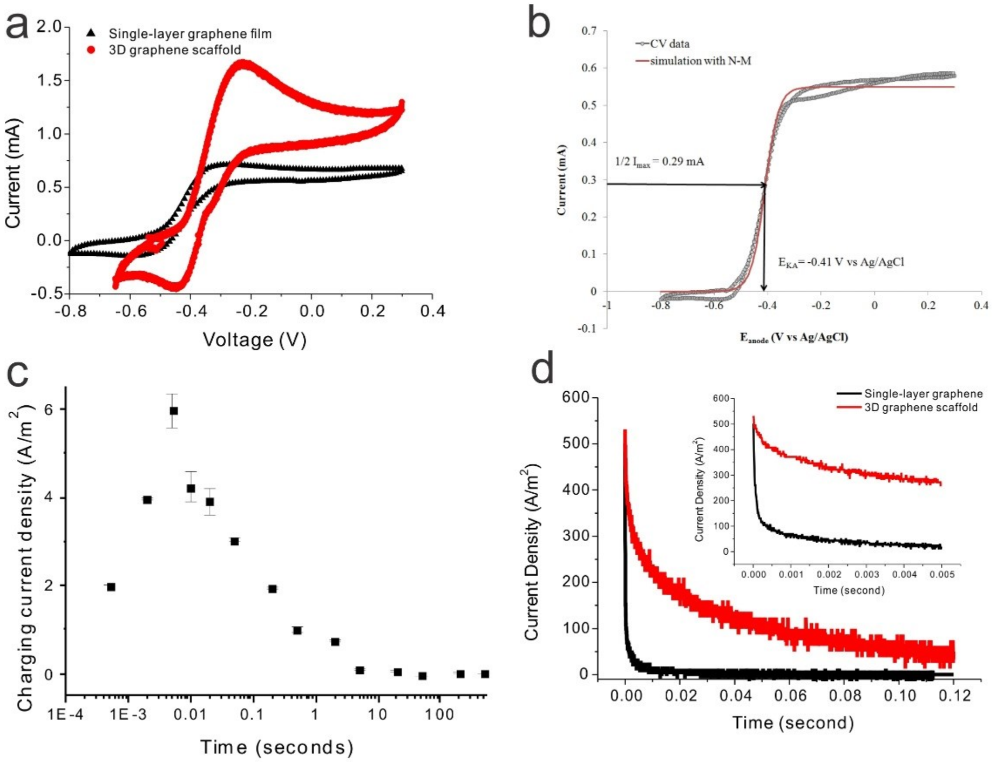

Figure 7.3. Electrochemical characterization of the microbial supercapacitor. (a) cyclic voltammetry of biofilm at a scan rate of 100 mV/s for both single-layer graphene film and 3D graphene scaffold. Pseudocapacitance was observed by the CV measurement; (b) Cyclic voltammetry at a scan rate of 10 mV/s and simulated results with Nernst-Monod equation for the supercapacitor with single layer graphene film. The maximum current (I_{max}): 0.58 mA, the half-saturation potential (E_{KA}): -0.41 V vs. Ag/AgCl, the half-saturation concentration (K_s): 1.86 mA, acetate concentration at steady state (S) 25 mM in the supercapacitor; (c) charging characteristics of the supercapacitor; (d) discharging characteristics when a load of 7 Ω was connected. Substantially high current and power density, 531.2 A/m^2 / 1,060,000 A/m^3, and 197.5 W/m^2 / 395,000 W/m^3 are marked, which is 1-2 orders of magnitude higher than previously reported microbial electrochemical techniques; (inset: Discharging current in the first 5 mili-seconds).

Figure 7.3(a) shows the cyclic voltammetry (CV) curve of the supercapacitor with single-layer graphene film and 3D graphene scaffold, respectively, at scan rate of 100 mV/s. Pseudocapacitance was observed by the redox peaks in the CV curve. It is obvious that the biofilm on the 3D scaffold electrode demonstrates a significantly higher pseudocapacitance, due to the high specific surface area.

Figure 7.3(b) shows CV diagram at a scan rate of 10 mV/second for the supercapacitor with single-layer graphene film. This CV diagram is a sigmoidal curve commonly found in biofilm having *Geobacter sulfurreducens* or *Geobacter*-enriched culture [69, 154, 207], supporting the bacterial community analysis. The sigmoidal curve can be represented with Nernst-Monod equation. The maximum current was 0.58 mA in the supercapacitor, and the half-saturation potential (E_{KA}) was estimated at -0.41 V vs. Ag/AgCl for biofilm anode. This E_{KA} is close to literature, ranging from -0.45V to -0.43V in MFCs having *Geobacter spp.* as dominant exoelectrogens [69, 70]. We simulated an anode polarization curve with the Nernst-Monod equation

$$I = I_{max} \times (S/K_s+S) \times 1/(1+\exp(-\eta F/RT)) \qquad (7.7)$$

where I_{max}: the maximum current, S: substrate concentration (mol acetate/L), K_s: the half-saturation concentration (mol acetate/L), η: $E_{anode} - E_{KA}$, E_{anode}: anode potential (V), F: Faraday constant (96,485 J/V-mol), R: universal gas constant (8.3145 J/mol-K) , and T: temperature (K), and the simulated data well fits into CV (Figure 7.2(b)).

Charging and discharging current density of the microbial supercapacitor with a fully-grown biofilm were collected (Figure 7.3(c) and (d)) using a high speed data acquisition system (PXI 1020, National Instruments) at 100,000 samples/second. At the very beginning, the charging current density was low, and then it increased to its maximum, 5.7 A/m^2 at 5 mili-seconds. The charging current density gradually dropped near zero due to the accumulation of reduced redox cofactors inside biofilm, which stopped EET extracellular electron transfer to the anode and inhibited electron transfer in the upstream redox reactions from acetate to intracellular electron carriers. Discharging process was substantially faster than charging (Figure 7.3(d)). Discharging current and power densities reached as high as 531.2 A/m^2, and 197.5 W/m^2 with a load resistor of 7 Ω. The discharging current and power densities are more than one order of magnitude higher than those of MET in literature [30, 150]. The high current/power density could be partially due to the high reaction rate of redox cofactors at the vicinity of the anode [201]. Furthermore, a substantially high maximum volumetric current and power density of 1,060,000 A/m^3 and 395,000 W/m^3 is obtained., 2 orders of magnitude higher than those in literature [33, 34], and the maximum current density is even higher than a recent theoretically predicted steady state current density of *Geobacter* species.. The maximum transient discharging current density of our full-cell supercapacitor is 1.36 times of the maximum steady-state current density of a half-cell MET whereas the maximum areal / volumetric transient current and power densities are more than one order and two orders of magnitude higher than those at steady-state of full-cell MET in literature, respectively [30, 150]. Due to the higher pseudo-capacitance, the discharging process of the supercapacitor with 3D graphene scaffold anode demonstrates a longer discharging time.

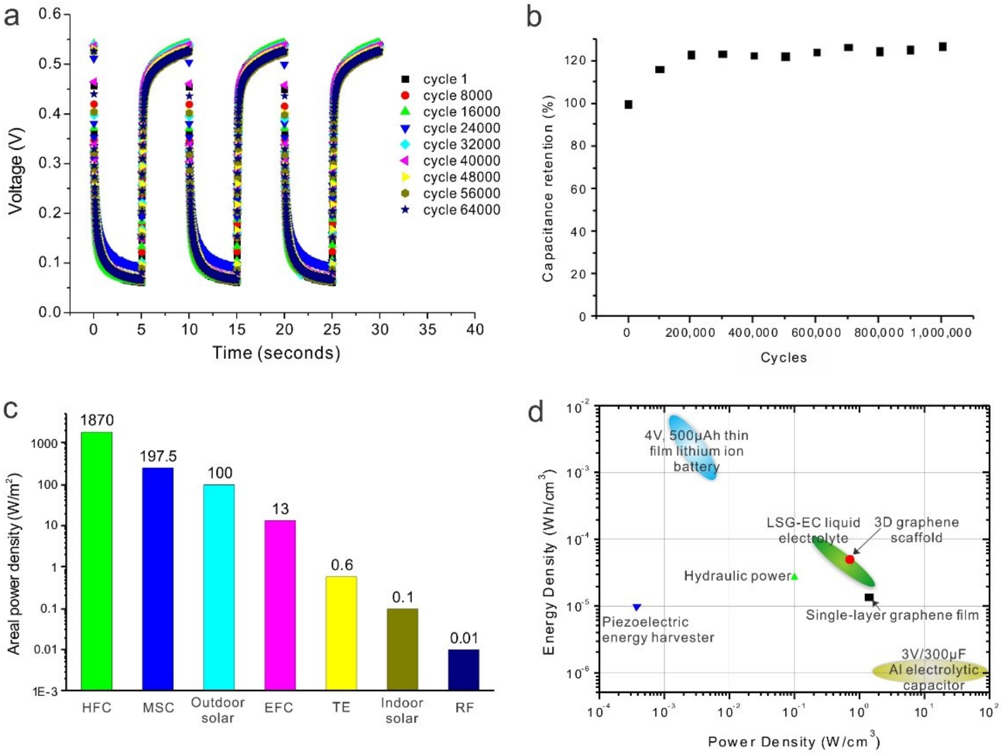

Figure 7.4. Cycle stability and performance comparison of the microbial supercapacitor. (a) charging/discharging characteristics of the supercapacitor with 3D graphene scaffold up to 64,000 cycles; (b) capacitance retention of supercapacitor with single-layer graphene film of 1 million cycles; (c) comparison of areal power density; here HFC, MSC, EFC, TE, RF stands for hydrogen fuel cell, microbial supercapacitor, enzymatic fuel cell, thermoelectric energy harvester, radio frequency energy harvester, respectively; (d) Ragone plot of the microbial supercapacitor: energy and power densities of the microbial supercapacitor with 3D graphene scaffold are compared with those of lithium ion battery, laser scribing electrochemical capacitor in liquid electrolyte (LSG-EC), and commercially available Al electrolytic capacitor. The energy and power densities of microbial supercapacitor are comparable with LSG-EC. Compared with carbon neutral and renewable energy, the energy density of microbial supercapacitor is slightly higher, and the power density is a few folds to two orders of magnitudes higher than hydraulic energy and piezoelectric energy harvester.

Cyclic charging and discharging of the microbial supercapacitor was performed for the cycle stability of the supercapacitor with 3D graphene scaffold anode and single-layer graphene film (Figure 7.4(a) and (b)). The microbial supercapacitor demonstrated excellent cycle stability. The charged and discharged voltages remained almost constant up to 64,000 cycles with a charging/discharging ratio of 25 second/25 second. The cyclic charging and discharging characteristics with different charging/discharging ratio were also performed for the supercapacitor with single-layer graphene film. The supercapacitor achieved a total cycle number of more than 1,000,000 comparable to or much greater than conventional electrochemical supercapacitors [208, 209] (Figure 7.4(b)). The high cyclic stability seems to be due to the excellent mechanical and electrochemical stability of 2D graphene film and 3D graphene scaffold in addition to the robust, self-immobilized and self-regenerating *Geobacter*-enriched biofilm [210]. Excellent specific capacitance was demonstrated by the microbial supercapacitor. Specific capacitance of the microbial supercapacitor with 3D graphene scaffold was measured to be 17.85 mF/cm^2, which is 5.6 times higher than the microbial supercapacitor with single-layer graphene film (3.20 mF/cm^2), which is believed to be due to the high specific area of the 3D graphene scaffold. The specific capacitance is more than two orders of magnitude larger than that of graphene-based in-plane supercapacitors [211], and 4.4 time of that of supercapacitor based on laser scribing graphene [184].

The power density and energy density of microbial supercapacitors are compared with other existing renewable and non-renewable batteries in addition to supercapacitors (Figure 7.4(c)). The areal power density of microbial supercapacitor is 2.5 fold, 19 fold, 3 orders of magnitude, and 4 orders of magnitude greater than those of solar cell, enzymatic fuel cell, thermoelectric energy harvester, and RF energy harvester, respectively [212]. The Ragone plot, Figure 7.4(d), shows that the energy density of microbial supercapacitor with 3D graphene scaffold is 3.8 fold of that of microbial supercapacitor with single-layer graphene film. The energy density and power density of microbial supercapacitor is comparable with those of laser scribing graphene electrochemical capacitor (LSG-EC) [184]. The power and energy densities of microbial supercapacitor is approximately one order of magnitude higher than those of Li thin-film battery and Al electrolyte capacitor [184, 211], respectively. As of carbon neutral and renewable converter/storage, the energy density and power density of microbial supercapacitor are slightly higher and a few fold to two orders of magnitude higher than hydraulic energy and piezoelectric energy harvester, respectively [213], suggesting the microbial supercapacitor may be an attractive candidate for renewable energy conversion and storage device.

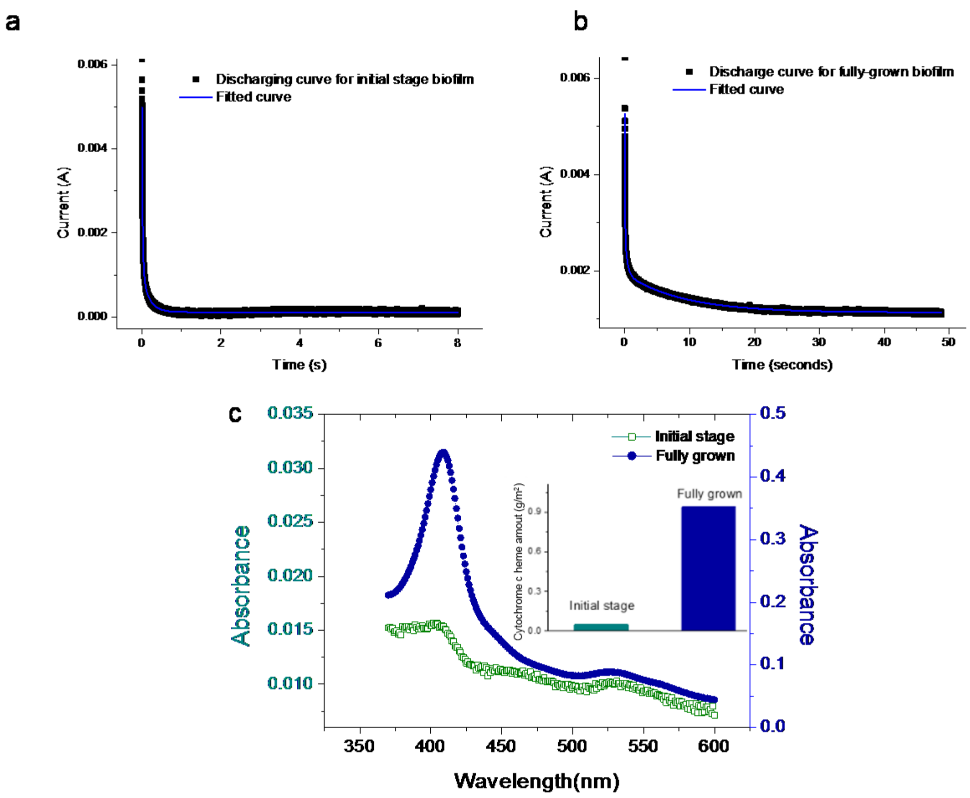

Figure 7.5. Non-linear fitting and optical spectrum analysis of the microbial supercapacitor to determine its kinetics features. (a, b) Non-linear fittings of discharging current for (a) initial and (b) full-grown biofilms; (c) absorbance spectrum of cytochrome c in initial and fully-grown biofilms (inset: a comparison of amount of cytochrome c in initial and fully-grown biofilms).

To further improve the performance of microbial supercapacitor and other microbial electrochemical techniques, understanding the limiting stage of EET is critical to facilitate the study of fundamental mechanisms within catabolic reactions in exoelectrogen [87, 201].

Through non-linear fitting of the discharging curve, quantitative comparison of kinetics between initial and fully-grown biofilms was performed. Initial and fully-grown biofilms exhibited steady-state current densities of 1 A/m^2 and 6 A/m^2, respectively. Catabolism of exoelectrogens is known to have a series of electron transfer steps, from acetate turnover, electron transfer from redox cofactors inside to extracellular redox cofactors (ERC), including outer membrane cytochrome (OMC) of exoelectrogen, through biofilm matrix, finally to the anode. These steps can be modeled by kinetic modeling, including the reaction rate constants of these steps are k_{ac}, k_{mic}, k_{erc}, and k_{int}, respectively. The temporal discharging current profile and electron transfer profile of a fully-charged microbial supercapacitor, can be modeled using these rate constants, therefore the total current collected at the anode can be modeled to be the sum of individual current components (see Materials and Methods Section). The total current assumes that reaction kinetics at the anode are the fastest and the kinetics of acetate turnover are the slowest. For the initial biofilm, we have k_{int} ($=1.12\times10^{2} \pm 1.3\ s^{-1}$) >> $k_{erc}Erc_{total,i}$ ($=32.75 \pm 0.5\ s^{-1}$) >> $k_{mic}Erc_{total}$ ($=4.81 \pm 2\times10^{-2}\ s^{-1}$) >> k_{ac} ($=6.39\times10^{-1} \pm 2\times10^{-3}\ s^{-1}$). For the fully-grown biofilm, we have k_{int} ($=3.65\times10^{1} \pm 2\times10^{-1}\ s^{-1}$) >> $k_{erc}Erc_{total,i}$ ($=2.76 \pm 1\times10^{-2}\ s^{-1}$) >> $k_{mic}Erc_{total} + k_{ac}$ ($=0.11 \pm 8\times10^{-7}\ s^{-1}$) (here $k_{mic}Erc_{total}$ ($=0.0466 \pm 8\times10^{-7}\ s^{-1}$) is slightly smaller than k_{ac} ($=0.066\ s^{-1}$)). Note that k_{int} and k_{ac} are 1st order where as k_{erc} and k_{mic} are 2nd order reaction rate constants. The kinetic data, first of all, show that kinetic rates of initial biofilm are significantly higher than those of fully-grown biofilm. All kinetic rate constants, k_{int}, k_{erc}, k_{mic}, and k_{ac}, of initial biofilm are higher than those of fully-grown biofilm. The kinetic data also suggests that the slowest step in initial biofilm is the acetate turnover stage, whereas for fully-grown biofilm, acetate turnover and electron transfer from inside the bacteria to outer membrane cytochromes are rate-limiting.

Acetate turnover rate would be limited by the diffusion rate of NAD^+/NADH, in comparison to the other two electron-transferring steps in $Erc_{ox/red}$ and $Erc_{ox/red,i}$ bound to cell and outer membranes. The much slower rate of acetate turnover in fully-grown biofilm implies a substrate-diffusion limitation [214]. The high kinetic rate constants in initial over fully-grown biofilms are in agreement with prior art [153], which reported that for a thin biofilm, no significant hysteresis in *cytochrome* c oxidation was observed in cyclic voltammetry at a scan rate of 20 mV/s, whereas in a fully-grown biofilm, a significant lag existed at a scan rate of, rather low, 1 mV/s [153].

Besides the kinetic constants, it is informative on EET study to perform comparative analysis on the quantity of charges in initial and fully-grown biofilms. $Erc_{red,i,0}$, $Erc_{red,0}$, and Mic_{total} were extracted from the constants generated by fitting transient discharging curves (equation D.17). $Erc_{total,i}$ and Erc_{total} were, then, calculated concurrently. The redox cofactors inside exoelectrogen, Mic_{total}, of fully-grown biofilm is 4.20×10^{-2} C/cm^2, which is in agreement with prior art (5.67×10^{-2} C/cm^2) [201]. Mic_{total} dominates other charges, $Erc_{total,i}$ and Erc_{total}, in both initial and fully-grown biofilms. Mic_{total} accounts for 75% and more than 99% of overall charges for initial and fully-grown biofilms, respectively, in accordance with prior study [201].

$Erc_{red,i}$ in fully-grown biofilm is 3.1 times of that in initial biofilm, suggesting the biofilm-electrode interface for fully-grown biofilm is denser than that of initial biofilm. Erc_{total} in fully-grown biofilm is 6.4 times of that in initial biofilm, while Mic_{total} in fully-grown biofilm is 202 times of that in initial biofilm.

The total redox cofactors in fully-grown biofilm is 152 fold of that in initial biofilm, yet the total current density of fully-grown biofilm is merely 6 times of that of initial biofilm, which suggests that the participation of redox cofactors in the current of fully-grown biofilm is substantially less than that of initial biofilm. This implies that a finite limitation in electron transfer capability exists in fully-grown biofilm, in agreement with the slower reaction kinetics discussed above, and also in agreement with prior arts [132, 153, 154, 160].

The total charges contributing the discharging current were calculated by integrating discharging current over time. The total charges during the discharging are $3.17\times10^{-4} \pm 7\times10^{-5}$ and $2.65\times10^{-3} \pm 2\times10^{-5}$ C/cm^2, for initial and fully-grown biofilms, respectively. The total charges of initial biofilm are very close to the sum of redox cofactors calculated from the fitting analysis, $2.76\times10^{-4} \pm 5\times10^{-7}$ C/cm^2. However, the calculated charges, via integrating discharging current over time, of fully-grown biofilm is far less than, by a factor of 16, the sum of redox cofactors calculated from the fitting analysis, 4.20×10^{-2} C/cm^2. This distinct difference between initial and fully-grown biofilms implies that almost all redox cofactors in the initial biofilm contribute to the discharging current whereas a very small portion of redox cofactors inside the fully-grown biofilm participate in the discharging current, i.e. inactive redox cofactors related to EET are present in fully-grown biofilm. Not all redox cofactors located on the other side, away from the anode, would contribute to EET significantly in a fully-grown biofilm [132, 153, 160] whereas exoelectrogen close to the anode would not be active due to high pH or substrate depletion [63, 64].

The amount of *cytochrom*e c inside biofilm was quantified by UV-Vis spectrum analysis. The absorption spectrum for both initial and fully-grown biofilms are shown in Figure 7.5(c) to quantify the amount of heme in *cytochrome* c. The amounts of heme in *cytochrome* c are 0.4 ± 0.012 and 7.625 ± 0.025 nMole/cm^2, respectively, for initial and fully-grown biofilms. The amount of heme in *cytochrome* c for fully-grown biofilm is comparable with the previous report by Malvankar *et al*. [195]. From the amounts of heme in *cytochrome* c we can deduce the storable charges with *cytochrome* c as, $3.88\times10^{-5} \pm 1\times10^{-6}$ and $7.36\times10^{-4} \pm 2\times10^{-6}$ C/cm^2, for initial and fully-grown biofilms, respectively. The number of charges that can be stored in *cytochrome* c are significantly less than the total charges obtained by integrating discharging current over time. The storable charges accounts for only 12% and 28% of the total charges associated with initial and fully-grown biofilms during discharging, respectively, suggesting redox cofactors other than *cytochrome* c should be present for EET, such as membrane-bound and periplasmic cofactors, which concurs with prior art [154, 194]. More notably the storable charges are merely 14% and 1.7% of the sum of available redox cofactors, for initial and fully-grown biofilms, respectively. This finding supports that *cytochrome* c may not be the dominant charge storage unit, regardless of initial or fully-grown stage biofilms, and other charge storage molecules besides *cytochrome* c exist.

CHAPTER 8

CONCLUDING REMARKS

The current and power densities of previously reported MFCs are low compared with conventional power sources and converters. The work described herein has focused on enhancing the performance of MFCs, especially the current and power densities.

In the first chapter of the dissertation, an overview of the MFC background, operation principle, bacteria and extracellular electron transfer for MFC. The applications and a brief literature review of the state of art for MFCs are also included.

In the second chapter of the dissertation, the impact of scaling effect on the performance of MFCs are analyzed, based on the viewpoint of both mass transfer and internal resistance. By scaling down the characteristic length of MFCs, both the surface-area-to-volume ratio (SAV) and the mass transfer coefficient increases, which results in a higher current and power density. The promises and challenges of scaling down MFCs are also discussed.

In the third chapter of the dissertation, a miniaturized MFC with a small characteristic length is presented, based on the analysis of scaling effect on MFCs. Together with improved mass transfer due to increased flow rate, the miniaturized MFC achieve a high areal and volumetric power densities of 0.83 W/m^2 and 3,300 W/m^3. Thin film gold is used for both anode and cathode. Furthermore, the measured Coulombic efficiency (CE) was at least 79%, which is 2.5-fold greater than the previously reported maximum CE in micro-scale MFCs. The ability to improve these performance metrics may make micro-scale MFCs attractive for supplying power in sub-100 μW applications.

In the fourth chapter of the dissertation, the effect of using anode materials with high surface area to volume ratio is investigated. Three types of CNT-based anodes with different morphology and sheet resistance, VACNT, RACNT, and SSLbL CNT, along with a bare gold control were evaluated using miniaturized MFCs. Morphology and thickness of biofilm, and current/power generation capability of different anodes were characterized by SEM and polarization curves of miniaturized MFCs having these anodes. All CNT-based anodes form thicker biofilms than the bare gold anode control, with the low-sheet-resistance SSLbL CNT anode having the thickest biofilm of 10 μm and a current/power density of 2.59 A/m^2 and 0.83 W/m^2. Additionally, a coulombic efficiency of 60%-80% is achieved. This research may offer potential to provide guidance to future MFC research with 2D and 3D nanostructured electrode.

In the fifth chapter of the dissertation, a three dimensional graphene scaffold anode is implemented in the miniaturized MFC to further improve the performance. By implementing the three dimensional graphene scaffold anode, the two bottlenecks that limit the performance of MFCs - i) ineffective electron transfer from microbes located far from the anode and ii) an insufficient buffer supply to the biofilm – are successfully mitigated, and thus the highest power density to date of 11,220 Wm^{-3} has been recorded, a more than 3 fold increase over the highest value reported in all previous studies. The high volumetric power density is comparable with commercially available power sources, such as lead-acid batteries, nickel-cadmium batteries, and lithium ion batteries, which makes it a promising candidate as a carbon-neutral, renewable power source.

In the sixth chapter of the dissertation, the effect of enhanced mass transfer by an ultramicroelectrode(UME) anode is studied. A concentric ring-shape UME, width of 20 μm, is investigated to facilitate the diffusion of ions at the vicinity of micro-organisms that form their biofilm on the UME. The biofilm extends approximately 15 μm from the edge of the UME, suggesting the effective biofilm area increases. Measured current/power densities per the effective area and the original anode area are 7.08 ± 0.01 A/m^2 & 3.09 ± 0.04 W/m^2 and 17.7 ± 0.03 A/m^2 & 7.72 ± 0.09 W/m^2, respectively, substantially higher than any prior work in micro-scale MFCs, and very close, or even higher, to that of macro-scale MFCs. Coulombic efficiency (CE), a measure of how efficiently a MFC harvest electrons from micro-organisms, of 70 % and energy conversion efficiencies of 17 % are marked.

In the seventh chapter of the dissertation, a novel bio-inspired microbial supercapacitor based on regulating the respiration of bacteria. The microbial supercapacitor operates by utilizing unique pseudocapacitance formed by exoelectrogen, a specific species of microbe named Geobacter spp. which is able to transfer electrons outside its outer membrane during respiration. Charging and discharging operations were performed by regulating the respiration of the exoelectrogen. Remarkable performance is demonstrated, including (1) high maximum current and power densities of 531.2A/m^2 / 1,060,000A/m^3 and 197.5W/m^2 / 395,000W/m^3, respectively, which are 1-2 orders of magnitude higher than previously reported other microbial electrochemical techniques; (2) high cycle stability of over 1 million; (3) high specific capacitance of 17.85±0.91 mF/cm2, which is 4.4 fold to 2 orders of magnitude higher than any previously reported supercapacitors having graphene-based electrodes. The microbial supercapacitor was also implemented to study the extracellular electron transfer (EET) process by non-linearly fitting the discharging profile, through which critical quantitative kinetics information to fully understand EET and determining the rate-limiting EET mechanism was obtained.

This cumulated work has demonstrated that a maximum current and power density of 31,020 Am^{-3} and 11,220 Wm^{-3} is presented by the MFC, and a maximum current and power density of 1,060,000 A/m^3 and 395,000 W/m^3 is presented by the microbial supercapacitor. A comparison of the performance of the MFCs in this dissertation with prior MFCs is shown in Figure 8.1. The performance are comparable or better than conventional power sources/converters, as shown in Figure 5.4. As a result, there is plenty of room for MFC and microbial supercapacitor research. We believe MFC will be an important power source/converter for biomass utilization in the near future through painstaking research all over the world.

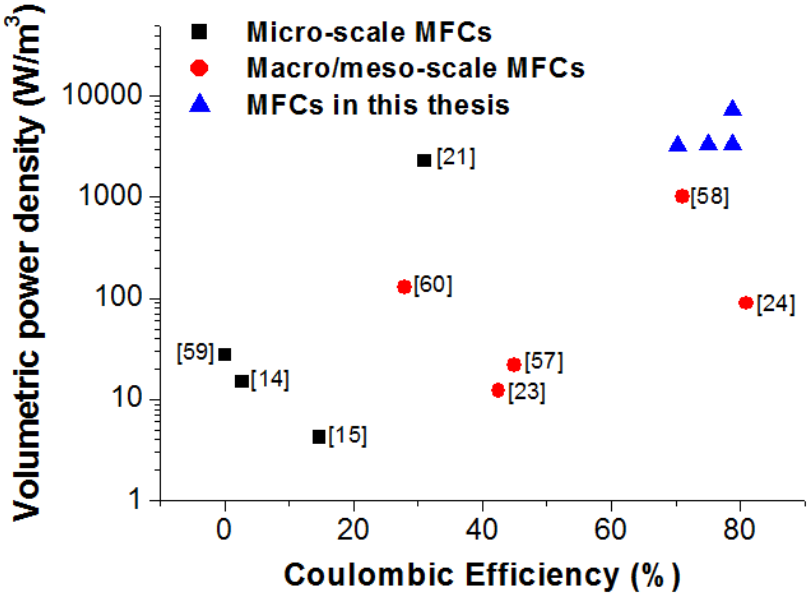

Figure 8.1. A comparison of areal power density and CE of this dissertation with those of existing macroscale, mesoscale and microscale MFCs.

REFERENCES

1. Sorrell S, Speirs J, Bentley R, Brandt A, Miller R. *Global oil depletion-an assessment of the evidence for a near-term peak in global oil production* (2009).

2. Bentley RW. Global oil & gas depletion: an overview. *Energy policy* **30**, 189-205 (2002).

3. Faaij AP. Bio-energy in Europe: changing technology choices. *Energy policy* **34**, 322-342 (2006).

4. Rodrigo M, Canizares P, Lobato J, Paz R, Sáez C, Linares J. Production of electricity from the treatment of urban waste water using a microbial fuel cell. *Journal of Power Sources* **169**, 198-204 (2007).

5. REN21 PS. *Renewables 2011 global status report*. REN21 Secretariat Paris, France (2011).

6. Cheng S, Xing D, Logan BE. Electricity generation of single-chamber microbial fuel cells at low temperatures. *Biosensors and Bioelectronics* **26**, 1913-1917 (2011).

7. Rabaey K, Verstraete W. Microbial fuel cells: novel biotechnology for energy generation. *Trends in biotechnology* **23**, 291-298 (2005).

8. Huang L, Cheng S, Rezaei F, Logan BE. Reducing organic loads in wastewater effluents from paper recycling plants using microbial fuel cells. *Environmental technology* **30**, 499-504 (2009).

9. Clauwaert P, Verstraete W. Methanogenesis in membraneless microbial electrolysis cells. *Applied microbiology and biotechnology* **82**, 829-836 (2009).

10. Kim JR, Dec J, Bruns MA, Logan BE. Removal of odors from swine wastewater by using microbial fuel cells. *Applied and environmental microbiology* **74**, 2540-2543 (2008).

11. Morris JM, Jin S. Feasibility of using microbial fuel cell technology for bioremediation of hydrocarbons in groundwater. *Journal of Environmental Science and Health, Part A* **43**, 18-23 (2007).

12. Catal T, Fan Y, Li K, Bermek H, Liu H. Effects of furan derivatives and phenolic compounds on electricity generation in microbial fuel cells. *Journal of Power Sources* **180**, 162-166 (2008).

13. Tender LM*, et al.* The first demonstration of a microbial fuel cell as a viable power supply: powering a meteorological buoy. *Journal of Power Sources* **179**, 571-575 (2008).

14. Cooke KG, Gay MO, Radachowsky SE, Guzman JJ, Chiu MA. BackyardNetTM: distributed sensor network powered by terrestrial microbial fuel cell technology. In: *SPIE Defense, Security, and Sensing* (ed^(eds). International Society for Optics and Photonics (2010).

15. Guzman JJ, Cooke KG, Gay MO, Radachowsky SE, Girguis PR, Chiu MA. Benthic microbial fuel cells: Long-term power sources for wireless marine sensor networks. In: *SPIE Defense, Security, and Sensing*. International Society for Optics and Photonics (2010).

16. Dyer CK. Fuel cells for portable applications. *Journal of Power Sources* **106**, 31-34 (2002).

17. Drews J, Fehrmann G, Staub R, Wolf R. Primary batteries for implantable pacemakers and defibrillators. *Journal of power sources* **97**, 747-749 (2001).

18. Moghaddam S*, et al.* An inorganic–organic proton exchange membrane for fuel cells with a controlled nanoscale pore structure. *Nature nanotechnology* **5**, 230-236 (2010).

19. Debabov V. Electricity from microorganisms. *Microbiology* **77**, 123-131 (2008).

20. Tender LM*, et al.* The first demonstration of a microbial fuel cell as a viable power supply: powering a meteorological buoy. *Journal of Power Sources* **179**, 571-575 (2008).

21. Wilkinson S. "Gastrobots"—Benefits and Challenges of Microbial Fuel Cells in FoodPowered Robot Applications. *Autonomous Robots* **9**, 99-111 (2000).

22. Ieropoulos I, Melhuish C, Greenman J. Artificial gills for robots: MFC behaviour in water. *Bioinspiration & biomimetics* **2**, S83 (2007).

23. Ieropoulos I, Melhuish C, Greenman J, Horsfield I. EcoBot-II: An artificial agent with a natural metabolism. *Journal of Advanced Robotic Systems* **2**, 295-300 (2005).

24. Han Y, Yu C, Liu H. A microbial fuel cell as power supply for implantable medical devices. *Biosensors and Bioelectronics* **25**, 2156-2160 (2010).

25. Siu CPB, Chiao M. A microfabricated PDMS microbial fuel cell. *Microelectromechanical Systems, Journal of* **17**, 1329-1341 (2008).

26. Sun M*, et al.* Passing data and supplying power to neural implants. *IEEE Engineering in medicine and biology magazine* **25**, 39-46 (2006).

27. Li Z, Rosenbaum MA, Venkataraman A, Tam TK, Katz E, Angenent LT. Bacteria-based AND logic gate: a decision-making and self-powered biosensor. *Chemical Communications* **47**, 3060-3062 (2011).

28. Davila D, Esquivel J, Sabate N, Mas J. Silicon-based microfabricated microbial fuel cell toxicity sensor. *Biosensors and Bioelectronics* **26**, 2426-2430 (2011).

29. Logan BE. Scaling up microbial fuel cells and other bioelectrochemical systems. *Applied microbiology and biotechnology* **85**, 1665-1671 (2010).

30. Fan Y, Sharbrough E, Liu H. Quantification of the internal resistance distribution of microbial fuel cells. *Environmental science & technology* **42**, 8101-8107 (2008).

31. Fan Y, Hu H, Liu H. Enhanced Coulombic efficiency and power density of air-cathode microbial fuel cells with an improved cell configuration. *Journal of Power Sources* **171**, 348-354 (2007).

32. Ringeisen BR*, et al.* High power density from a miniature microbial fuel cell using Shewanella oneidensis DSP10. *Environmental Science & Technology* **40**, 2629-2634 (2006).

33. Chae J, Kulah H, Najafi K. A monolithic three-axis micro-g micromachined silicon capacitive accelerometer. *Microelectromechanical Systems, Journal of* **14**, 235-242 (2005).

34. Je S-S, Chae J. A compact, low-power, and electromagnetically actuated microspeaker for hearing aids. *Electron Device Letters, IEEE* **29**, 856-858 (2008).

35. Ren H, Tao F, Wang W, Yao J. An out-of-plane electrostatic actuator based on the lever principle. *Journal of Micromechanics and Microengineering* **21**, 045019 (2011).

36. Chiao M, Lam KB, Su Y, Lin L. A MINIATURIZED MICROBIAL FUEL CELL. In: *Solid-State Sensor, Actuator and Microsystems Workshop* (ed^(eds) (2002).

37. Bond DR, Holmes DE, Tender LM, Lovley DR. Electrode-reducing microorganisms that harvest energy from marine sediments. *Science* **295**, 483-485 (2002).

38. Chiao M, Lam KB, Lin L. Micromachined microbial and photosynthetic fuel cells. *Journal of Micromechanics and Microengineering* **16**, 2547 (2006).

39. Qian F, Baum M, Gu Q, Morse DE. A 1.5 uL microbial fuel cell for on-chip bioelectricity generation. *Lab on a Chip* **9**, 3076-3081 (2009).

40. Qian F, He Z, Thelen MP, Li Y. A microfluidic microbial fuel cell fabricated by soft lithography. *Bioresource Technol* **102**, 5836-5840 (2011).

41. Parra E, Lin L. Microbial fuel cell based on electrode-exoelectrogenic bacteria interface. In: *Micro Electro Mechanical Systems, 2009. MEMS 2009. IEEE 22nd International Conference on*. IEEE (2009).

42. Inoue S. Structural optimization of contact electrodes in microbial fuel cells for current density enhancements. *Sensors and Actuators A-Physical* **177**, 7 (2012).

43. Choi S*, et al.* A mu L-scale micromachined microbial fuel cell having high power density. *Lab on a Chip* **11**, 1110-1117 (2011).

44. Choi S, Chae J. An array of microliter-sized microbial fuel cells generating 100 µW of power. *Sensors and Actuators A: Physical* **177**, 10-15 (2012).

45. Hou H, Li L, Cho Y, de Figueiredo P, Han A. Microfabricated microbial fuel cell arrays reveal electrochemically active microbes. *PLoS One* **4**, e6570 (2009).

46. Rittmann BE, McCarty PL. *Environmental biotechnology*. McGraw Hill New York (2001).

47. Pocaznoi D, Erable B, Delia M-L, Bergel A. Ultra microelectrodes increase the current density provided by electroactive biofilms by improving their electron transport ability. *Energy & Environmental Science* **5**, 5287-5296 (2012).

48. Kim JR, Cheng S, Oh S-E, Logan BE. Power generation using different cation, anion, and ultrafiltration membranes in microbial fuel cells. *Environmental science & technology* **41**, 1004-1009 (2007).

49. Baughman RH, Zakhidov AA, de Heer WA. Carbon nanotubes--the route toward applications. *Science* **297**, 787-792 (2002).

50. Qiao Y, Li CM, Bao SJ, Bao QL. Carbon nanotube/polyaniline composite as anode material for microbial fuel cells. *Journal of Power Sources* **170**, 79-84 (2007).

51. Peng L, You SJ, Wang JY. Carbon nanotubes as electrode modifier promoting direct electron transfer from Shewanella oneidensis. *Biosensors & Bioelectronics* **25**, 1248-1251 (2010).

52. Tsai HY, Wu CC, Lee CY, Shih EP. Microbial fuel cell performance of multiwall carbon nanotubes on carbon cloth as electrodes. *Journal of Power Sources* **194**, 199-205 (2009).

53. Chaudhuri SK, Lovley DR. Electricity generation by direct oxidation of glucose in mediatorless microbial fuel cells. *Nat Biotechnol* **21**, 1229-1232 (2003).

54. Logan BE*, et al.* Microbial fuel cells: Methodology and technology. *Environ Sci Technol* **40**, 5181-5192 (2006).

55. Morris JM, Jin S. Feasibility of using microbial fuel cell technology for bioremediation of hydrocarbons in groundwater. *J Environ Sci Heal A* **43**, 18-23 (2008).

56. Ren H, Lee H-S, Chae J. Miniaturizing microbial fuel cells for potential portable power sources: promises and challenges. *Microfluidics and Nanofluidics* **13**, 353-381 (2012).

57. Lee S, Nam G-J, Chae J, Kim H, Drake AJ. Two-dimensional position detection system with MEMS accelerometer for mouse applications. In: *Design Automation Conference, 2001. Proceedings* of IEEE (2001).

58. Welch WC, Chae J, Najafi K. Transfer of metal MEMS packages using a wafer-level solder transfer technique. *Ieee T Adv Packaging* **28**, 643-649 (2005).

59. Yang Y, Chae J. Miniaturized protein separation using a liquid chromatography column on a flexible substrate. *Journal of Micromechanics and Microengineering* **18**, (2008).

60. Choi S, Chae J. Reusable biosensors via in situ electrochemical surface regeneration in microfluidic applications. *Biosensors & Bioelectronics* **25**, 527-531 (2009).

61. Choi S, Chae J. Optimal biofilm formation and power generation in a micro-sized microbial fuel cell (MFC). *Sensors and Actuators A: Physical*.

62. Fan YZ, Sharbrough E, Liu H. Quantification of the Internal Resistance Distribution of Microbial Fuel Cells. *Environ Sci Technol* **42**, 8101-8107 (2008).

63. Torres CI, Kato Marcus A, Rittmann BE. Proton transport inside the biofilm limits electrical current generation by anode-respiring bacteria. *Biotechnology and Bioengineering* **100**, 872-881 (2008).

64. Franks AE, Nevin KP, Jia H, Izallalen M, Woodard TL, Lovley DR. Novel strategy for three-dimensional real-time imaging of microbial fuel cell communities: monitoring the inhibitory effects of proton accumulation within the anode biofilm. *Energy & Environmental Science* **2**, 113-119 (2009).

65. Gerlach G, Dotzel W. *Introduction to microsystem technology: a guide for students*. Wiley (2008).

66. Qian F, Morse DE. Miniaturizing microbial fuel cells. *Trends Biotechnol* **29**, 62-69 (2011).

67. Stone HA, Stroock AD, Ajdari A. Engineering flows in small devices. *Annu Rev Fluid Mech* **36**, 381-411 (2004).

68. Sherwood TK, Pigford RL, Wilke CR. *Mass transfer*. McGraw-Hill (1975).

69. Torres CsI*, et al.* Selecting anode-respiring bacteria based on anode potential: phylogenetic, electrochemical, and microscopic characterization. *Environmental science & technology* **43**, 9519-9524 (2009).

70. Lee H-S, Rittmann BE. Significance of biological hydrogen oxidation in a continuous single-chamber microbial electrolysis cell. *Environmental science & technology* **44**, 948-954 (2009).

71. Parameswaran P, Torres CI, Kang D-W, Rittmann BE, Krajmalnik-Brown R. The role of homoacetogenic bacteria as efficient hydrogen scavengers in microbial electrochemical cells (MXCs). *Water Science & Technology* **65**, (2012).

72. Renslow R, Babauta J, Majors P, Beyenal H. Diffusion in biofilms respiring on electrodes. *Energy & environmental science* **6**, 595-607 (2013).

73. Torres CI, Kato Marcus A, Rittmann BE. Proton transport inside the biofilm limits electrical current generation by anode-respiring bacteria. *Biotechnology and bioengineering* **100**, 872-881 (2008).

74. Torres CI, Marcus AK, Rittmann BE. Proton transport inside the biofilm limits electrical current generation by anode-respiring bacteria. *Biotechnol Bioeng* **100**, 872-881 (2008).

75. Rabaey K, Boon N, Siciliano SD, Verhaege M, Verstraete W. Biofuel cells select for microbial consortia that self-mediate electron transfer. *Appl Environ Microb* **70**, 5373-5382 (2004).

76. Siu CPB, Chiao M. A Microfabricated PDMS Microbial Fuel Cell. *J Microelectromech S* **17**, 1329-1341 (2008).

77. Qian F, Baum M, Gu Q, Morse DE. A 1.5 mu L microbial fuel cell for on-chip bioelectricity generation. *Lab Chip* **9**, 3076-3081 (2009).

78. Chiao M, Lam KB, Lin LW. Micromachined microbial and photosynthetic fuel cells. *J Micromech Microeng* **16**, 2547-2553 (2006).

79. Fan YZ, Hu HQ, Liu H. Enhanced Coulombic efficiency and power density of air-cathode microbial fuel cells with an improved cell configuration. *J Power Sources* **171**, 348-354 (2007).

80. Liu H, Cheng S, Huang LP, Logan BE. Scale-Lip of membrane-free single-chamber microbial fuel cells. *J Power Sources* **179**, 274-279 (2008).

81. Liu H, Logan BE. Electricity Generation Using an Air-Cathode Single Chamber Microbial Fuel Cell in the Presence and Absence of a Proton Exchange Membrane. *Environmental Science & Technology* **38**, 4040-4046 (2004).

82. Fan Y, Han S-K, Liu H. Improved performance of CEA microbial fuel cells with increased reactor size. *Energy & Environmental Science* **5**, 8273-8280 (2012).

83. Himmel ME*, et al.* Biomass recalcitrance: engineering plants and enzymes for biofuels production. *Science* **315**, 804-807 (2007).

84. Ragauskas AJ*, et al.* The path forward for biofuels and biomaterials. *Science* **311**, 484-489 (2006).

85. Logan BE, Rabaey K. Conversion of wastes into bioelectricity and chemicals by using microbial electrochemical technologies. *Science* **337**, 686-690 (2012).

86. Logan BE*, et al.* Microbial Fuel Cells: Methodology and Technology†. *Environmental Science & Technology* **40**, 5181-5192 (2006).

87. ElMekawy A, Srikanth S, Vanbroekhoven K, De Wever H, Pant D. Bioelectro-catalytic valorization of dark fermentation effluents by acetate oxidizing bacteria in bioelectrochemical system (BES). *Journal of Power Sources* **262**, 183-191 (2014).

88. Pant D*, et al.* Integrated conversion of food waste diluted with sewage into volatile fatty acids through fermentation and electricity through a fuel cell. *Environmental technology* **34**, 1935-1945 (2013).

89. Gregory KB, Lovley DR. Remediation and recovery of uranium from contaminated subsurface environments with electrodes. *Environmental Science & Technology* **39**, 8943-8947 (2005).

90. Lu L, Huggins T, Jin S, Zuo Y, Ren ZJ. Microbial Metabolism and Community Structure in Response to Bioelectrochemically Enhanced Remediation of Petroleum Hydrocarbon-Contaminated Soil. *Environmental science & technology* **48**, 4021-4029 (2014).

91. Logan B. *Microbial fuel cells*. John Wiley & Sons, Inc. (2008).

92. Rabaey K, Boon N, Siciliano SD, Verhaege M, Verstraete W. Biofuel Cells Select for Microbial Consortia That Self-Mediate Electron Transfer. *Applied and Environmental Microbiology* **70**, 5373-5382 (2004).

93. He Z, Minteer SD, Angenent LT. Electricity generation from artificial wastewater using an upflow microbial fuel cell. *Environmental Science & Technology* **39**, 5262-5267 (2005).

94. Rosenbaum M, Zhao F, Schroder U, Scholz F. Interfacing electrocatalysis and biocatalysis with tungsten carbide: A high-performance, noble-metal-free microbial fuel cell. *Angew Chem Int Edit* **45**, 6658-6661 (2006).

95. Lee SW*, et al.* High-power lithium batteries from functionalized carbon-nanotube electrodes. *Nat Nanotechnol* **5**, 531-537 (2010).

96. Taylor AD, Michel M, Sekol RC, Kizuka JM, Kotov NA, Thompson LT. Fuel Cell Membrane Electrode Assemblies Fabricated by Layer-by-Layer Electrostatic Self-Assembly Techniques. *Advanced Functional Materials* **18**, 3003-3009 (2008).

97. Geim AK, Novoselov KS. The rise of graphene. *Nature materials* **6**, 183-191 (2007).

98. Xie X, Yu GH, Liu N, Bao ZN, Criddle CS, Cui Y. Graphene-sponges as high-performance low-cost anodes for microbial fuel cells. *Energy & Environmental Science* **5**, 6862-6866 (2012).

99. Xiao L, Damien J, Luo J, Jang HD, Huang J, He Z. Crumpled graphene particles for microbial fuel cell electrodes. *Journal of Power Sources* **208**, 187-192 (2012).

100. Liu X-W, Sun X-F, Huang Y-X, Sheng G-P, Wang S-G, Yu H-Q. Carbon nanotube/chitosan nanocomposite as a biocompatible biocathode material to enhance the electricity generation of a microbial fuel cell. *Energy & Environmental Science* **4**, 1422-1427 (2011).

101. Mink JE, Hussain MM. Sustainable design of high-performance microsized microbial fuel cell with carbon nanotube anode and air cathode. *ACS nano* **7**, 6921-6927 (2013).

102. Mehdinia A, Ziaei E, Jabbari A. Multi-walled carbon nanotube/SnO2 nanocomposite: a novel anode material for microbial fuel cells. *Electrochimica Acta* **130**, 512-518 (2014).

103. Yong Y-C, Dong X-C, Chan-Park MB, Song H, Chen P. Macroporous and monolithic anode based on polyaniline hybridized three-dimensional graphene for high-performance microbial fuel cells. *ACS nano* **6**, 2394-2400 (2012).

104. He Z, Liu J, Qiao Y, Li CM, Tan TTY. Architecture engineering of hierarchically porous chitosan/vacuum-stripped graphene scaffold as bioanode for high performance microbial fuel cell. *Nano letters* **12**, 4738-4741 (2012).

105. Wang H*, et al.* High power density microbial fuel cell with flexible 3D graphene–nickel foam as anode. *Nanoscale* **5**, 10283-10290 (2013).

106. Qiao Y, Wu X-S, Ma C-X, He H, Li CM. A hierarchical porous graphene/nickel anode that simultaneously boosts the bio-and electro-catalysis for high-performance microbial fuel cells. *RSC Advances* **4**, 21788-21793 (2014).

107. Chou H-T, Lee H-J, Lee C-Y, Tai N-H, Chang H-Y. Highly durable anodes of microbial fuel cells using a reduced graphene oxide/carbon nanotube-coated scaffold. *Bioresource Technol* **169**, 532-536 (2014).

108. Mink JE, Rojas JP, Logan BE, Hussain MM. Vertically grown multiwalled carbon nanotube anode and nickel silicide integrated high performance microsized (1.25 muL) microbial fuel cell. *Nano Lett* **12**, 791-795 (2012).

109. Smart SK, Cassady AI, Lu GQ, Martin DJ. The biocompatibility of carbon nanotubes. *Carbon* **44**, 1034-1047 (2006).

110. Sharma T, Reddy ALM, Chandra TS, Ramaprabhu S. Development of carbon nanotubes and nanofluids based microbial fuel cell. *Int J Hydrogen Energ* **33**, 6749-6754 (2008).

111. Wang H*, et al.* Carbon nanotube modified air-cathodes for electricity production in microbial fuel cells. *Journal of Power Sources* **196**, 7465-7469 (2011).

112. Khilari S, Pandit S, Ghangrekar M, Das D, Pradhan D. Graphene supported α-MnO 2 nanotubes as a cathode catalyst for improved power generation

and wastewater treatment in single-chambered microbial fuel cells. *RSC Advances* **3**, 7902-7911 (2013).

113. Richter H, McCarthy K, Nevin KP, Johnson JP, Rotello VM, Lovley DR. Electricity generation by Geobacter sulfurreducens attached to gold electrodes. *Langmuir* **24**, 4376-4379 (2008).

114. Ren ZF*, et al.* Synthesis of large arrays of well-aligned carbon nanotubes on glass. *Science* **282**, 1105-1107 (1998).

115. Choi KS, Cho YS, Hong SY, Park JB, Kim DJ. Effects of ammonia on the alignment of carbon nanotubes in metal-assisted thermal chemical vapor deposition. *J Eur Ceram Soc* **21**, 2095-2098 (2001).

116. Gittleson FS, Kohn DJ, Li X, Taylor AD. Improving the assembly speed, quality, and tunability of thin conductive multilayers. *ACS Nano* **6**, 3703-3711 (2012).

117. Parameswaran P, Torres CI, Lee HS, Krajmalnik-Brown R, Rittmann BE. Syntrophic interactions among anode respiring bacteria (ARB) and Non-ARB in a biofilm anode: electron balances. *Biotechnology and bioengineering* **103**, 513-523 (2009).

118. Oh S, Daraio C, Chen LH, Pisanic TR, Finones RR, Jin S. Significantly accelerated osteoblast cell growth on aligned TiO2 nanotubes. *Journal of Biomedical Materials Research Part A* **78**, 97-103 (2006).

119. Kim D-H, Provenzano PP, Smith CL, Levchenko A. Matrix nanotopography as a regulator of cell function. *The Journal of cell biology* **197**, 351-360 (2012).

120. Ren Z, Ramasamy RP, Cloud-Owen SR, Yan H, Mench MM, Regan JM. Time-course correlation of biofilm properties and electrochemical performance in single-chamber microbial fuel cells. *Bioresource Technol* **102**, 416-421 (2011).

121. Bond DR, Lovley DR. Electricity production by Geobacter sulfurreducens attached to electrodes. *Applied and environmental microbiology* **69**, 1548-1555 (2003).

122. Kim HJ, Park HS, Hyun MS, Chang IS, Kim M, Kim BH. A mediator-less microbial fuel cell using a metal reducing bacterium, Shewanella putrefaciens. *Enzyme and Microbial Technology* **30**, 145-152 (2002).

123. Zurita–Gotor M, Gittleson FS, Taylor AD, Blawzdziewicz J. Stratified rod network model of electrical conductance in ultrathin polymer–carbon nanotube multilayers. *Physical Review B* **87**, 195449 (2013).

124. Tan JL, Tien J, Pirone DM, Gray DS, Bhadriraju K, Chen CS. Cells lying on a bed of microneedles: an approach to isolate mechanical force. *Proceedings of the National Academy of Sciences* **100**, 1484-1489 (2003).

125. Ren Z, Yan H, Wang W, Mench MM, Regan JM. Characterization of microbial fuel cells at microbially and electrochemically meaningful time scales. *Environmental science & technology* **45**, 2435-2441 (2011).

126. Lyon DY, Buret F, Vogel TM, Monier J-M. Is resistance futile? Changing external resistance does not improve microbial fuel cell performance. *Bioelectrochemistry* **78**, 2-7 (2010).

127. McLean JS*, et al.* Quantification of electron transfer rates to a solid phase electron acceptor through the stages of biofilm formation from single cells to multicellular communities. *Environmental science & technology* **44**, 2721-2727 (2010).

128. Logan BE*, et al.* Microbial fuel cells: methodology and technology. *Environmental science & technology* **40**, 5181-5192 (2006).

129. Aelterman P, Verstraete W. Bioanode performance in bioelectrochemical systems: recent improvements and prospects. *Trends in biotechnology* **27**, 168-178 (2009).

130. Clauwaert P, Aelterman P, De Schamphelaire L, Carballa M, Rabaey K, Verstraete W. Minimizing losses in bio-electrochemical systems: the road to applications. *Applied Microbiology and Biotechnology* **79**, 901-913 (2008).

131. ElMekawy A, Hegab HM, Dominguez-Benetton X, Pant D. Internal resistance of microfluidic microbial fuel cell: challenges and potential opportunities. *Bioresource Technol* **142**, 672-682 (2013).

132. Bond DR, Strycharz-Glaven SM, Tender LM, Torres CI. On Electron Transport through Geobacter Biofilms. *ChemSusChem* **5**, 1099-1105 (2012).

133. Biffinger JC, Ray R, Little B, Ringeisen BR. Diversifying Biological Fuel Cell Designs by Use of Nanoporous Filters. *Environmental Science & Technology* **41**, 1444-1449 (2007).

134. Liu H, Cheng S, Huang L, Logan BE. Scale-up of membrane-free single-chamber microbial fuel cells. *Journal of Power Sources* **179**, 274-279 (2008).

135. Shimoyama T, Komukai S, Yamazawa A, Ueno Y, Logan BE, Watanabe K. Electricity generation from model organic wastewater in a cassette-electrode microbial fuel cell. *Applied microbiology and biotechnology* **80**, 325-330 (2008).

136. Stevens J. Optimized thermal design of small ΔT thermoelectric generators. (1999).

137. Roundy SJ. Energy scavenging for wireless sensor nodes with a focus on vibration to electricity conversion. (ed^(eds). University of California (2003).

138. Vullers R, van Schaijk R, Doms I, Van Hoof C, Mertens R. Micropower energy harvesting. *Solid-State Electronics* **53**, 684-693 (2009).

139. Seok M*, et al.* The Phoenix Processor: A 30pW platform for sensor applications. (ed^(eds). IEEE (2008).

140. Hempstead M, Tripathi N, Mauro P, Wei GY, Brooks D. An ultra low power system architecture for sensor network applications. IEEE (2005).

141. Pillai V, Heinrich H, Dieska D, Nikitin PV, Martinez R, Rao KVS. An ultra-low-power long range battery/passive RFID tag for UHF and microwave

bands with a current consumption of 700 nA at 1.5 V. *Circuits and Systems I: Regular Papers, IEEE Transactions on* **54**, 1500-1512 (2007).

142. Ren H, Tian H, Gardner CL, Ren T-L, Chae J. A miniaturized microbial fuel cell with three-dimensional graphene macroporous scaffold anode demonstrating a record power density of over 10000 W m^{-3}. *Nanoscale* **8**, 3539-3547 (2016).

143. McCarty PL, Bae J, Kim J. Domestic Wastewater Treatment as a Net Energy Producer–Can This be Achieved? *Environmental science & technology* **45**, 7100-7106 (2011).

144. Logan BE. Peer reviewed: extracting hydrogen and electricity from renewable resources. *Environmental science & technology* **38**, 160A-167A (2004).

145. Perlack RD, Wright LL, Turhollow AF, Graham RL, Stokes BJ, Erbach DC. Biomass as feedstock for a bioenergy and bioproducts industry: the technical feasibility of a billion-ton annual supply. DTIC Document (2005).

146. Pikul JH, Zhang HG, Cho J, Braun PV, King WP. High-power lithium ion microbatteries from interdigitated three-dimensional bicontinuous nanoporous electrodes. *Nature communications* **4**, 1732 (2013).

147. Wang ZL, Song J. Piezoelectric nanogenerators based on zinc oxide nanowire arrays. *Science* **312**, 242-246 (2006).

148. Heeger AJ. Semiconducting and metallic polymers: the fourth generation of polymeric materials (Nobel lecture). *Angewandte Chemie International Edition* **40**, 2591-2611 (2001).

149. Pech D*, et al.* Ultrahigh-power micrometre-sized supercapacitors based on onion-like carbon. *Nature nanotechnology* **5**, 651-654 (2010).

150. Ren H*, et al.* A high power density miniaturized microbial fuel cell having carbon nanotube anodes. *Journal of Power Sources* **273**, 823-830 (2015).

151. Ren H, Torres CI, Parameswaran P, Rittmann BE, Chae J. Improved Current and Power Density with a Micro-scale Microbial Fuel Cell Due to a Small Characteristic Length. *Biosensors and Bioelectronics*, (2014).

152. Malvankar NS, Tuominen MT, Lovley DR. Biofilm conductivity is a decisive variable for high-current-density Geobacter sulfurreducens microbial fuel cells. *Energy & Environmental Science* **5**, 5790-5797 (2012).

153. Liu Y, Bond DR. Long-Distance Electron Transfer by G. sulfurreducens Biofilms Results in Accumulation of Reduced c-Type Cytochromes. *ChemSusChem* **5**, 1047-1053 (2012).

154. Strycharz-Glaven SM, Tender LM. Study of the mechanism of catalytic activity of G. sulfurreducens biofilm anodes during biofilm growth. *ChemSusChem* **5**, 1106-1118 (2012).

155. Xie X*, et al.* Three-dimensional carbon nanotube− textile anode for high-performance microbial fuel cells. *Nano letters* **11**, 291-296 (2010).

156. Xie X, Yu G, Liu N, Bao Z, Criddle CS, Cui Y. Graphene–sponges as high-performance low-cost anodes for microbial fuel cells. *Energy & Environmental Science* **5**, 6862-6866 (2012).

157. Chen S*, et al.* Electrospun and solution blown three-dimensional carbon fiber nonwovens for application as electrodes in microbial fuel cells. *Energy & Environmental Science* **4**, 1417-1421 (2011).

158. Chen Z, Ren W, Gao L, Liu B, Pei S, Cheng H-M. Three-dimensional flexible and conductive interconnected graphene networks grown by chemical vapour deposition. *Nature materials* **10**, 424-428 (2011).

159. Li W, Tan C, Lowe MA, Abruna HD, Ralph DC. Electrochemistry of individual monolayer graphene sheets. *ACS nano* **5**, 2264-2270 (2011).

160. Bonanni PS, Bradley DF, Schrott GD, Busalmen JP. Limitations for Current Production in Geobacter sulfurreducens Biofilms. *ChemSusChem* **6**, 711-720 (2013).

161. Jiang X*, et al.* Probing single-to multi-cell level charge transport in Geobacter sulfurreducens DL-1. *Nature communications* **4**, (2013).

162. Jiang X*, et al.* Nanoparticle facilitated extracellular electron transfer in microbial fuel cells. *Nano letters* **14**, 6737-6742 (2014).

163. Lovley DR. The microbe electric: conversion of organic matter to electricity. *Current opinion in Biotechnology* **19**, 564-571 (2008).

164. Muller R, Gambini S, Rabaey JM. A 0.013, 5, DC-coupled neural signal acquisition IC with 0.5 V supply. *Solid-State Circuits, IEEE Journal of* **47**, 232-243 (2012).

165. Aelterman P, Rabaey K, Pham HT, Boon N, Verstraete W. Continuous electricity generation at high voltages and currents using stacked microbial fuel cells. *Environmental science & technology* **40**, 3388-3394 (2006).

166. Ledezma P, Stinchcombe A, Greenman J, Ieropoulos I. The first self-sustainable microbial fuel cell stack. *Physical Chemistry Chemical Physics* **15**, 2278-2281 (2013).

167. Holade Y*, et al.* Wireless Information Transmission System Powered by an Abiotic Biofuel Cell Implanted in an Orange. *Electroanalysis* **27**, 276-280 (2015).

168. Katz E. Implantable biofuel cells operating in vivo: Providing sustainable power for bioelectronic devices: From biofuel cells to cyborgs. In: *Advances in Sensors and Interfaces (IWASI), 2015 6th IEEE International Workshop on* (ed^(eds). IEEE (2015).

169. Taghavi M*, et al.* Self sufficient wireless transmitter powered by foot-pumped urine operating wearable MFC. *Bioinspiration & biomimetics* **11**, 016001 (2015).

170. Ren H, Chae J. SCALING EFFECT ON MEMS-BASED MICROBIAL FUEL CELLS TOWARD A CARBON-NEUTRAL MINIATURIZED POWER SOURCE. In: *IEEE Solid-State Sensors and Actuators Workshop* (ed^(eds) (2012).

171. Mu C, Kien BL, Liwei L. Micromachined microbial and photosynthetic fuel cells. *Journal of Micromechanics and Microengineering* **16**, 2547 (2006).

172. Jiang H, Halverson LJ, Dong L. A miniature microbial fuel cell with conducting nanofibers-based 3D porous biofilm. *Journal of Micromechanics and Microengineering* **25**, 125017 (2015).

173. Bard AJ, Faulkner LR. *Electrochemical methods: fundamentals and applications*. Wiley New York (1980).

174. Smirnov W*, et al.* Integrated All-Diamond Ultramicroelectrode Arrays: Optimization of Faradaic and Capacitive Currents. *Analytical Chemistry* **83**, 7438-7443 (2011).

175. Fletcher BL*, et al.* Effects of ultramicroelectrode dimensions on the electropolymerization of polypyrrole. *Journal of Applied Physics* **105**, 124312-124316 (2009).

176. Liu Y, Kim H, Franklin R, Bond DR. Gold line array electrodes increase substrate affinity and current density of electricity-producing G. sulfurreducens biofilms. *Energy & Environmental Science* **3**, 1782-1788 (2010).

177. Lee H-S, Parameswaran P, Kato-Marcus A, Torres CI, Rittmann BE. Evaluation of energy-conversion efficiencies in microbial fuel cells (MFCs) utilizing fermentable and non-fermentable substrates. *Water Research* **42**, 1501-1510 (2008).

178. Call D, Logan BE. Hydrogen production in a single chamber microbial electrolysis cell lacking a membrane. *Environ Sci Technol* **42**, 3401-3406 (2008).

179. Ren H*, et al.* Regulating the respiration of microbe: A bio-inspired high performance microbial supercapacitor with graphene based electrodes and its kinetic features. *Nano Energy* **15**, 697-708 (2015).

180. Stewart PS. Diffusion in biofilms. *J Bacteriol* **185**, 1485-1491 (2003).

181. Efficiency in Electricity Generation. (2003).

182. Seok M*, et al.* The Phoenix Processor: A 30pW platform for sensor applications. In: *VLSI Circuits, 2008 IEEE Symposium on*. IEEE (2008).

183. Conway B. *Electrochemical supercapacitors: scientific fundamentals and technological applications (POD)*. Kluwer Academic/Plenum: New York (1999).

184. El-Kady MF, Strong V, Dubin S, Kaner RB. Laser scribing of high-performance and flexible graphene-based electrochemical capacitors. *Science* **335**, 1326-1330 (2012).

185. Simon P, Gogotsi Y. Materials for electrochemical capacitors. *Nature materials* **7**, 845-854 (2008).

186. Munch E, Launey ME, Alsem DH, Saiz E, Tomsia AP, Ritchie RO. Tough, bio-inspired hybrid materials. *Science* **322**, 1516-1520 (2008).

187. Wegst UG, Bai H, Saiz E, Tomsia AP, Ritchie RO. Bioinspired structural materials. *Nature materials*, (2014).

188. Sanchez C, Arribart H, Guille MMG. Biomimetism and bioinspiration as tools for the design of innovative materials and systems. *Nature materials* **4**, 277-288 (2005).

189. Darder M, Aranda P, Ruiz-Hitzky E. Bionanocomposites: a new concept of ecological, bioinspired, and functional hybrid materials. *Advanced Materials* **19**, 1309-1319 (2007).

190. Whitesides GM, Crabtree GW. Don't forget long-term fundamental research in energy. *Science* **315**, 796-798 (2007).

191. Cusick RD, Kim Y, Logan BE. Energy capture from thermolytic solutions in microbial reverse-electrodialysis cells. *Science* **335**, 1474-1477 (2012).

192. Logan BE. Exoelectrogenic bacteria that power microbial fuel cells. *Nature Reviews Microbiology* **7**, 375-381 (2009).

193. Kim Y, Logan BE. Hydrogen production from inexhaustible supplies of fresh and salt water using microbial reverse-electrodialysis electrolysis cells. *Proceedings of the National Academy of Sciences* **108**, 16176-16181 (2011).

194. Lovley DR. Extracellular electron transfer: wires, capacitors, iron lungs, and more. *Geobiology* **6**, 225-231 (2008).

195. Malvankar NS, Mester T, Tuominen MT, Lovley DR. Supercapacitors Based on c-Type Cytochromes Using Conductive Nanostructured Networks of Living Bacteria. *ChemPhysChem* **13**, 463-468 (2012).

196. Uría N, Muñoz Berbel X, Sánchez O, Muñoz FX, Mas J. Transient storage of electrical charge in biofilms of Shewanella oneidensis MR-1 growing in a microbial fuel cell. *Environmental science & technology* **45**, 10250-10256 (2011).

197. Deeke A, Sleutels TH, Hamelers HV, Buisman CJ. Capacitive bioanodes enable renewable energy storage in microbial fuel cells. *Environmental science & technology* **46**, 3554-3560 (2012).

198. Esteve-Núñez A, Sosnik J, Visconti P, Lovley DR. Fluorescent properties of c-type cytochromes reveal their potential role as an extracytoplasmic electron sink in Geobacter sulfurreducens. *Environmental microbiology* **10**, 497-505 (2008).

199. Gardel EJ, Nielsen ME, Grisdela Jr PT, Girguis PR. Duty Cycling Influences Current Generation in Multi-Anode Environmental Microbial Fuel Cells. *Environmental science & technology* **46**, 5222-5229 (2012).

200. Schrott GD, Bonanni PS, Robuschi L, Esteve-Nuñez A, Busalmen JP. Electrochemical insight into the mechanism of electron transport in biofilms of Geobacter sulfurreducens. *Electrochimica Acta* **56**, 10791-10795 (2011).

201. Bonanni PS, Schrott GD, Robuschi L, Busalmen JP. Charge accumulation and electron transfer kinetics in Geobacter sulfurreducens biofilms. *Energy & Environmental Science* **5**, 6188-6195 (2012).

202. Ren H, Tian H, Ren T-L, Chae J. A micro-scale microbial supercapacitor. In: *Micro Electro Mechanical Systems (MEMS), 2014 IEEE 27th International Conference on*. IEEE (2014).

203. Alvarez-Gallego Y*, et al.* Development of gas diffusion electrodes for cogeneration of chemicals and electricity. *Electrochimica Acta* **82**, 415-426 (2012).

204. Zhang X, Pant D, Zhang F, Liu J, He W, Logan BE. Long-Term Performance of Chemically and Physically Modified Activated Carbons in Air Cathodes of Microbial Fuel Cells. *ChemElectroChem* **1**, 1859-1866 (2014).

205. An J, Lee H-S. Implication of endogenous decay current and quantification of soluble microbial products (SMP) in microbial electrolysis cells. *RSC Advances* **3**, 14021-14028 (2013).

206. Sevda S, Dominguez-Benetton X, Vanbroekhoven K, Sreekrishnan T, Pant D. Characterization and comparison of the performance of two different separator types in air–cathode microbial fuel cell treating synthetic wastewater. *Chemical Engineering Journal* **228**, 1-11 (2013).

207. Fricke K, Harnisch F, Schröder U. On the use of cyclic voltammetry for the study of anodic electron transfer in microbial fuel cells. *Energy & Environmental Science* **1**, 144-147 (2008).

208. Wang G, Zhang L, Zhang J. A review of electrode materials for electrochemical supercapacitors. *Chemical Society Reviews* **41**, 797-828 (2012).

209. Yan J*, et al.* Aniline Tetramer-Graphene Oxide Composites for High Performance Supercapacitors. *Advanced Energy Materials* **4**, (2014).

210. Rosche B, Li XZ, Hauer B, Schmid A, Buehler K. Microbial biofilms: a concept for industrial catalysis? *Trends in biotechnology* **27**, 636-643 (2009).

211. Wu ZS, Parvez K, Feng X, Müllen K. Graphene-based in-plane micro-supercapacitors with high power and energy densities. *Nature communications* **4**, (2013).

212. Jayashree RS, Mitchell M, Natarajan D, Markoski LJ, Kenis PJ. Microfluidic hydrogen fuel cell with a liquid electrolyte. *Langmuir* **23**, 6871-6874 (2007).

213. Roundy S*, et al.* Improving power output for vibration-based energy scavengers. *Pervasive Computing, IEEE* **4**, 28-36 (2005).

214. Lee H-S, Torres CI, Rittmann BE. Effects of substrate diffusion and anode potential on kinetic parameters for anode-respiring bacteria. *Environmental science & technology* **43**, 7571-7577 (2009).

APPENDIX A

COPYRIGHT

This dissertation includes some of my own published work. The detailed copyright permission is showing as below.

Chapter 1 is reproduced with permission from Ren H, Lee H-S, Chae J. Miniaturizing microbial fuel cells for potential portable power sources: promises and challenges. Microfluidics and Nanofluidics 13, 353-381 (2012). The chapter is written based on the paper.

Chapter 2 is reproduced with permission from Ren H, Lee H-S, Chae J. Miniaturizing microbial fuel cells for potential portable power sources: promises and challenges. Microfluidics and Nanofluidics 13, 353-381 (2012). The chapter is written based on the paper.

Chapter 3 is reproduced with permission from Ren H, Torres CI, Parameswaran P, Rittmann BE, Chae J. Improved Current and Power Density with a Micro-scale Microbial Fuel Cell Due to a Small Characteristic Length. Biosensors and Bioelectronics, 61, 587-592 (2014). The chapter is written based on the paper.

Chapter 4 is reproduced with permission from Ren H, et al. A high power density miniaturized microbial fuel cell having carbon nanotube anodes. Journal of Power Sources 273, 823-830 (2015). It is written based on the paper.

Chapter 5 is reproduced with permission from Ren H, Tian H, Gardner CL, Ren T-L, Chae J. A miniaturized microbial fuel cell with three-dimensional graphene macroporous scaffold anode demonstrating a record power density of over 10000 W m^{-3}. Nanoscale 8, 3539-3547 (2016). The chapter is written based on the paper.

Chapter 6 is reproduced with permission from Ren H, et al. Enhanced Current and Power Density of Micro-Scale Microbial Fuel Cells (MFCs) with Ultramicroelectrode (UME) Anodes. Accepted by Journal of Micromechanics and Microengineering. The chapter is written based on the paper.

Chapter 7 is reproduced with permission from Ren H, et al. Regulating the respiration of microbe: A bio-inspired high performance microbial supercapacitor with graphene based electrodes and its kinetic features. Nano Energy 15, 697-708 (2015). The chapter is written based on the paper.

APPENDIX B

FABRICATION PROCESS OF MEMS MFC

The fabrication of MEMS MFCs anodes starts with inlet/outlet formation. First, six through holes were drilled on a glass slide (46 mm × 26 mm × 1 mm, VWR), one as inlet, one as outlet and the rest four as screw holes. Then the glass slides were cleaned by piranha solution (concentrated H_2SO_4 and 30% H_2O_2, 3:1 volume ratio). Subsequently a layer of Cr/Au was deposited using a magnetron sputter (0.7 Pa, 150 mA for Cr and 45 mA for Au). The CNT based anodes and graphene based anodes are fabricated by growing or transferring CNT and graphene onto the anode.

The fabrication of MFC cathodes also started with inlet/outlet formation. First, six through holes were drilled on a glass slide (46 mm × 26 mm × 1 mm, VWR), one as inlet, one as outlet and the rest four as screw holes. Then the glass slides were cleaned by piranha solution (concentrated H_2SO_4 and 30% H_2O_2, 3:1 volume ratio). Afterwards, a layer of Cr/Au (20/200 nm) was deposited using a magnetron sputter (0.7 Pa, 150 mA for Cr and 45 mA for Au).

Anodes, cathodes, proton exchange membrane (PEM, Nafion 117), silicone gaskets (250 µm thick, Fuel Store Inc.), nanoports (10-32 Coned assembly, IDEX Health & Science), bolts and nuts were assembled to build the MEMS MFCs, as shown in Figure B.1. First, nanoports were glued to the inlet and outlet of anode and cathode glass slides by instant epoxy glue (Loctite). Second, two rectangular silicone gaskets with dimensions of 46 mm × 26 mm × 0.25 mm were patterned with a square hole of 10mm × 10 mm at the center, in order to define the anode and cathode chamber volume. Third, a rectangular PEM with a dimension of 46 mm × 26 mm was cut. Finally, anode, cathode, conductive copper tape as interconnect, PEM and silicone gaskets were assembled, as illustrated in Figure B.1.

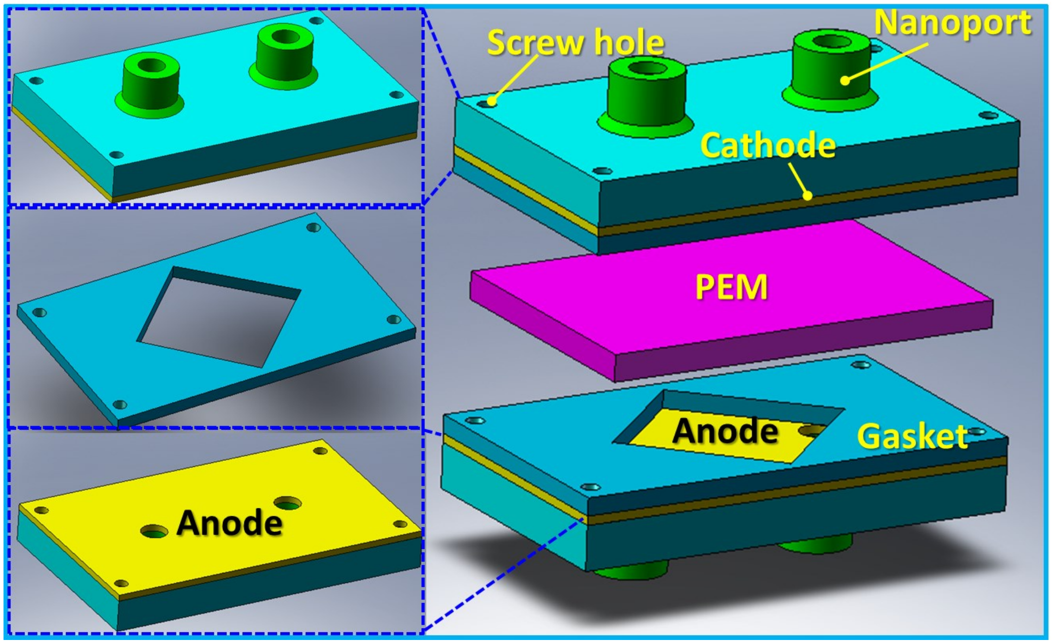

Figure B.1. Schematic of the fabrication process of the MEMS MFC

APPENDIX C

FABRICATION AND CHARACTERIZATION OF THE GRAPHENE BASED ANODE

A single-layer graphene with a size of 2×2 cm^2 was grown by chemical vapor deposition (CVD) on copper foil (25 µm, Alfa Inc.) at 1000 °C by flowing CH_4 and H. Afterwards, the single-layer graphene with copper foil was first spin-coat on polymethyl methacrylate (PMMA). Then the copper was removed by copper etchant, and it was afterwards cleaned by de-ion water by two times, 30 hour each time and afterwards it was dried for one day. After that, the graphene on PMMA was transferred onto the substrate (rectangular glass slide of 2.6×4.6 cm^2 with a layer of Cr/Au deposited on top through magnetron sputtering (20nm/200nm). Lastly the PMMA layer was dissolved in acetone for one hour, as shown in Figure C.1. An optical image of the single layer graphene on gold is shown in Figure C.2.

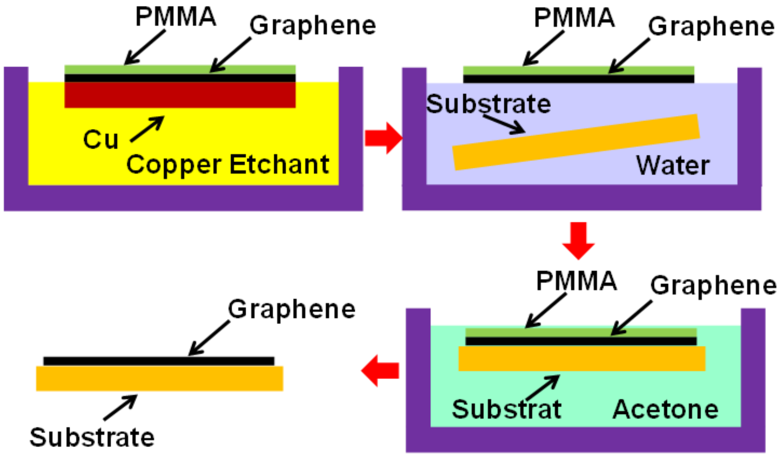

Figure C.1. Single layer graphene transfer on a glass slide.

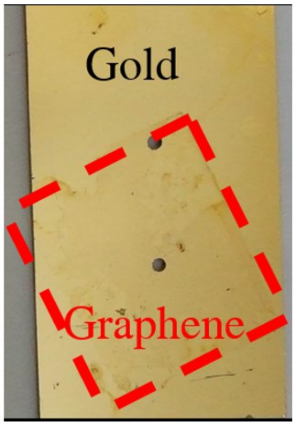

Figure C.2. Optical image of the graphene on gold current collector.

3D graphene scaffold was prepared by following fabrication procedures which has been described previously. Briefly, nickel foams (Alantum Advanced Technology Materials (Shenyang), ~320 g m^{-2} in areal density and ~1 mm in thickness) were used as 3D scaffold templates. Graphene was grown by CVD at 1000 °C. Afterwards, a thin PMMA layer was used as a support to reinforce the graphene scaffold structure for subsequent Nickel foam removal. The Ni foams covered with graphene were drop-coated with a PMMA solution, and then baked at 180 °C for 30 min. Then the samples were put into HCl (3 M) solution at 80°C for 3 h to completely dissolve the nickel. Finally free-standing graphene scaffold was obtained by dissolving the PMMA with hot acetone at 55°C. Optical and scanning electron microscopy (SEM) images of the 3D graphene scaffold is shown in Figure 1(d) and (e), respectively.

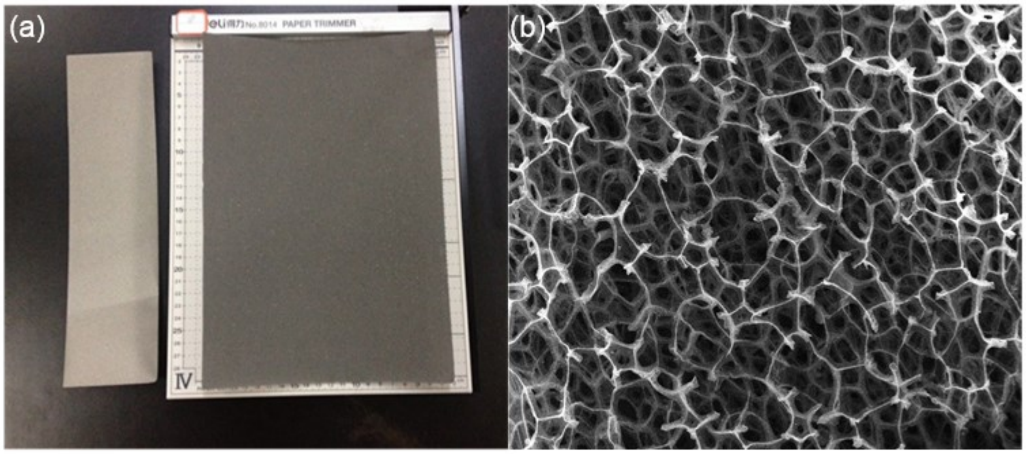

Figure C.3. Optical and SEM images of the 3D graphene scaffold.

Raman result of the single layer graphene in Figure C.4(a) showed graphene G and 2D peaks, indicating the single-layer graphene. The D peak presents finite defects in graphene film. In order to confirm the whole film quality of graphene, Raman mapping was performed, as shown in Figure C.4(b) and (c). Light field represents strong Raman signal with graphene film while dark field corresponds to weak signal without graphene. The results indicate good uniformity of single layer graphene film on the gold anode with some minor crack. Figure C.4(d) shows a transfer length method (TLM) to extract the sheet resistance of single-layer graphene, presenting ~ 4 kΩ/□. When the graphene layer was on the anode, obviously the sheet resistance decreases significantly, which is ~ 4.13 Ω/□.

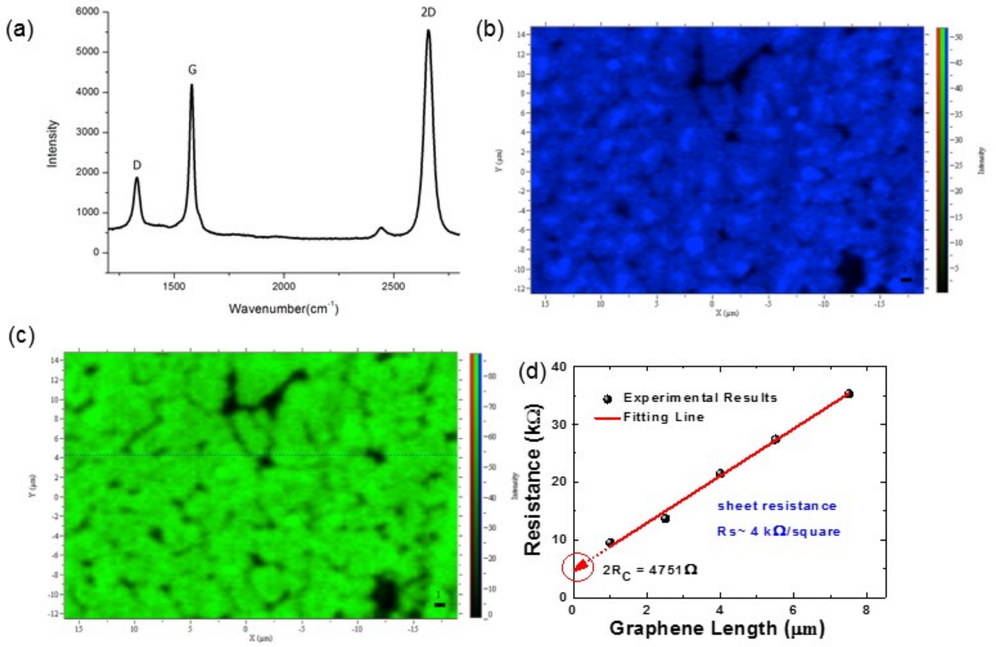

Figure C.4 Characterization of the graphene anodes: (a) Raman spectrum of the single layer graphene: typically graphene G and 2D peak are observed, indicating the single-layer graphene. The D peak presents finite defects in graphene film; (b) Raman G-band Mapping and (c) Raman 2D-band Mapping, these two figures indicate good uniformity of graphene film with minor cracks; (d) sheet resistance of single layer graphene.

APPENDIX D

NON-LINEAR FITTING THE DISCHARGING CURVE OF MICROBIAL SUPERCAPACITOR

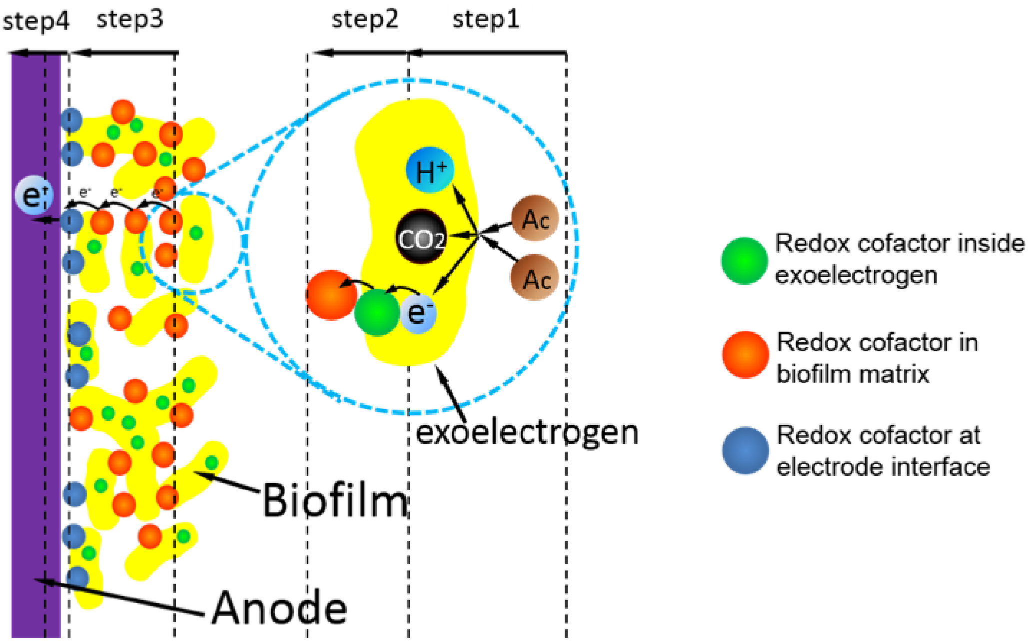

Figure D.1 A schematic of the 4 step for biofilm catalytic process: (1) irreversible acetate turnover by exoelectrogens; (2) electron transfer from inside exoelectrogens to extracellular redox cofactors (ERC) in biofilm; (3) electron transfer from ERC in biofilm to ERC at the anode interface; (4) oxidization of the ERC at the anode.

Biofilm catalytic process can be illustrated, including a series of 4 steps (Figure D.1): (1) irreversible acetate turnover by exoelectrogens; (2) electron transfer from inside exoelectrogens to extracellular redox cofactor (ERC) in biofilm; (3) electron transfer from ERC in biofilm to ERC at the anode interface; (4) oxidization of the interface ERC at the anode:

$$\frac{1}{8}CH_3COOH + Mic_{ox} \xrightarrow{k_{ac}} Mic_{red} + \frac{1}{4}CO_2 + H^+ \tag{D.1}$$

$$Mic_{red} + Erc_{ox} \xrightarrow{k_{mic}} Mic_{ox} + Erc_{red} \tag{D.2}$$

$$Erc_{red} + Erc_{ox,i} \xrightarrow{k_{erc}} Erc_{ox} + Erc_{red,i} \tag{D.3}$$

$$Erc_{red,i} \xrightarrow{k_{\text{int}}} Erc_{\text{ox},i} + e^{-} \tag{D.4}$$

where Mic_{ox}, Mic_{red}, Erc_{ox}, Erc_{red}, $Erc_{ox,i}$, $Erc_{red,i}$ denote the oxidized and reduced redox cofactor inside exoelectrogen, extracellular redox cofactors, and interface redox cofactors, respectively.

According to equation D.1-D.4, change of $Erc_{red,i}$ Erc_{red}, Mic_{red}, versus time is determined by the generation of $Erc_{red,i}$ Erc_{red}, Mic_{red}, minus the consumption of $Erc_{red,i}$ Erc_{red}, Mic_{red}, in equation, thus we can write:

$$\frac{dErc_{red,i}}{dt} = k_{erc} \cdot Erc_{red} \cdot (Erc_{total,i} - Erc_{red,i}) - k_{\text{int}} \cdot Erc_{red,i} \tag{D.5}$$

$$\frac{dErc_{red}}{dt} = k_{mic} \cdot Mic_{red} \cdot (Erc_{total} - Erc_{red}) - k_{erc} \cdot Erc_{red} \cdot (Erc_{total,i} - Erc_{red,i}) \tag{D.6}$$

$$\frac{dMic_{red}}{dt} = k_{ac} \cdot (\text{Mic}_{total} - Mic_{red}) - k_{mic} \cdot Mic_{red} \cdot (Erc_{total} - Erc_{red}) \tag{D.7}$$

For equation D.5, since the interface redox cofactors is in direct contact with anode, during the discharging process when working with sufficiently oxidative potential (anode polarization), step 4 is much faster than any other electron transfer process in EET. Thus, the step 4 will dominate the production rate of the interface redox cofactors, thus, equation D.5 can be rewritten as

$$\frac{dErc_{red,i}}{dt} = -k_{\text{int}} \cdot Erc_{red,i} \tag{D.8}$$

Solving this partial differential equation results in the reduced interface redox cofactors as a function of time. The discharge current, then, can be described by interface redox cofactors from equation D.4 (current generation is proportional to the change rate of reduced interface redox cofactors):

$$\begin{aligned} Erc_{red,\mathrm{i}} &= Erc_{red0,i} \cdot \exp(-k_{\mathrm{int}} \cdot t) \\ I_{\mathrm{Erc},i} &= F \cdot k_{\mathrm{int}} \cdot Erc_{red0,i} \cdot \exp(-k_{\mathrm{int}} \cdot t) \end{aligned} \qquad \text{(D.9)}$$

where $Erc_{red0,i}$ is initial interface cytochrome haems before discharging and F is Faraday constant.

For equation D.6, electron transport from the cell interior to the extracellular redox cofactors (Step 2) implicates a series of membrane transport processes which are considered to be slower than the transfer in between extracellular redox cofactors including *cytochrome* c, thus, we can rewrite equation D.7 as:

$$\frac{dErc_{red}}{dt} = -k_{erc} \cdot Erc_{red} \cdot (Erc_{total,i} - Erc_{red,i}) \qquad \text{(D.10)}$$

Likewise one can solve the partial differential equation to deduce the reduced extracellular redox cofactors as a function of time, and then obtain discharging current by ERC (current generation is proportional to the change rate of reduced ERC):

$$\begin{aligned} Erc_{red} &= Erc_{red0} \cdot \exp(-k_{erc} \cdot Erc_{\mathrm{total},i} \cdot t) \\ I_{Erc} &= F \cdot k_{erc} \cdot Erc_{\mathrm{total},i} \cdot Erc_{red0} \cdot \exp(-k_{erc} \cdot Erc_{\mathrm{total},i} \cdot t) \end{aligned} \qquad \text{(D.11)}$$

Note in order to calculate current in equation D.11, we write equation D.4 as

$$Erc_{red} \xrightarrow{k_{erc} \cdot Erc_{total,i}} Erc_{ox} + e^-$$

For equation D.7, we can assume Erc_{red}=0, we can write

$$\mathrm{Mic}_{red} = Mic_{red0} \cdot \exp[-(\mathrm{k}_{mic} \cdot Erc_{total} + \mathrm{k}_{ac})\,\mathrm{t}] + \frac{k_{ac} Mic_{total}}{k_{mic} Erc_{total} + k_{ac}} \cdot [1 - \exp[-(\mathrm{k}_{mic} \cdot Erc_{total} + \mathrm{k}_{ac})\,\mathrm{t}]] \tag{D.12}$$

Equation D.12 can be seen as a reversible reaction as follows, and thus similar with equation D.7 and D.11, we can get the current produced by this process

$$Mic_{red} \underset{k_{ac}}{\overset{k_{mic} \cdot Erc_{total}}{\rightleftharpoons}} Mic_{ox}$$

$$\mathrm{I}_{cells} = F \cdot k_{erc} \cdot Erc_{total} \cdot Mic_{red} \tag{D.13}$$

As a result, the total current is calculated as

$$\begin{aligned} I_{total} &= I_{Erc,i} + I_{Erc} + I_{cells} \\ &= F \cdot k_{\mathrm{int}} \cdot Erc_{red0,i} \cdot \exp(-k_{\mathrm{int}} \cdot t) \\ &+ F \cdot k_{erc} \cdot Omc_{\mathrm{total},i} \cdot Erc_{red0} \cdot \exp(-k_{erc} \cdot Erc_{\mathrm{total},i} \cdot t) \\ &+ F \cdot k_{erc} \cdot Erc_{total} \cdot Mic_{red0} \cdot \exp[-(\mathrm{k}_{mic} \cdot Erc_{total} + \mathrm{k}_{ac})\,\mathrm{t}] + \frac{k_{ac} \cdot Mic_{total}}{k_{mic} \cdot Erc_{total} + k_{ac}} \cdot [1 - \exp[-(\mathrm{k}_{mic} \cdot Erc_{total} + \mathrm{k}_{ac})\,\mathrm{t}]] \end{aligned} \tag{D.14}$$

As a result, we are able to fit the curve based on non-linear fitting approach:

$$\mathrm{I}_{total} = A\exp(-k_1 t) + B\exp(-k_2 t) + C\exp(-k_3 t) + D(1 - \exp(-k_3 t)) \tag{D.15}$$

where

$$\begin{aligned} \mathrm{A} &= F \cdot k_{\mathrm{int}} \cdot Erc_{red0,i} \\ B &= F \cdot k_{erc} \cdot Erc_{\mathrm{total},i} \cdot Erc_{red0} \\ C &= F \cdot k_{erc} \cdot Erc_{tot} \cdot Mic_{red0} \\ D &= \frac{F \cdot k_{ac} \cdot Mic_{total}}{k_{mic} Erc_{total} + k_{ac}} \\ k_1 &= k_{\mathrm{int}} \\ k_2 &= k_{omc} \cdot Erc_{\mathrm{total},i} \\ k_3 &= \mathrm{k}_{mic} \cdot Erc_{total} + \mathrm{k}_{ac} \end{aligned} \tag{D.16}$$

Figure 7.4(a)(b) shows the non-linear fittings of two discharge curves: one for initial biofilm and the other for fully-grown biofilm. One can find non-linear fitting constants (A, B, C, D, k_1, k_2, and k_3) and deduce kinetic parameters (Figure 7.4(c)(d)).

According to equation D.16, we are able to calculate the interface cytochrome, matrix cytochrome and redox cofactors inside exoelectrogen, $Erc_{redi,0}$, $Erc_{red,0}$, Mic_{total} by equation:

$$
\begin{aligned}
Erc_{red0,i} &= \frac{A}{k_1 \cdot F} \\
Erc_{red0} &= \frac{B}{k_2 \cdot F} \\
Mic_{total} &= \frac{D}{k_{ac} \cdot F}(k_{mic} Erc_{total} + k_{ac})
\end{aligned}
\tag{D.17}
$$

The discharging profile in initial and fully grown biofilms were fitted by non-linear fitting function in software Origin (Origin Inc.) The fitted curve and the residual error are shown in Figure D.2. The fitted curve matches well with the discharging curve, and the residual error is small. As a result, equation D.15 is suitable for fitting the discharging curve.

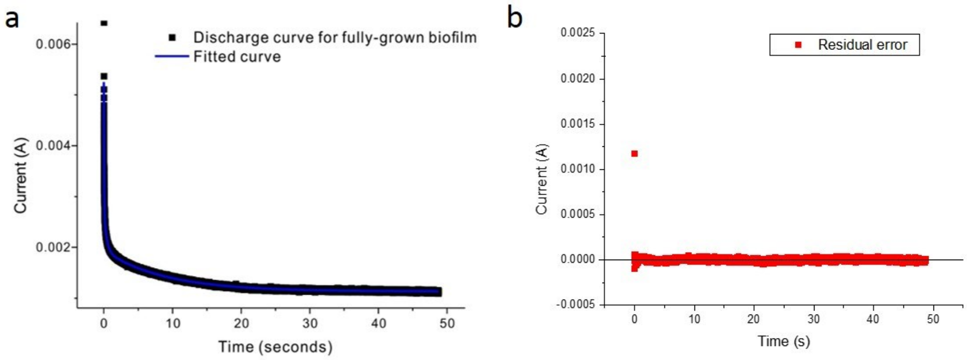

Figure D.2 Non-linear fitting of the charging curve in Origin for the fully-grown biofilm. (a) Discharging curve and fitted curve; (b) Residual error for the non-linear fitting.

The kinetics parameters are determined consequently by equation D.16 and equation D. 17, and the calculated parameters are shown in Table D.1.

Table D.1 Fitting parameters and the kinetics parameters derived by the non-linear fitting approach. (a) Fitting parameters by non-linear fitting in Origin; (b) kinetics parameters calculated by equation D.16 and equation D. 17.

(a)

	A (C)	B (C)	C (C)	D (C)	k_1 (s^{-1})	k_2 (s^{-1})	k_3 (s^{-1})
Initial biofilm	2.45×10^{-3} $\pm3\times10^{-5}$	1.57×10^{-3} $\pm3\times10^{-5}$	9.90×10^{-4} $\pm6\times10^{-6}$	1.16×10^{-4}	1.12×10^{2} ±1.3	3.27×10^{1} $\pm5\times10^{-1}$	5.45 $\pm2\times10^{-2}$
Fully-grown biofilm	2.48×10^{-2} $\pm6\times10^{-6}$	8.45×10^{-4} $\pm3\times10^{-6}$	1.94×10^{-3} $\pm5\times10^{-7}$	1.14×10^{-3}	3.65×10^{1} $\pm2\times10^{-1}$	2.76 $\pm1\times10^{-2}$	0.11 $\pm8\times10^{-7}$

(b)

	k_{int} (s^{-1})	k_{omc} ($s^{-1}Mole$)	k_{mic} ($s^{-1}Mole$)	k_{ac} (s^{-1})	$Erc_{total,i}$ (C)	Erc_{total} (C)	Mic_{total} (C)
Initial biofilm	1.12×10^{2} ±1.3	1.49×10^{6} $\pm2\times10^{4}$	1.00×10^{5} $\pm1\times10^{2}$	6.38×10^{-1} $\pm2\times10^{-3}$	2.19×10^{-5} $\pm1\times10^{-8}$	4.79×10^{-5} $\pm2\times10^{-7}$	2.06×10^{-4} $\pm3\times10^{-7}$
Fully-grown biofilm	3.65×10^{1} $\pm2\times10^{-1}$	4.07×10^{4} $\pm3\times10^{-2}$	1.53×10^{2} $\pm7\times10^{-2}$	6.64×10^{-2}	6.79×10^{-5} $\pm2\times10^{-7}$	3.05×10^{-4} $\pm2\times10^{-7}$	4.16×10^{-2}

APPENDIX E

CO-AUTHOR APPROVAL

I verify that the following co-authors have approved the usage of our publication materials in the dissertation:

Junseok Chae
Hyung-sool Lee
Cesar I. Torres
Bruce E. Rittmann
Prathap Parameswan
Soonjae Pyo
Jae-Ik Lee
Tae-Jin Park
Frederick Leung
Jongbaeg Kim
André Taylor
He Tian
Tian-Ling Ren
Cameron Gardner